Improved scintillator design for thermal neutron detection

by

Gunaratna Mudiyanselage Nadeera Hemamali

In Partial Fulfilment of the Requirements for the

Degree of Doctor of Philosophy

At the

Department of Electronic and Electrical Engineering

College of Engineering, Design and Physical Sciences

Brunel University London

December 2022

Thesis Supervisor:

Dr. David R. Smith

Second Thesis Supervisor:

Prof. Peter R. Hobson

Improved scintillator design for thermal neutron detection

G. M. Nadeera Hemamali

Abstract

Neutron detectors are used in various applications in nuclear security and nuclear safety. The most efficient neutron detection systems used in these applications are based on ^{3}He technology. The growing demand for ^{3}He already exceeds production in the next few years leading to an exponential increase of the price. The last decade has been driven by the quest for finding competitive alternative technologies to replace ^{3}He based detectors.

Thus, intense research and development continues to explore new phosphor materials as scintillators or the optimization of existing scintillators taking advantage of new technological methods for their preparation. The development of phosphors with rare earth elements such as gadolinium show a high potential for use as efficient and cost-effective inorganic scintillators for neutron detection.

The appealing feature of gadolinium, which has one of the highest neutrons capture cross sections, and the production of electrons instead of heavy charged particles, has pushed several research programs to study possible alternatives that use gadolinium. The work presented in this thesis is mainly focussed on the investigation of the development of scintillator layers based on natural gadolinium, mainly Gd_2O_3:Eu^{3+}, $GdBO_3$:Eu^{3+}, and $Li_6Gd(BO_3)_3$:Eu^{3+} for thermal neutron detection. Scintillators were prepared, using the ^{nat}Gd based phosphor prepared using simple urea precipitation method followed by K-bar technique. Hexagonal boron nitride (h-BN) based thin films have also been developed using the RF sputtering technique. Performance of those thin film scintillators were tested for thermal neutrons.

The key goals of the presented research work being the identification of improvements in the different parts of neutron detector design based on both experimental measurements and simulation activities.

Silicon Photomultipliers (SiPMs) represent a well-consolidated and cost-effective technology for a large range of applications requiring the detection of low light levels. In recent years, research efforts have been devoted to improving the basic performance of this kind of detector. In the presented research, a SiPM based readout system is used.

The front-end readout system for the SiPM has been developed and tested. The presented measurement results demonstrate that the implemented circuit has features that are attributable to photon detection. Here the research work mainly focused on reducing the power consumption of the required electronics and reducing the PCB size, to implement a lightweight portable handheld detector for ease of use in field activities.

Contents

Table of Figures   Page No.

Table of Tables   Page No.

Abbreviations

APD	Avalanche Photodiode
AP	After-Pulsing
CT	Crosstalk
DCR	Dark Count Rate
FLUKA	FLUktuierende KAskade
^{nat}Gd	Natural Gadolinium
GAGG:Ce	Cerium-doped gadolinium aluminium gallium garnet
G-APD	Geiger-APD
Gd_2O_3:Eu^{3+}	Europium doped Gadolinium oxide,
$GdBO_3$:Eu^{3+}	Europium doped gadolinium borate
LYSO:Ce	Cerium-doped lutetium-yttrium orthosilicate
$Li_6Gd(BO_3)_3$:Eu^{3+}	Europium doped lithium gadolinium borate
h-BN	Hexagonal Boron Nitride
MaPMT	Multi-anode Photomultiplier Tube
MCA	Multi-Channel Analyzer
PDE	Photon detection efficiency
p.e	photo-electrons
PMT	Photomultiplier Tube
RD	Relative Difference
SEM	Scanning electron microscope
SiPM	Silicon Photomultiplier
SPAD	Single-Photon Avalanche Diode
SRIM	Stopping Range of Ions in Matter – a collection of software packages that calculate many features of the transport of ions in matter
USB	Universal Serial Bus
YSO:Ce	Cerium doped yttrium orthosilicate

Key Symbols Used

Variable/Compound	Name	Value/Units
m_p	Proton mass	938.28 MeV/c^2
m_n	Neutron mass	939.57 MeV/c^2
τ_n	Mean lifetime	s
λ	Wavelength	m
$\hbar$	Plank's constant	6.626×10^{-34} m^2.kg/s
k	Wave-vector	
k_B	Boltzmann's constant	1.281×10^{-23} J/K
γ	Gamma radiation	
α	Alpha radiation	
σ	Capture cross section "barn"	10^{-28} m^2 (10^{-24} cm^2)
E	Energy	eV
$A(t)$	Activity of a radioisotope source	Bq ($= 2.7 \times 10^{-11}$ Ci)
ε	Efficiency	
Q	Total charge	C
I	Current	A

Declaration

I hereby declare that no part of this thesis has been previously submitted to this or any other university as part of the requirements for a higher degree. The work described herein was conducted solely by the undersigned except for those colleagues and others acknowledged in the text.

G.M. Nadeera Hemamali

30 December 2022

Acknowledgement

I would like to express my thanks to my principal supervisor: Dr. David Ryan Smith for his excellent guidance and encouragement in the research work. I appreciate his kindness and sensitivity and continuous support throughout my PhD journey. I would like to thank my supervisor: Prof. Peter Hobson, for his guidance through each stage of the process. I would like to acknowledge my research development advisor: Dr. George Fern, for inspiring my interest in developing materials for the research.

I would like to express my gratitude to Brunel Graduate School, the Postgraduate Research Office of the College of Engineering Design and Physical Sciences and all its staff for all the thoughtful guidance. I am also thankful to many other institutions, especially, NILE at RAL, Science and Technology Facility Council for supporting me by providing access to neutron sources for the research.

I would like to express my sincere gratitude to my mother for all the support and push forward. I thank my friends for all the unconditional encouragement and support during these academic years.

COVID-19 Impact Statement

A substantial amount of work developing hardware in the laboratory had to be abandoned when COVID-19 restrictions were implemented. It was not possible to fully transition the study to an online format due to the nature of the experimental activities that needed to be implemented in a practical laboratory, and during the related lockdown there was significantly less control over laboratory procedures. Unfortunately, the level of detail describing the development of the electronics hardware implementation for this project is therefore less than was originally intended for this aspect of the study.

Chapter 1

Introduction

Neutron detectors are used in various applications in nuclear security and nuclear safety, mainly to track illicit transportation of nuclear materials. Detection of illicit trafficking of such material relies on the detection of the radiation emitted, for example, in plutonium detection one of the characteristic signatures derives from neutron emission. For this reason, neutron detectors cover an important role, particularly in detection systems used in nuclear security. Most current neutron detection systems used for nuclear security are based on ^{3}He technology.

A typical ^{3}He detector consists of a gas-filled tube with a high voltage applied across the anode and cathode. A neutron passing through the tube interacts with a ^{3}He atom to produce tritium and a proton. The proton ionizes the surrounding gas atoms to create charges, which in turn ionize other gas atoms in an avalanche-like multiplication process, resulting charges which can be collected as measurable electrical pulses with the amplitudes proportional to the neutron energy. ^{3}He detector has high neutron detection efficiency, good gamma-ray discrimination, and non-toxicity. Hence ^{3}He based detectors are considered as standard.

As a result of the increasing demand for instrumentation for nuclear security, the need for ^{3}He has grown significantly. For neutron detectors, pure ^{3}He is required. ^{3}He is a rare non-radioactive isotope of helium, which is a by-product of tritium decay and no other mechanism of producing it is known at present. The growing demand for it already exceeds production in the next few years and encountered a huge problem in matching the supply and demand [1]. This has caused on one side an exponential increase in the value and on the other side a significant strategic problem of resources [2, 3]. To guarantee the availability of detection systems, it is necessary to develop alternative detection systems based on technologies different from ^{3}He, and new materials are needed to meet these challenges. Therefore, various investigations have been carried out with the goal to find alternative neutron detection technologies having similar characteristics to ^{3}He detectors [1, 4-12]. Suitable alternatives should fulfil the minimum requirements to detect the neutrons [4]. These requirements can be derived

from international standards given in [13, 14] and are that the instrument shall indicate the presence of neutron radiation. If the instrument provides a measurement of neutron count rate, no further testing is required.

The following types of commercially available detectors are used to detect neutron radiation, where possible to reduce consumption of ^{3}He.

- BF$_3$ gas-filled proportional detectors;
- Boron-lined proportional detectors;
- Semiconductor neutron detectors;
- Scintillation neutron detectors (liquid, plastic, thin film, fibers, etc.).

Comparison of above neutron detection technologies:

Boron fluoride is a toxic gas, potentially causing problems in shipping, installation, and long-term use, and the tubes have a significantly higher operating voltage and for this reason, have not been used in nuclear security applications [11]. Semiconductor crystals suffer from limitations in size that leads to a limit in their detection efficiency. Boron-lined gas-filled proportional counters are identical to ^{3}He counters and are probably the more practical short-term solution available on the market, but it has a relatively low detection efficiency; approximately seven times lower than a ^{3}He counter of the same size. Therefore, scintillation neutron detectors can be a longer-term alternative to ^{3}He technology [4].

Scintillation materials, loaded with a neutron absorber such as ^{6}Li, ^{10}B, and ^{157,155}Gd offer a method of realizing compact and rugged detectors for thermal and fast neutrons to enable the availability of detection systems [15-21].

At present all detectors of these types employ photomultiplier tubes (PMTs) or multi-anode photomultiplier tubes (MaPMTs) as photosensors. The application of silicon photomultipliers (SiPMs) in such detectors has been hindered by their higher dark count rate at room temperature and the deficient light collection due to its poor transparency made it difficult to combine a high trigger efficiency for the neutron signals with a reasonable suppression of the SiPM dark counts.

Silicon Photomultipliers (SiPMs) represent a well-consolidated and cost-effective technology for a large range of applications requiring the detection of low light levels.

In recent years, remarkable research efforts have been devoted to improving the basic performance of this kind of detectors, for instance increasing the Photon Detection Efficiency (PDE), and, on the other hand, to reduce the impact of their main drawbacks, such as dark count rate, after-pulsing and optical crosstalk [22, 23]. As a result, the possible application of SiPM detectors becomes wider and wider [24], covering fields where traditionally they have been considered a valid replacement for PMTs, such as in nuclear medicine (positron emission tomography), in high energy physics (calorimeters), astrophysics (Cherenkov telescopes), and in other single-photon or few-photon applications. For their characteristics, SiPMs are also very promising for the scintillator readout in neutron detectors.

This PhD project fits in this context of instrumentation development, focusing on the research and investigation of the development of thin film scintillation detectors loaded with neutron absorbers, ^{6}Li, ^{10}B and ^{nat}Gd, and readout by employing a SiPM, to investigate and fabricate possible inexpensive alternatives for replacing ^{3}He gas filled tubes for thermal neutron detection. The entire device, including the package, can be a few cm thick with good radiation hardness, allowing for the improvement of current lightweight detectors.

Thesis structure

Background literature relevant to the research, and theory has been reviewed in both Chapter 2 and Chapter 3. The simulation work carried out is presented in Chapter 4. In Chapter 5, we present a brief overview of scintillation detectors, and interactions of gamma-rays, which are used in this work. Preparation of scintillators, testing with neutrons, and comparison with experimental results are presented in Chapter 6. Implementation of PCB design, assembly, and testing are presented in Chapter 7. Results and discussion, conclusions, and recommendations for future work are presented in Chapter 8.

During the course of this research, the work has been published and presented at conferences. A full list of these is given below.

Publications

G.M. Nadeera Hemamali, D.R. Smith, P.R. Hobson, G. Fern, T. Ireland, "Gd_2O_3:Eu and $GdBO_3$:Eu scintillators for thermal neutron detection", Nuclear Instruments and Methods in Physics Research, A 1048 (2023). *(Chapter 6)*

G.M. Nadeera Hemamali, D.R. Smith, P.R. Hobson, "Determination of energy resolution for YSO:Ce detector modelled with FLUKA code", accepted for publication in IEEE Nuclear Science Symposium Conference Record (2023). *(Chapter 6)*

Poster Presentations

G.M. Nadeera Hemamali, D.R. Smith, P.R. Hobson, "Determination of energy resolution for YSO:Ce detector modelled with FLUKA code", IEEE Nuclear Science Symposium, Milan, Italy, November 2022. *(Chapter 4)*

G.M. Nadeera Hemamali, D.R. Smith, P.R. Hobson, T. Ireland, "Gadolinium Based Scintillators for Thermal Neutron Detection", International Conference on the Safety and Security of Radioactive Sources, IAEA, Vienna, Austria, June 2022. *(Chapter 6)*

G.M. Nadeera Hemamali, P. Hobson, D. Smith, G. Fern, T. Ireland, "Improved Scintillator Design for Thermal Neutron Detection", Brunel Graduate School Research Conference, Brunel University London, United Kingdom, 2021. *(Chapter 6)*

Chapter 2

Neutron interaction with matter

Neutrons together with protons constitute the nuclei of atoms. A neutron is a subatomic particle composed of three quarks (1 up quark and 2 down quarks), with no net electric charge and a mass slightly larger than that of a proton (m_p = 938.28 MeV/c^2, m_n = 939.57 MeV/c^2). Neutrons are decaying into a proton, electron, and an electron-antineutrino via radioactive decay known as β-decay with a mean lifetime of τ_n = 885.7±0.8 s due to instability of outside the nucleus [25, 26]. Neutrons are subject to all four fundamental interactions: gravitational, electromagnetic interactions, and strong and weak interactions. As neutrons are uncharged particles, the symbol is n or $^1n_0$, they are unaffected by the Coulomb potential of the electrons. The electron magnetic interaction of the neutrons is only due to the spin coupling (s = 1/2) with the magnetic moment.

The energy (E) of a neutron can be described in terms of its wavelength λ through the De Broglie relationship:

$$E = \frac{1}{2}\, mv^2 = \frac{2\,\pi^2\,\hbar^2}{m_n\,\lambda^2} \qquad (2.1)$$

Where $\hbar$ is Plank's constant, λ wavelength and m_n the mass of the neutron. The wave-vector k of the neutron has a magnitude:

$$k = \frac{2\,\pi}{\lambda} \qquad (2.2)$$

From equations 1.1 and 1.2, the energy E of the neutron can be written as:

$$E = \frac{\hbar^2 k^2}{2\,m_n} \qquad (2.3)$$

The energy can be defined by using temperature T as follows:

$$E = k_B\, T \qquad (2.4)$$

Where k_B = 1.281 × 10^{-23} J/K is the Boltzmann constant.

Although no specific boundaries are prescribed, due to the strong energy dependence of neutron interactions, neutrons are classified according to their energy. In Table 2.1, the neutron energy ranges are also roughly presented.

Table 2.1 Neutron Energy Ranges

Term	Energy
Cold	< 0.005 eV
Thermal	0.025 eV
Epithermal	0.02 eV
Slow	1-10 eV
Intermediate	300 eV - 1 MeV
Fast	1 - 20 MeV

Cold neutrons – energies below thermal energies, typically corresponding to meV and sub meV energies, from 0 to 0.025 eV. Neutrons in thermal equilibrium with very cold surroundings such as liquid deuterium. This spectrum is used for neutron scattering experiments.

Thermal neutrons – the most probable energy at 20°C for Maxwellian distribution is 0.025 eV (~2 km/s). This part of the neutron's energy spectrum constitutes the most important spectrum in thermal reactors.

Epithermal neutrons – energies between thermal (~0.025 eV) and a few hundred eV range. Neutrons of kinetic energy are greater than thermal. Some reactor designs operate with an epithermal neutron spectrum.

Slow neutrons – generally have energies between 100s of eV to 0.5 or 1 MeV. In this energy range, many of the nuclei that the neutron interacts with have nuclear structure within the combination of neutrons and protons that make up the nucleus, and that structure leads to an enhanced probability of interaction between the neutron and nucleus [27].

Fast neutrons – commonly energies between 0.5 and 10 - 20 MeV which are the energies of neutrons emitted by fission sources. This indicates the upper limit of the

research on neutron radiobiology and fundamental neutron interaction cross sections has been done [27].

When a neutron interacts with matter a variety of nuclear processes depending on its energy may occur.

Among these are:

i. Elastic scattering from nuclei, which is the main mechanism of energy loss for neutrons in the MeV region.
ii. Inelastic scattering. In this reaction, the nucleus is left in an excited state which may later decay by γ-ray or some other form of radioactive emission. The neutron must have sufficient energy, generally on the order of 1 MeV or more to excite the nucleus. Below this energy limit, elastic scattering may occur [27].
iii. Radioactive neutron capture.
iv. Other nuclear reactions, in which the neutron is captured and charged particles are emitted.
v. Fission occurs presumably at thermal energies.

The total probability of neutron interaction with matter is given by the sum of the individual cross sections listed for the above processes:

$$\sigma_{total} = \sum_i \sigma_i = \sigma_{elastic} + \sigma_{inelastic} + \sigma_{capture} + \cdots \quad\quad (2.5)$$

To obtain the macroscopic cross section ($\sum$, is used here as a variable symbol), σ_{total} should multiply by the density of atoms. The mean free path length (*l*), known as the mean distance travelled by a particle without suffering any collision, is the inverse of macroscopic cross section $\sum$:

$$\sum = n.\sigma_{total} = \frac{N_A.\rho}{A}.\sigma_{total} = \frac{1}{l} \quad\quad (2.6)$$

Where ρ is the material mass density, A is the atomic number and N_A is Avogadro's number.

When a narrow beam of neutrons passes through the matter, the number of detected neutrons will fall off exponentially with absorber thickness, d. In this case, the

probability for a neutron that has wavelength λ will interact with a nucleus of the matter at depth in a thickness dx is given by:

$$I(x, \lambda)dx = \sum e^{-x\Sigma(\lambda)} . dx \tag{2.7}$$

The number of neutrons that pass through a layer with thickness d:

$$\frac{N(d)}{N_0} = \int_0^d I(x, d)dx = \int_0^d \sum e^{-x\Sigma} . dx = 1 - e^{-d\Sigma} \tag{2.8}$$

Where N_0 is the initial incoming neutron flux.

For noncollimated source, equation 2.8 is no longer an adequate description. Hence, a more complex neutron transport calculation is required to predict the number of transmitted neutrons and their distribution in energy.

2.1   Neutron cross section

In nuclear physics, the concept of a neutron cross section is used to express the probability of interaction between an incident neutron and a target nucleus, conventionally stated in terms of the cross section (σ) per nucleus for each type of interaction. The standard unit for measuring the cross section is "barn", which is equal to 10^{-28} m^2 (10^{-24} cm^2).

An isotope (or nuclide) can be classified according to its neutron cross section and its reaction to an incident neutron. Nuclides that absorb a neutron, either decay or keep the neutron in their nucleus, and will have a capture cross section for that reaction.

2.2   Neutron sources and activity

A neutron source is any device that emits neutrons, mostly based on either spontaneous fission or nuclear reaction, and varies according to the energy of the neutrons emitted by the source, the rate of neutrons produced by the source, and the size of the source [28].

Some of the possible mechanisms to produce neutrons will be described here.

2.2.1 Spontaneous fission

Spontaneous fission can occur in certain isotopes, releasing neutrons along with the fission and promptly decay by emitting β and γ radiation. Commonly used spontaneous fission source is radioactive isotope ^{252}Cf which has a half-life of 2.65 years. The dominant decay mechanism is the alpha decay (~97%) compared to spontaneous fission (~3%) resulting of yield, 0.116 n/s per Bq, combining both decay rate. The energy spectrum of neutrons is continuous up to about 10 MeV and displays a Maxwellian shape distribution described by the following expression:

$$\frac{dN}{dE} = \sqrt{E \, e^{-\frac{E}{A}}} \tag{2.9}$$

Where the constant A = 1.3 MeV for the ^{252}Cf [25].

2.2.2 Nuclear reactions

A more convenient method of generating neutrons is through the nuclear reactions (α, n) or (γ, n). Such sources are generally made by mixing a strong α or γ emitter such as radium, polonium, or americium, with a suitable target material. The most common target material is beryllium. It undergoes several reactions which lead to the production of free neutrons under bombardment by alpha-particles, such as:

$$\alpha + {}^{9}\text{Be} \longrightarrow {}^{13}\text{C}* \longrightarrow \begin{cases} 12C^{*} + n \\ 8Be + \alpha + n \\ 3\alpha + n \end{cases} \tag{2.10}$$
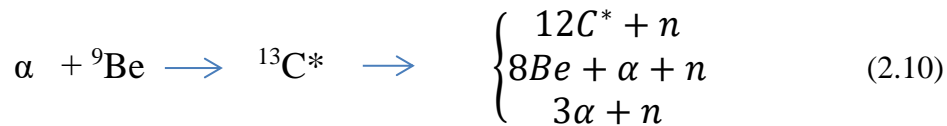
The excited nucleus ^{13}C*, depending on the excitation energy, decays through different modes. The dominant reaction is ^{12}C decay reaction. In general, the majority of α-particles simply stop in the target and approximately 1 out of 10^4 particles interact with a beryllium nucleus. The actinide elements are the most diffused alpha emitters, a stable alloy, such as ^{238}Pu/Be and ^{241}Am/Be can be made in the form MBe$_{13}$, where M represents the actinide metal [29].

In the case of photoreaction (γ, n), the emission of a free neutron arises if, by the absorption of a γ-ray photon, the target nucleus is in a sufficient excitation energy state. The advantage of these kind of sources is that if the gamma-rays are mono-energetic, then the neutron emitted also nearly mono-energetic.

2.2.3 Activity

The activity of a radioisotope source is defined as the number of disintegrations per second or the mean number of decay processes it undergoes per unit time. Note that the activity measures the source disintegration rate, which is not necessarily synonymous with the amount of radiation emitted in its decay. The relation between radiation output and activity depends on the specific nuclear decay scheme of the isotope. The activity can be defined as:

$$A(t) = \frac{dN(t)}{dt} = -\lambda\, N(t) \qquad (2.11)$$

Where, N is the number of nuclei and λ the decay constant.

The traditional unit of activity has been the Curie (Ci), defined as $3.7{\times}10^{10}$ disintegrations/second and is expressed in SI unit system as Becquerel. Thus 1 Bq = 2.7 $\times10^{-11}$ Ci.

2.3 Operating principle of neutron detector

All radiation detectors are based on the same fundamental principle, the transfer of part or all the radiation energy to the detector matter and conversion into an electrical signal [30]. The types of output electrical signals are dependent on the type of detector: gaseous, scintillator or solid-state, and their subsequent design.

Gaseous detectors are based on the direct collection of the ionization electrons and ions produced in the gas, while in scintillator detectors, the detection of ionizing radiation arises from the scintillation light produced in certain materials. When coupled to an

amplifying device such as a photomultiplier, it is possible to convert the light photons into an electrical pulse [31]. Solid-state detectors are based on semiconductor materials and basic operational principles are similar to gas ionization devices. Instead of gas the medium is a semiconductor, which produces charge carriers (electron-hole pairs) that drift and produce a signal. In a semiconductor, due to the small energy gap between their valence and conduction bands, the energy required to create an electron-hole pair is generally one order of magnitude smaller than that required for gas ionization [32].

An overview of several detectors used in applications in the thermal neutron energy region will be presented in the next section. The main references used are [28], [30], [32], and [33].

2.3.1   Neutron detectors

Thermal neutrons are not energetic enough to give rise to the charge produced by elastic scattering. Secondary radiation is, indeed, produced by capture reactions, either γ-rays of heavy charged particles such as protons, α, tritium or fission fragments. Different techniques have been used for neutron detection in different energy regions. Attention will be focused on the thermal neutron energy region, below 0.5 eV. When looking for nuclear reactions that could be useful in neutron detection, several factors must be considered:

- The cross section for the reaction.
- The discrimination gamma from neutron radiation.
- Q-value, the amount of energy absorbed or released during the nuclear reaction.
- The distance travelled by the reaction yields also concerns the detector design, in terms of the needful active volume to detect the released energy.

The most popular reactions for the conversion of slow neutrons are ^{3}He (n,p), ^{6}Li(n,α) and ^{10}B(n,α). All these reactions have large positive Q-values and large cross sections at thermal energies.

The ^{3}He (n,p) reaction can be written as:

$${}^{3}\text{He} + {}^{1}\text{n}_0 \longrightarrow {}^{3}\text{H (at 0.191 MeV)} + \text{p (at 0.573 MeV), 0.764 MeV}$$

The ${}^{6}\text{Li}$ (n,α) can be written as:

$${}^{6}\text{Li} + {}^{1}\text{n}_0 \longrightarrow {}^{3}\text{H (at 2.73 MeV)} + \alpha \text{ (at 2.05 MeV), 4.78 MeV}$$

The ${}^{10}\text{B}$ (n,α) can be written as:

${}^{10}\text{B} + {}^{1}\text{n}_0 \longrightarrow$ ${}^{7}\text{Li (at 1.015 MeV)} + \alpha$ (at 1.777 MeV), 2.79 MeV (6.3%) (to ground state)

${}^{7}\text{Li*}$ (at 0.84 MeV) + α (at 1.47 MeV), 2.31 MeV (93.7%) (1st excited state)

$\longrightarrow {}^{7}\text{Li} + \alpha + \gamma$ (0.478 MeV) (to ground state)
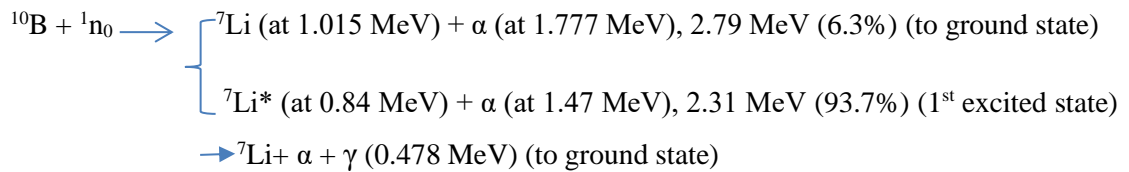
Q value of the reactions are very large compared with the incoming energy of the slow neutron, thus the energy distributed to the reaction products is essentially the Q value itself. This also means that the incoming linear momentum is very small, and therefore the reaction yields must show a total momentum of approximately zero. Namely, the products are emitted in exactly opposite directions and the energy will always be shared in the same manner between them.

Another important mechanism for low-energy neutrons, is radiative capture. The target nucleus absorbs the neutrons and goes in an excited state, the de-excitation into the ground state most probably occurs via emission of γ-ray.

A very interesting radiative capture process occurs when using naturally occurring gadolinium, ${}^{\text{nat}}\text{Gd}$, which has the largest thermal neutron absorption cross section of all the stable elements, with a total neutron absorption cross section of nearly 48,800 barns. The natural abundance of ${}^{155}\text{Gd}$ and ${}^{157}\text{Gd}$ isotopes in ${}^{\text{nat}}\text{Gd}$ are 14.8% and 15.8% respectively, contributing most significantly to the thermal neutron absorption cross section, approximately 99.99% of the elemental cross section [34]. The cross section for thermal neutron capture is about 2.5×10^5 barns for ${}^{157}\text{Gd}$, one of the largest nuclear cross sections in any material.

The Gd (n) can be written as:

$${}^{155}\text{Gd} + {}^{1}\text{n}_0 \rightarrow {}^{156}\text{Gd*} \rightarrow {}^{156}\text{Gd} + \gamma + \text{conversion electron} + \text{X-rays (39-199 keV)}$$

$${}^{157}\text{Gd} + {}^{1}\text{n}_0 \rightarrow {}^{158}\text{Gd*} \rightarrow {}^{158}\text{Gd} + \gamma + \text{conversion electrons} + \text{X-rays (29-182 keV)}$$

The reaction products of (n, γ) reactions on ^{155}Gd and ^{157}Gd are ^{156}Gd and ^{158}Gd respectively. The reaction Q-value energies are 8.536 and 7.937 MeV. (n, γ) reactions produce a large number of high energy gamma decays, typically above 1 MeV, which are not of primary interest in this work. The resulting de-excitations also produce transitions through numerous low-lying states, which are much more likely to be stopped within a relatively small scintillator crystal. The level scheme for the first three excited states in each of the nuclides of interest is shown in Fig. 2.1. The first excited states in ^{156}Gd and ^{158}Gd are at 88.97 keV and 79.51 keV respectively, which are populated by E2 transitions of 199.22 keV and 181.95 keV from the 4^+ 2nd excited states. In turn the 2nd excited states are themselves populated by E2 transitions of 296.4 keV and 277.6 keV from the 6^+ 3rd excited states. These transitions are the source of key neutron signatures for gadolinium containing scintillators. However, it should be noted that the 2^+ first excited states in both isotopes can also decay via internal conversion processes, and this mechanism produces an additional low energy neutron-related peak due to the escape of characteristic gadolinium K-shell X-rays.

Figure 2.1 The low-lying level structure for the rotational bands of ^{156}Gd and ^{158}Gd, adapted from [65]. The gamma ray transition energies are given alongside the competing internal conversion electron energy (in brackets)

The lower energy peak at ~43 keV is caused by internal conversion decays occurring within the Gd based scintillator from the first excited states.

A summary of the major decay routes for ^{158}Gd in the excited state through emission of high energy gamma-rays, low energy gamma rays, X-rays, internal conversion (IC) electrons, and Auger conversion electrons adapted from [19] are presented below:
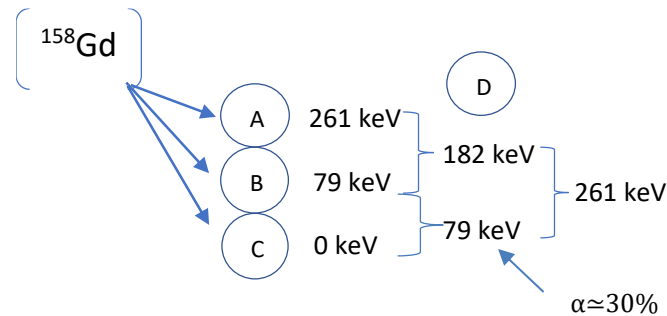
(A) $\gamma_1 + \gamma_2 = 7676.0$ keV (4.6%)

(B) $\gamma_1 + \gamma_2 = 7857.9$ keV (11.3%)

(C) $\gamma_1 + \gamma_2 = 7937.4$ keV (3.2%)

(D) Internal conversion electrons:

    182 keV   96.7% of IC energy

    79 keV

  X-rays:

    ~43 keV, K-shell   94.2% of X-ray energy

    ~7 keV, L-shell

  Coster-Kronig Auger electrons:

    ~1 keV, L-shell

The neutron absorption cross section in natural and isotopic Gd (^{157}Gd) takes quite high values over the range of cold and thermal neutrons, although it decreases very sharply for energies greater than 0.1 eV. The combination of small thickness and a large

absorption cross section makes gadolinium an appropriate converter for thermal neutrons.

The main problem compared with the other conversion reactions in which heavy charged particles are produced is the high γ ray background, and an effective pulse shape discrimination technique is needed.

2.4   Operation Principles of Detectors

In this section, a brief overview of different neutron detector types is presented.

2.4.1   Gaseous detectors

When a charged particle passes through a gas it interacts with the gas by ionizing and exciting the molecules along its path, resulting in a positive ion and a free electron, the so-called electron ion pair. The electron ion pair represents the basic element of the electrical signal employed in a gaseous detector.

Under the effect of an electric field E, with a velocity v, the mobility of the charged particles is given by:

$$\mu = \frac{v}{E}$$ (2.12)
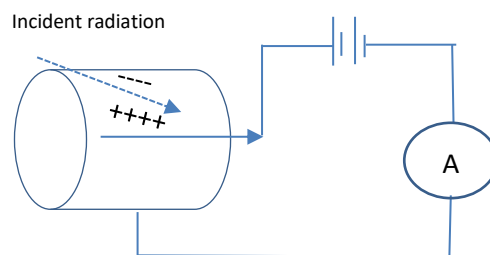
Figure 2.2 Sketch of a simple ionization detector

The radial electric field is given by:

$$E = \frac{1}{r} \cdot \frac{v_0}{\ln\left(\frac{b}{a}\right)}$$ (2.13)

Where r is the radial distance from the axis, b is the inside radius of the cylinder and a is the radius of the central wire.

When an incident radiation enters the gas volume, a certain number of election-ion pairs will be created along the track of the radiation. Regardless of the detailed processes involved, through a charged particle or secondary electrons or neutral, the practical quantity of interest is the total number of ion pairs.

The total number of ion pairs is given by:

$$n_{pair} = \frac{\Delta E}{w_i} \tag{2.14}$$

Where ΔE is the charged particle energy loss, and w_i is the effective average energy to produce one pair [35].

The mean number of electron-ion pairs is proportional to the energy deposited in the detector. Under the effect of the electric field, the electrons will be accelerated towards the anode and the ions toward the cathode, thus, it is necessary that the ion-pairs remain in a free state long enough to be read out. Positive ions and free electrons produced in the gas go through several types of collisions with the neutral gas molecules, diminishing the net charge generated by charge transfer collisions, electron attachment and recombination [28].

Figure 2.3 shows the charge produced by ionization as a function of the voltage applied to two electrodes, across the electric field is applied, where four operating regions are recognized: ionization, proportional, limited proportional, and Geiger region. The recombination and continuous discharge regions are not used as working regions for any device.

The ionization region is created when all ion pairs are collected after they overcome the recombination region, so any further increase in voltage does not show any effect. It is possible to recognize different detectors by the technology they use to operate in a given region. A detector working in the ionization region is called an ionization chamber as it collects the ionization produced directly by incident radiation. The signal is very small, and this type of device is generally used to measure gamma ray exposure.

When the voltage increases to a certain point the electric field will be strong enough to accelerate free electrons to ionize the gas molecules in the cylinder. These secondary ionizations are accelerated as well and can produce more ionization and so on. This effect is known as ionization avalanche or cascade. This avalanche occurs rapidly and entirely within a few radii of the anode wire making the number of ion-pairs in the avalanche directly proportional to the number of primary electrons produced. Hence, a detector operating in this domain is known as a proportional chamber. The proportional chamber is widely used for neutron detection or for low energy X-ray applications.
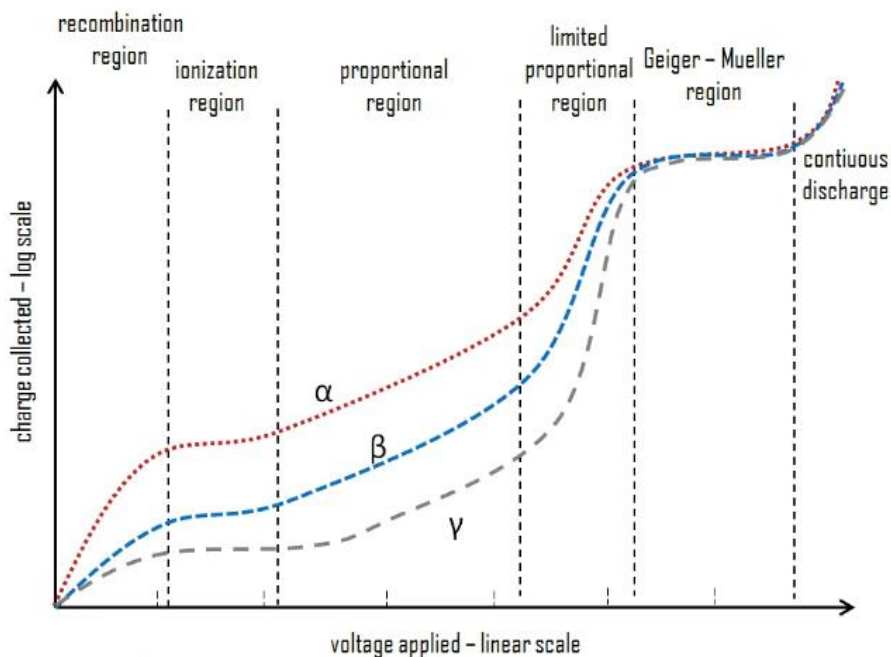
Figure 2.3 Gaseous ionization detector regions [36]

Further increase of voltage leads to the loss the proportionality, in fact, the amount of ionization produced through the avalanche multiplication process becomes large enough that the space charge effect deforms the electric field. This region is defined as the region of limited proportionality. Even higher voltage values generate discharge in the gas, leading to many multiplication processes and spreading out of the charge along the entire length of the electrode. The discharge can be stopped using a quenching gas, with a low ionization potential and a complex molecular structure, that can absorb these photons. Detectors working in this voltage region are called Geiger-Mueller counters.

2.4.2 Semiconductor detector

This section mainly draws information from the books [37-41] for the principles of operation discussion.

The basic operating principle of solid-state detectors is analogous to gas ionization detectors, although instead of a gas, the medium is a solid semiconductor material. The passage of ionizing radiation generates electron-hole pairs, which drift and create signals when an electric field is applied. The semiconductor gain advantages from a small energy gap between its valence and conduction bands, the average energy required to create an electron-hole pair being about 10 times smaller than that required for gas ionization. Furthermore, as their density and stopping power is larger compared to that of gas, semiconductor detectors are compact in size and can have very fast response times.

When an electric field is applied, the passage of electrons from the valence band drifts into the conduction band, generating holes in the valence band moving in the opposite direction to that of electrons in the conduction band. Thus, electrons move in the opposite direction to the electric field vector and holes move in the same direction as the electric field. Hence, the velocity of the charge carriers is proportional to the applied electric field through the mobility as follows:

$$v_e = \mu_e \,. E \qquad\qquad\qquad (2.15)$$
$$v_h = \mu_h \,. E \qquad\qquad\qquad (2.16)$$

Where μ_e and μ_h are the electron and hole mobility, respectively.

At higher electric field values, the drift velocity increases slowly with the field, until it reaches saturation velocity, which is independent from any further increase in the electric field strength. These velocities are on the order of 10^7 cm/s, thus the time required to collect the signals will be under 10 ns over a typical dimension of 0.1 cm. The mobility determines the current in a semiconductor, by using equation 2.15 and

2.16. The current density, J_c, for concentrations n of electron carriers and p of hole carriers, is given by:

$$J_c = q(n\mu_e + p\mu_h).E \qquad (2.17)$$

Where q is the electronic charge.

At a given temperature T, an equilibrium between generation and recombination of free electrons and holes is established. The production of concentrations of electrons and holes remains constant and is presented by:

$$np = n_{int}^2 \qquad (2.18)$$

Where n_{int} (cm^{-3}) is the intrinsic carrier concentration.

p-n junction:

When an n-type region in a crystal is put adjacent to the p-type region, a p-n junction is formed by diffusing acceptor impurities into an n-type crystal or vice versa. The formation of a p-n junction creates a special zone known as the depletion region between the two materials. The diffusion is the consequence of the motion of carriers from regions of high concentration to regions of low concentration, thus, the diffusing electrons fill up the hole in the p-region while the diffusing holes capture electrons on the n region. Hence, the p-side injected with extra electrons becomes negative, while n-region becomes positive. This creates an electric field across the junction.

The electric field is only due to the different concentrations of electrons and holes at the junction when no external voltage is applied. The diffusion process will move electrons generated in n-type material into p-type material and holes in opposite direction. This process is slowed down by the generated electric field due to the ionized dopants, which drives electrons back to the n-type side and holes into the p-type side, until a dynamical equilibrium is reached. Free charges can be produced in excess of the equilibrium by ionizing particles navigating the diode in the depletion region. The

charges produced by ionization in the depletion zone are separated and induce an electron-hole signal.

2.4.3 Neutron Detection with Silicon Detectors

Silicon detectors can be used to detect neutral particles through measurement of indirect ionization for photons, or secondary radiation for neutrons. Typically, the active area of the detector, the silicon-based component, is coupled to a neutron converter layer, where neutron interacts by giving rise to secondary heavy charged particles either via nuclear reactions or as energy recoils from an elastic scattering of neutrons on nuclei. These secondary charged particles produced in the converter must have a range bigger than the distance between the interaction point in the converter and the converter layer-detector interface, to reach the silicon layer where they deposit the energy. Then, charge carriers are produced in silicon, forming a signal.

Different converters have different mechanisms of producing secondary particles depending on the neutron energy, for example ^{10}B, ^{113}Cd, ^{155}Gd, ^{157}Gd, ^{6}Li are in general the most used converters for thermal neutrons. However, for higher energies of neutrons, such as fast neutrons, the neutron capture reactions have a much reduced cross section so another type of converter is required and another mechanism of charged particle generation needs to be exploited. Fast neutrons can be detected via energetic recoils produced from their elastic scattering on the nuclei of a converter. Converters with high hydrogen content need to be selected. In the case of thermal neutrons, the heavy charged particles generated in the converter material have their direction of emission kinematically constrained, the reaction products are emitted in opposite directions, so only one can cross the converter layer / detector interface into the underlying silicon.

2.5   Neutron Measurements

2.5.1   Pulse height Spectra

Pulse height spectra are measured using a multi-channel analyzer (MCA).

When operating radiation detector in pulse mode, each individual pulse amplitude carries important information regarding the number of photons detected by that particular radiation interaction in the detector. If a large number of such pulses are examined, their amplitudes will not be the same. Variations maybe due to either differences in radiation energy or fluctuations in the inherent response of the detector to monoenergetic radiation. Pulse height spectra are a fundamental property of the detector output and are routinely used to deduce information about the incident radiation or the operation of the detector itself.

2.5.2 Counting pulses

When radiation detectors are operated in pulse mode a common situation often arises in which the pulses from the detector are fed to a counting device with a discrimination level. Signal pulses must exceed a given level to be registered by the counting circuit. In setting up a nuclear counting measurement, it is often desirable to establish an operating point which will provide maximum stability over long periods of time. One such stable operating point can be achieved at a discrimination level and small changes in the discrimination level will have minimum impact on total number of pulses recorded.

2.5.3 Detector resolution

The energy resolution of the detector is conventionally defined as the full width at half maximum (FWHM) divided by the location of the peak centroid. Energy resolution R is thus a dimensionless quantity usually expressed as a percentage:

$$Resolution\ (R) = \frac{FWHM}{E_0} \qquad\qquad (2.19)$$

2.5.4 Detector efficiency

All radiation detectors in principle give rise to an output pulse for each quantum of radiation which interacts within its active volume. For primary charge radiation such as alpha or beta particles, interactions in the form of ionization or excitation will take place immediately upon entry of the particle into the active volume. Uncharged radiation such as gamma and neutrons must first undergo a significant interaction in the detector before detection is possible.

Because these radiations can travel large distances between interactions, detectors are often less than 100% efficient. It then becomes necessary to have a precise figure for the detector efficiency to relate the number of pulses counted to the number of neutrons or photons incident on the detector. It is convenient to subdivide counting efficiencies into two classes: absolute and intrinsic.

Absolute efficiencies are defined as:

$$\varepsilon_{abs} = \frac{no.\ of\ pulses\ recorded}{no.of\ radiation\ \ quanta\ emitted\ by\ source} \tag{2.20}$$

and are dependent not only on detector properties but also on the details of the counting geometry (primarily the distance from the source to detector).

The intrinsic efficiency is defined as:

$$\varepsilon_{int} = \frac{no.of\ pulses\ recorded}{no.of\ quanta\ incident\ on\ detector} \tag{2.21}$$

and no longer includes solid angle subtended by the detector as an implicit factor. The two efficiencies are simply related for isotopic sources by:

$$\varepsilon_{int} = \varepsilon_{abs}\ \frac{4\pi}{\Omega} \tag{2.22}$$

Where Ω is the solid angle of the detector seen from the actual source position [24].

The intrinsic efficiency of a detector usually depends primarily on the detector material, the radiation energy, the nature of the event, and the physical thickness of the detector in the direction of the incident radiation. A slight dependence on distance between the source and the detector does remain, however, because the average path length of the

radiation through the detector will change somewhat with this spacing. In practice, any measurement system imposes a requirement that pulses be larger than some finite threshold, set to discriminate against, very small pulses from electronic noise source. Thus, one can only approach, the theoretical total efficiency by setting this threshold level as low as possible. The peak efficiency, however, assumes that only those interactions that deposits the full energy of the incident radiation are counted.

It is often preferable from an experimental standpoint to use only peak efficiencies, because the number of full energy events is not sensitive to some perturbing effect such as scattering from surrounding objects, or spurious noise. Therefore, values for the peak efficiency can be compiled and universally applied to a wide variety of laboratory conditions, whereas total efficiency values may be influenced by variable conditions. To be complete, a detector efficiency should be specified according to both criteria. For example, the most common type of efficiency tabulated for gamma-ray detectors is the intrinsic peak efficiency.

The full energy peak efficiency (ε_p (E)) is defined as the ratio of the number of photon counts in the full energy peak corresponding to energy E ($N_p(E)$) to the energy emitted by the source, F(E):

$$\varepsilon_p(E) = \frac{N_P\,(E)}{F(E)} \qquad\qquad (2.23)$$

ε_p(E) depends on the source-detector geometry and on the energy:

$$\varepsilon_p(E) = \varepsilon_G \cdot \varepsilon_I(E) \qquad\qquad (2.24)$$

Where ε_I (E) is intrinsic efficiency and ε_G is the geometrical efficiency.

The ratio of the number of photons emitted towards the detector to the number of photons emitted by the source is:

$$\varepsilon_G = \frac{\Omega}{4\,\pi} \qquad\qquad (2.25)$$

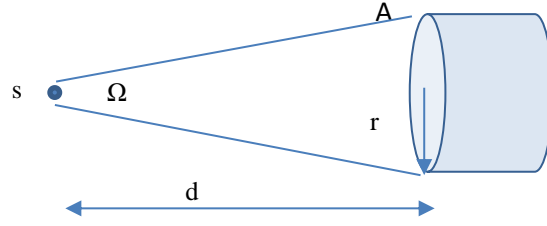For a point source the solid angle between source and detector Ω is given by:

Figure 2.4 Solid angle between source and detector

$$\Omega = 2\,\pi\,(1 - \frac{d}{\sqrt{d^2+r^2}}) \qquad\qquad (2.26)$$

Where d is the distance between source and detector, and r is the radius of the detector

For d >> r, the solid angle reduces to the ratio of the detector plane frontal area (A) visible at the source to the square of the distance [28]:

$$\Omega \simeq \frac{A}{d^2} = \frac{\pi r^2}{d^2} \qquad\qquad (2.27)$$

Intrinsic efficiency is defined as the ratio of the number of counts in the full energy peak to the number of impinging photons. The energy of the incident photons depends on transmission, absorption, and full energy deposition.

2.5.5 Dead time

In all detector systems there will be a minimum amount of time which must separate two events in order that they be recorded as two separate pulses. In some cases the limiting time may be set by the process in the detector itself, and other cases the limit may arise in the associated electronics. This minimum time separation is usually called *dead time* of the counting system. Because of the random nature of radioactive decay, there is always some probability that a true event will be lost because it occurs rapidly following a preceding event and this can become rather severe when high count rates are encountered. Any accurate counting measurements made under this condition must include correction for these loses [28].

Chapter 3

Silicon Photomultiplier

This chapter introduces Silicon Photomultipliers (SiPMs), their working principle, and the key parameters that represent SiPM performance, such as photon detection efficiency, dark count rate, crosstalk, after-pulsing, and non-linearity.

3.1 Working Principle

The base components of SiPMs are Single-Photon Avalanche Diodes (SPADs) that operate in Geiger mode [42,43].

The avalanche photodiode (APD) is a semiconductor detector. Most semiconductor detectors use a p-n junction as ionization medium. When ionizing radiation passes through the junction it interacts with the electrons of the semiconductor material and excites them from the valence to the conduction band, creating an electron-hole pair in the junction. These newly created charge carriers will be moved from the junction by the (intrinsic) bias voltage which results in a current flow. The total charge, Q, and bulk current of the signal, I, is given by:

$$Q = n.\,Q_{ion} = n.\,q.\frac{E_{ion}}{E_{bg}} = \frac{n.q}{E_{bg}} \int \left(\frac{dE}{dx}\right)_{ion} dx \qquad (3.1)$$

$$I = I_p + I_n = \left(\frac{1}{t_{c,p}} + \frac{1}{t_{c,n}}\right).Q \qquad (3.2)$$

Where n is a multiplication factor,

E_{ion} is the total energy deposited in the junction by the radiation,

E_{bg} is the band gap between valence and conduction bands, and

$t_{c,p}$ and $t_{c,n}$ are the charge collection time of holes and electrons respectively.

25

With no applied bias voltage most of these mobile charge carriers will recombine in the semiconductor before they reach the electrodes, since the initially created number of electron-hole pairs is small the output signal will be small as well. The total collected charge can be increased by applying a higher bias voltage. With the bias voltage in the ion chamber region the charge carriers are accelerated fast enough to reach the electrodes and create a signal (n = 1). By increasing the voltage further, the charge carriers have enough energy to ionize the atomic shells which results in an avalanche of additional secondary charge (n = 100 - 1000). APDs usually operate in this region since the multiplication of the primary induced charge is high enough to detect a signal without the need of further external components. Increasing the voltage even more will result in the secondary charges being energetic enough to again ionize the atom hulls which leads to a self-sustaining avalanche. This avalanche grants a large multiplication of the initial charge but makes the diode permanently conductive and also produce additional noise from the statistical fluctuations in the avalanche process.

To make it sensitive to radiation again an external quenching resistor is needed. When a current flows through this resistor the voltage drop will decrease the bias voltage and stop the avalanche. This region called Geiger region and an APD operating in this mode is called Geiger-APD (G-APD). Because of the large multiplication factor the G-APD is suited for low energy deposition or single photon detection which is why they are also referred to as Single-Photon Avalanche Diode (SPAD).

In a SPAD a number of secondary electron-hole pairs are formed and a resulting avalanche of charge carriers passes through the diode generating a self-sustaining sizable current. At this point, a single optical photon can be detected. To detect another photon, it is required to quench the avalanche using passive or active elements. During the avalanche and the quench time, a SPAD is not able to detect another photon. Thus, if more than one photon impinges on the SPAD simultaneously, the SPAD output does not change. To avoid this limitation, many SPADs are connected in parallel to common anode and cathode to form a matrix: such a device is called a Silicon Photomultiplier (SiPM) [44, 45].

3.2. Silicon Photomultiplier (SiPM)

A Silicon Photomultiplier (SiPM) is solid-state single photon sensitive detector formed of array of SPADs including quenching resistors as shown in Fig. 3.1. In this setting, a single SPAD is referred to as a pixel. If a pixel is hit by radiation the initial deposited charge is multiplied by the avalanche effect as described above and outputs the charge Q_{pix}:

$$Q_{pix} = C_{pix}(V_b - V_{bd}) = C_{pix} \cdot V_{ov} \qquad (3.3)$$

Where C_{pix} is the diode capacitance of a pixel, V_{ov} is the overvoltage of the diode, V_b is the applied reverse bias voltage, and V_{bd} is the diode's breakdown voltage.
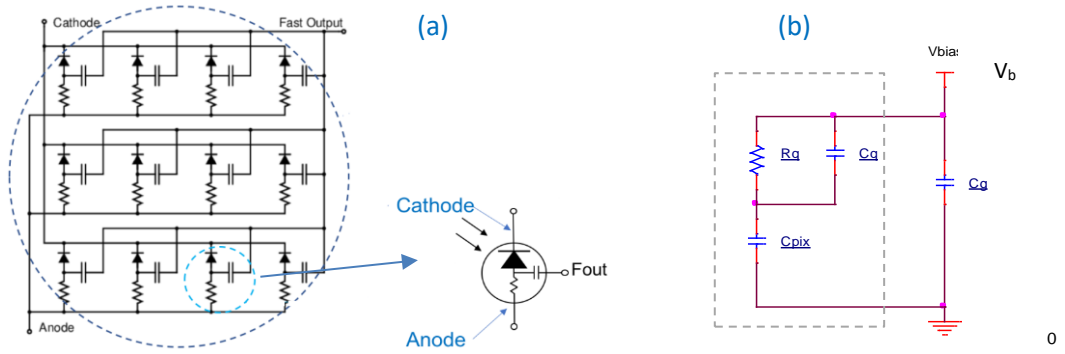
Figure 3.1 (a) Array of Microcells [46] (b) Electrical model, C_{pix}-pixel capacitance, R_q-quenching resistance, C_q-parasitic capacitance, C_g-grid capacitance

The signal output due to the charge Q_{pix} is also known as a photon equivalent (p.e.) pulse. The total signal given by an SiPM is the sum of all p.e. pulses emitted by individual pixels hit by radiation. The pulses consist of two-time components: a fast-rising edge caused by the Geiger discharge, and a long falling edge due to the slow pixel recovery time. The pixel recovery time constant τ_r is defined by the value of the quenching resistor R_q and the pixel capacitance C_{pix}:

$$\tau_r = R_q \cdot C_{pix}. \qquad (3.4)$$

After the recovery time Υ_r, the pixel regains the charge $Q(\Upsilon_r) = \frac{Q_{pix}}{e}$ due to quenching of the avalanche and is again sensitive to radiation.

Figure 3.2 Pulse shape of SPAD
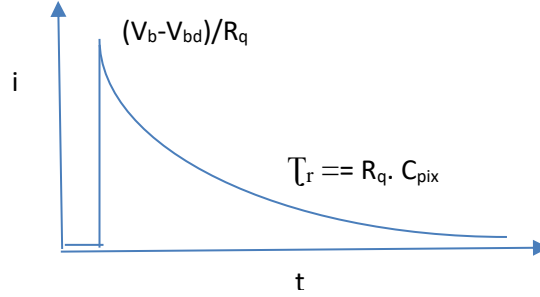
A histogram of the output charge of an SiPM is also referred to as a finger spectrum. An example of a finger spectrum is illustrated in Fig. 3.3. The distance of each peak is constant and given by the gain of the SiPM:

$$Gain\ (M) = \frac{Q_{pix}}{q} = \left(\frac{C_{pix}\ (V_b - V_{bd})}{q}\right) \qquad (3.5)$$

In SiPMs, there are two different types of noise, the primary noise and the correlated noise, which are related to different physical phenomena. The primary noise, also called Dark Count Rate (DCR) is due to the thermal generation of carriers in the depletion region. Instead, the correlated noise is due to a previous pulse, which can be photon or thermally generated. There are two main contributions to the correlated noise, After-Pulsing (AP) and Crosstalk (CT) [47, 48]. The AP occurs due to impurities in the bulk material. These impurities may absorb photons in a metastable state and emit them again after a short period of time, during the quenching of the avalanche discharge. Crosstalk is caused by photons escaped from one cell during an avalanche discharge that can be absorbed in adjacent cells leading to a second p.e. pulse from the second pixel. It is easily possible that a single photon can induce a 3 p.e. signal as depicted in Fig. 3.4.
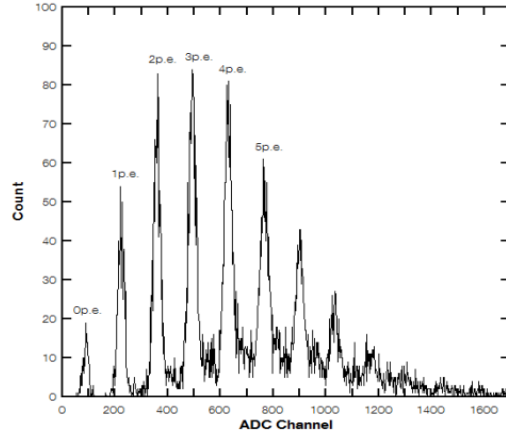
Figure 3.3 Photoelectron spectrum of the SiPM [21]

The output charge increases with the reverse bias voltage V_b, as well as the dark current I_d (and after-pulse probability):

$$I_d \ \alpha \ T^{\frac{3}{2}} \ e^{\frac{E_{bg}(V_b)}{2KT}} \qquad\qquad (3.6)$$

The breakdown voltage V_{bd} of the pixels increase with temperature since the probability of inelastic scattering of the charge carriers inside the bulk increases due to thermal excitation of atoms in the junction. Since V_{bd} increases, the overvoltage V_{ov} decreases with rising temperatures at a constant reverse bias voltage V_b. To obtain a constant signal spectrum, one must adjust V_b:

$$V_b(T) = \frac{\Delta V_b}{\Delta T} \ (T - T_0) + V_b(T_0) \qquad\qquad (3.7)$$

Where, $\frac{\Delta V_b}{\Delta T}$ is the temperature correction coefficient, T_0 a fixed offset temperature, and V_b (T_0) the bias voltage at the given offset temperature.
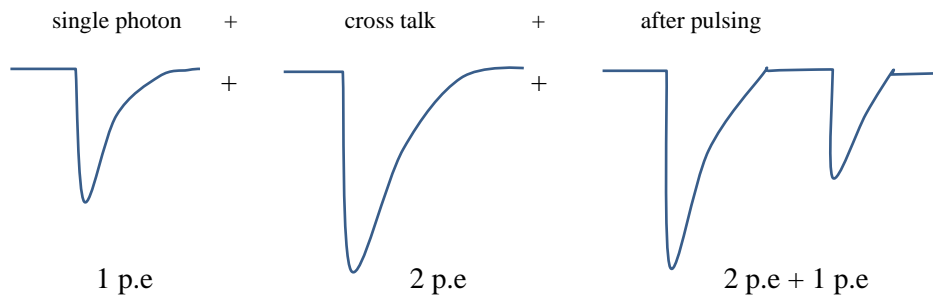

Figure 3.4 Effects of crosstalk and after-pulsing on the output signal of a SiPM

29

Dark Count Rate (DCR) results from counts generated in the absence of photons due to avalanches triggered by randomly generated carriers, and so follows the Poisson distribution. DCR has two different sources, thermal generation due to the Shockley-Read-Hall processes [49] and band-to-band tunnelling generation, due to the tunnelling of the electrons from the valence to the conduction band [47].

After-Pulsing (AP) is due to carriers which are trapped during a primary avalanche and then released with a time delay, thus triggering another avalanche. The traps are defects and impurities in the semiconductor lattice, which produce energy levels in the forbidden band gap [47]. The AP probability depends on three factors:

• **Trap capture probability:** depends on the number of traps and on the number of carriers flowing during an avalanche.

• **Trap lifetime:** depends on the trap level position, on the trap type, and on the temperature.

• **Triggering probability:** depends on the bias voltage and on the recovery condition of the microcells.

AP can be reduced by minimizing defects which may be introduced during the processing of the detector material, and by decreasing the gain [47]

Crosstalk (CT) is a phenomenon which occurs mainly between adjacent cells. During an avalanche discharge, $\sim 3 \times 10^{-5}$ photons are emitted for each carrier crossing the junction with energy higher than 1.14 eV [48]. These photons can trigger an avalanche in adjacent cells. CT depends on the distance between high-field region of the microcells, and thus can be reduced using trenches in silicon, which can be also filled with opaque material, between the SiPM microcells, and reducing the microcell gain. Usually, CT pulses occur at the same time as the primary pulse.

3.2.1 Dynamic range

The dynamic range of SiPMs is limited by the finite number of their cells. SiPMs provide a good linearity if the number of impinging photons is lower than the number of cells, $N_{photons} \ll N_{cells}$. When this condition is not met, the SiPM response is non-linear. This behaviour can be described by a Poisson distribution. The probability of

having n-interactions in a cell i, $P_i(n)$, can be expressed assuming that the photons are evenly distributed across all the microcells, as:

$$P_i(n) = \frac{e^{-\frac{N_{Photons} \cdot PDE}{N_{cells}}} \cdot \left(\frac{N_{Photons} \cdot PDE}{N_{cells}}\right)^n}{n!} \tag{3.8}$$

Where $N_{Photons}$ is the number of impinging photons, PDE is the SiPM photon detection efficiency, N_{cells} is the number of SiPM cells, and n is the number of interactions.

The number of SiPM fired cells, N_{fired}, is given by:

$$N_{fired} = N_{cells} \cdot (1 - P_i(0)) = N_{cells} \cdot \left(1 - e^{-\frac{N_{Photons} \cdot PDE}{N_{cells}}}\right) \tag{3.9}$$

Where $P_i(0)$ is the probability of having 0 interactions, calculated using Eq. 3.8.

Another linearity limiting factor is the recovery time of the cell, τ_{SiPM}. When a cell is fired, it is not able to detect another photon for a time, called dead time, which depends on τ_{SiPM}. However, if the distribution in time of photons, i.e. the photon rate, has a τ_{Light} > τ_{SiPM}, a single cell of a SiPM can be triggered more than once in the τ_{Light} interval. This re-trigger capability improves the linearity of SiPMs. Thus, a way to reduce the non-linearity is to increase the density of cells, cells/mm^2, in a SiPM reducing their size. The high cell density and the short recovery time are very important factors to improve the linearity of the SiPM in high-dynamic-range applications, such as the scintillation light readout in high-energy gamma-ray spectroscopy and in prompt gamma imaging for proton therapy. The reduction of the cell size has also a drawback, that is a decreasing of the PDE because of the lower fill factor, and consequently a worsening of the energy resolution. Thus, it is not sufficient to evaluate the linearity of the SiPM but it is necessary to evaluate how the cell density impacts on global performance of the SiPM.

3.2.2 Single photon time resolution

Another interesting feature of SiPMs is their excellent Single Photon Time Resolution (SPTR). The response is determined by avalanche discharge and is in the order of few hundreds of ps [50]. The major contribution at timing performance is due to the statistical fluctuations of the current growth due to the photo-conversion depth, a vertical build-up at the beginning of the avalanche, and a lateral propagation of the avalanche.

Chapter 4

Study 1

Simulation

4.1. Introduction

The response function of the scintillator can be found using both experimental studies and Monte Carlo simulations (FLUKA, MCNP simulation software). For this study, FLUKA Monte Carlo codes have been chosen to simulate the transport of incident neutrons and neutron-induced charged particles. The aim was to optimize detector response using FLUKA Monte Carlo Code. FLUKA Monte Carlo Code is a transport code widely used in radiation simulation studies mainly in high-energy physics. The FLUKA code is written in Fortran and used for calculations of particle transport and interactions with matter. FLUKA can simulate the interaction and propagation in matter of about 60 different particles from 1 keV to thousands of TeV, neutrinos, muons, hadrons, and all the corresponding antiparticles, neutrons down to thermal energy, and heavy ions, with high accuracy. The FLUKA code can also simulate the transport of polarized and optical photons [51].

The FLAIR package was used together with FLUKA for simulation activities. FLAIR is an advanced user-friendly interface for FLUKA to facilitate the editing of FLUKA input files, execution of the code, and visualization of the results.

In this work the purpose of the simulations are:

1) to optimize Gd based scintillator detector for 2.5 MeV neutrons emitting from Deuterium-Deuterium (D-D) source. The devices have an active thickness 100 µm and an active area of 1 cm².

2) to optimize h-BN detector for thermal neutrons emitting from AmBe source. The device has an active area of 1 cm^2.

3) to optimize single crystal scintillators for gamma energy range 59-662 keV. In the second step of the simulation, resolution of the detector was studied for different materials and thickness.

4) later in the thesis, these results compared with the experimental results.

4.2. Software

FLUKA is a Fortran-based Monte Carlo code used to calculate particle transport and interactions with matter and can be applied in many different fields such as nuclear physics, high-energy physics, and particle physics. The software was developed by CERN (European Organization for Nuclear Research) and INFN (Italian National Institute for Nuclear Physics) [52, 53]. FLUKA has a FLAIR interface for editing the input file, executing the code, and visualizing the output files. This study was done with FLUKA version 4.2.0 and FLAIR version 3.1-15 installed under the Community Enterprise Operating System (CentOS), a Linux-based operating system.

4.3 Simulation Method

FLUKA offers numerous different estimators that can be used to score various quantities of interest. The parameters for simulating detector response were activated using the DEFAULTS card, with the PRECISIO option. The PRECISIOn option is used for precision simulations. It includes low energy neutron transport down to thermal energies and fully analogue absorption for low-energy neutrons. FLUKA cards, BEAM and BEAMPOS used to introduce the energy type, position/direction and energy spectrum of radiation sources, respectively. MATERIAL card defines a single element and COMPOUND card was used to define (complex) materials in simulations. ASSIGNMA card is used to assign material to one or more regions.
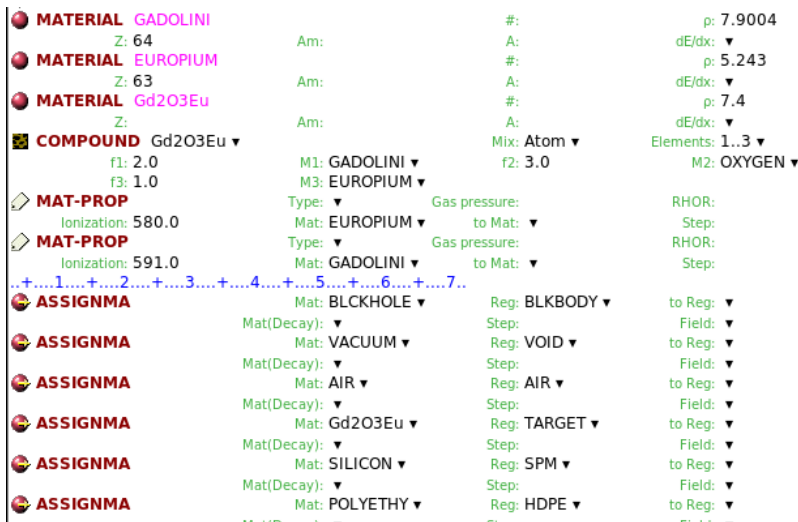
Figure 4.1 Example of card assigning in the input file

The USERBIN card is used to score the spatial distribution of energy deposited, or total fluence in a regular mesh (cartesian). The DETECT card is used for acquiring energy deposition spectrum. The DETECT card output gives a spectrum distributed over a fixed number of channels. In this study, 1024 channels were used. The light produced in scintillator material is emitted in all directions. Only a limited fraction of it reaches the surface where SiPM is mounted. Thus, the USRBDX card is used to calculate the light passes through the boundary.

The PHYSICS card is used for adding evaporation of heavy fragments when needed in the simulation. The EMFCUT card is used for setting threshold for transport of electrons, positrons, and photons with the TRANSPORT option and setting delta-ray production threshold with the PROD-CUT option. RADDECAY cards are used for simulation of decay of produced radioactive nuclides and allow for the modification of biasing and transport thresholds (defined by other cards) for the transport of decay radiation.

Figure 4.2 Example of cards assigning in input file

All these functions (cards) are used for finding the response function of scintillator detector. As well as visualization of neutron fluence, the corresponding energy deposition, the number of light photons produced, and the amount of light passing through the boundary were simulated for each scintillator type.

The scintillators and radiation sources used in this study are listed in Table 4.1.

Table 4.1 Scintillator sizes/types and radiation sources used for this study

Scintillator Type	Scintillator Size	Radiation
$Gd_2O_3:Eu^{3+}$	Thin film	Thermal neutrons
$GdBO_3:Eu^{3+}$	Thin film	
$Li_6Gd(BO_3)_3:Eu^{3+}$	Thin film	
h-BN	Thin films	
YSO:Ce	$5\times5\times5$ mm^3	Gamma radiation (59-662 keV)
LYSO:Ce	$5\times5\times1$ mm^3	
GAGG:Ce	$5\times5\times1$ mm^3	

Since the objective of the presented study was to generate the response function of a given scintillator as accurately as possible, one must locate the interaction site of each incident radiation particle and deduce their corresponding energy depositions.

4.4. Simulation for neutrons

This section presents the simulation of thermal neutron capture in gadolinium-based materials and hexagonal boron nitride.

The DETECT card was used for acquiring energy deposition spectra. The EMF (electromagnetic interactions) card was active and the cut-off energy for photons was set to 10^{-6} GeV. The light produced in the scintillator material was emitted in all directions. Only a limited fraction of this light reaches the surface where the SiPM detector is mounted, the USRBDX card being used to calculate the light passing through the boundary. To obtain a reasonable statistical error (<2%), 10^8 particles were run for each simulation over five cycles.

4.4.1 Gd$_2$O$_3$:Eu^{3+}

Europium doped gadolinium oxide (Gd$_2$O$_3$:Eu^{3+}) is an inorganic compound. For film detectors, the neutron absorbing film acts to absorb neutrons. The absorption of the neutron leaves the ^{158}Gd in an excited state that releases energy through emission of high-energy gamma rays, low-energy gamma rays, X-rays, and conversion electrons as:

$$n + {}^{157}Gd \rightarrow {}^{158}Gd^* \rightarrow {}^{158}Gd + \gamma + \text{conversion electrons} + \text{X-rays (29-182 keV)}$$
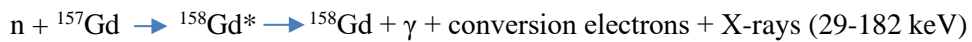
A similar result occurs with the neutron capture process of ^{155}Gd(n,γ) ^{156}Gd. However, a gadolinium-based semiconductor heterojunction, can produce pulses with characteristics of the K-shell Auger electron resonances following neutron capture [19]. So long as there is neutron capture, the resulting Auger electron spectrum is characteristic of the atomic electronic transitions that include a Gd 1s (K-shell) hole and is therefore not sensitive to the neutron energy [19].

Simulation Geometry:

Simulations were performed for Gd$_2$O$_3$:Eu^{3+} with a layer thickness of 100 µm. The experimental samples were irradiated with a Deuterium-Deuterium (D-D) source emitting 2.5 MeV neutrons. To convert fast neutrons emitted by the source to thermal neutrons a 15 cm thick HDPE moderator cube was used. The neutrons passed through about 10 cm (between HDPE and detector) of air before hitting the samples. This same setup was used for the simulations.
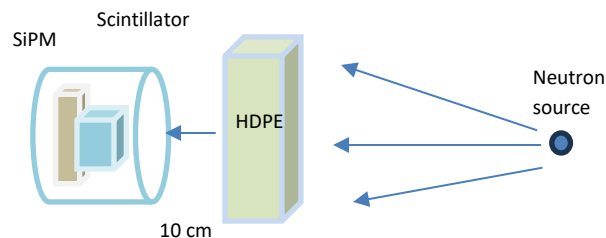

Figure 4.3 Simulated Geometry

Energy deposition density is expressed as GeV/cm^3 per primary. Neutron fluence is expressed as the number of particles (neutrons) particles/cm^2 per primary.

Neutron and Photon flux:

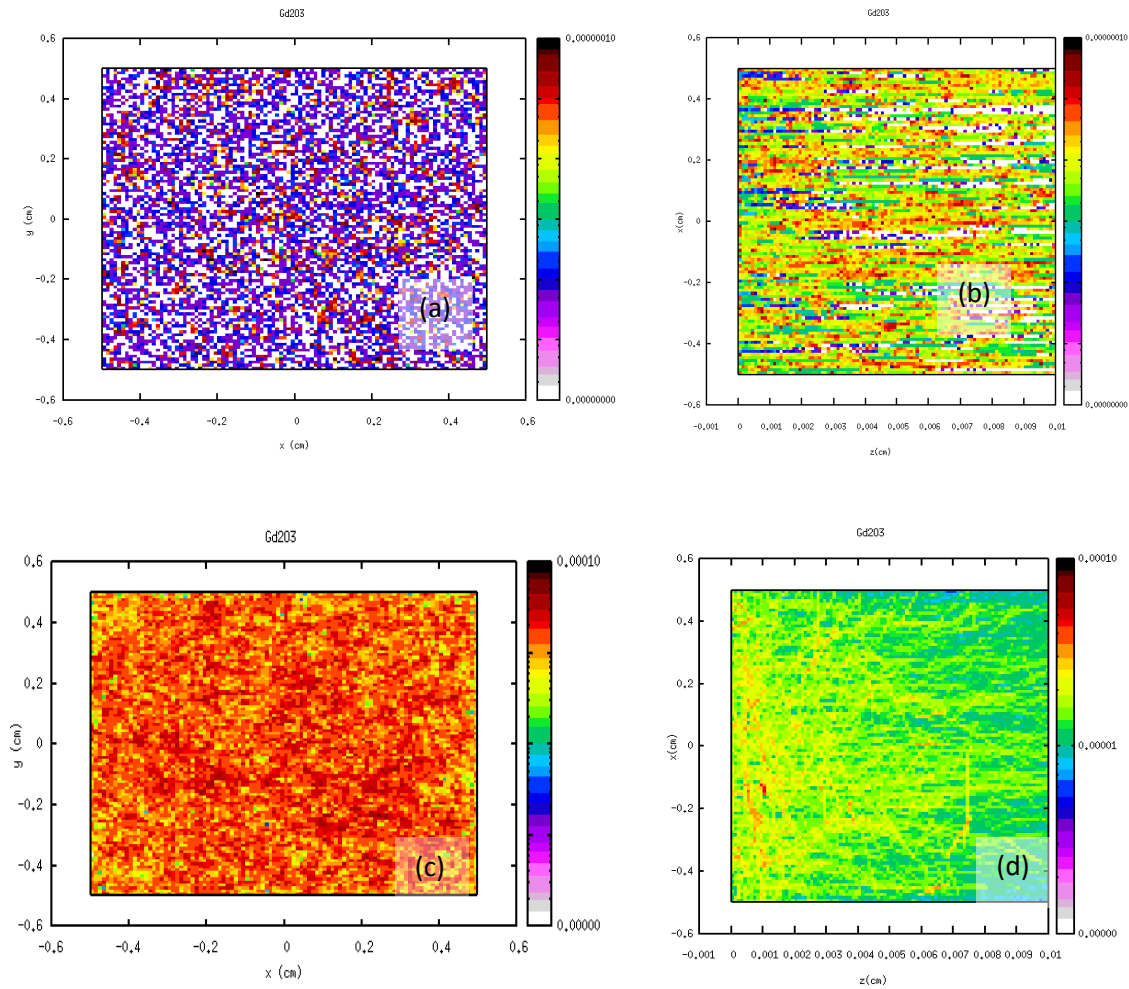*Figure 4.4 Gd$_2$O$_3$:Eu^{3+} (a) Energy deposition density at the surface (GeV/cm^3 per primary) (b) Energy deposition with depth (c) Photon fluence (1/cm^2 per primary) (d) Photon fluence variation with depth of the film*

Fig. 4.4 shows the energy deposition density when neutron flux (a) hit on the scintillator surface and (b) penetrates through the depth of the film. Fig. 4.4 (c) and (d) show the photon flux produced from the neutron absorption in these two cases respectively. As presented in Fig.4.4 (c), photon flux produced at the surface is high and flux is reducing along the depth of the thin film.

Therefore, to calculate the light passing through the boundary (the one-way fluence across the boundary) integrated over a solid angle, the USRBDX card was used. Results from USRBDX are given as double differential distributions.
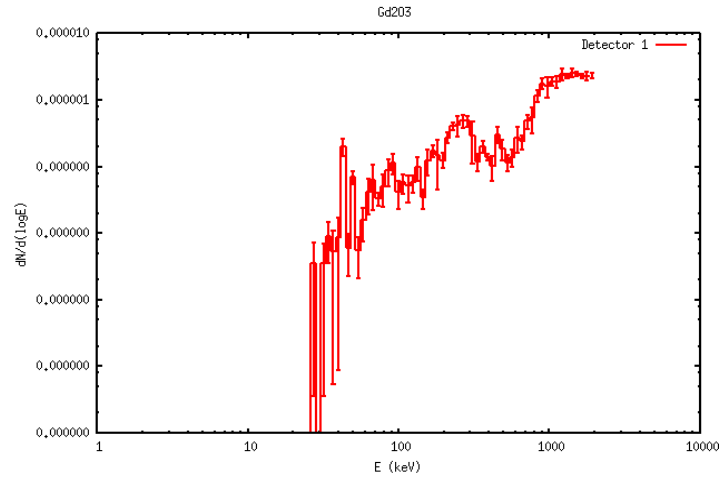

Figure 4.5 Gd$_2$O$_3$:Eu^{3+} Boundary crossing output-photons

Fig. 4.5 shows the number of photons transferred to the SiPM by travelling across the scintillator surface against the kinetic energy of all particles crossing the surface (in GeV per primary).

Energy spectrum

Fig. 4.6 shows the simulated energy spectrum for the scintillator and identifies peaks between 6 keV to 200 keV for 100 µm thick scintillation layer of Gd$_2$O$_3$:Eu^{3+}.
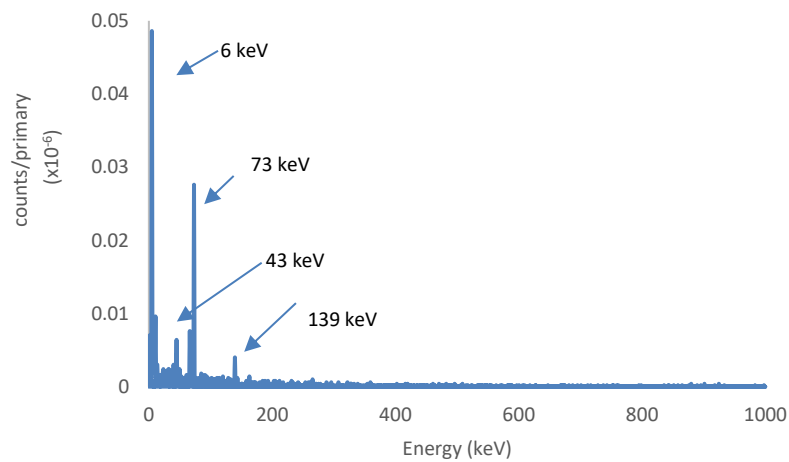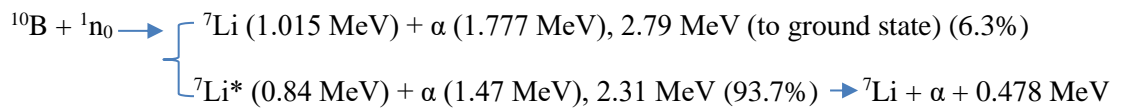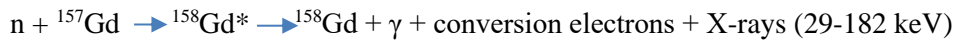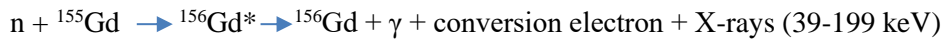

Figure 4.6 Simulated energy spectrum of Gd$_2$O$_3$:Eu^{3+}

Natural gadolinium (^{nat}Gd) comprises the 7 natural isotopes, out of which, ^{155}Gd and ^{157}Gd show the highest thermal cross sections for ^{nat}Gd. The products of reaction are two stable isotopes, ^{156}Gd* and ^{158}Gd* in excited states, of 8.536 MeV and 7.937 MeV respectively. The prompt gamma cascade is characterized with the maximum emission probability at around 2 MeV (Dumazert et al., 2018). A competitive mechanism to gamma emission is the IC process, mainly at low energies, with the maximum energy line at 246 keV (Harms and McCormack, 1974). Per neutron IC capture yield is around 0.12 and 0.48 for ^{155}Gd and ^{157}Gd respectively (Kandlakunta et al., 2013). Atoms in excited states, de-excite by emitting X-rays mainly around 40 keV to 50 keV for the K-shell and 6 keV to 7 keV for the L-shell and low energy Auger electrons.

4.4.2 GdBO$_3$:Eu^{3+}

For GdBO$_3$:Eu^{3+} film detectors, the neutron absorbing film acts to absorb neutrons and the following nuclear reactions are possible:

$n + {}^{155}Gd \longrightarrow {}^{156}Gd* \rightarrow {}^{156}Gd + \gamma$ + conversion electron + X-rays (39-199 keV)

$n + {}^{157}Gd \longrightarrow {}^{158}Gd* \rightarrow {}^{158}Gd + \gamma$ + conversion electrons + X-rays (29-182 keV)

$^{10}B + {}^1n_0 \longrightarrow$
  ^{7}Li (1.015 MeV) + α (1.777 MeV), 2.79 MeV (to ground state) (6.3%)
  ^{7}Li* (0.84 MeV) + α (1.47 MeV), 2.31 MeV (93.7%) $\rightarrow$ ^{7}Li + α + 0.478 MeV

Simulation Geometry:

For GdBO$_3$:Eu^{3+}, simulations were performed with a layer thickness of 100 µm. The experimental samples were irradiated with a Deuterium-Deuterium (D-D) source emitting 2.5 MeV neutrons. To produce thermal neutrons a 15 cm thick HDPE moderator cube was used. The neutrons passed through about 10 cm (between HDPE and detector) of air before hitting the samples. This same setup was used for the simulations.

Energy deposition density is expressed as GeV/cm^3 per primary. Neutron fluence, is expressed as number of particles (neutrons) particles/cm^2 per primary.

Neutron and Photon flux:

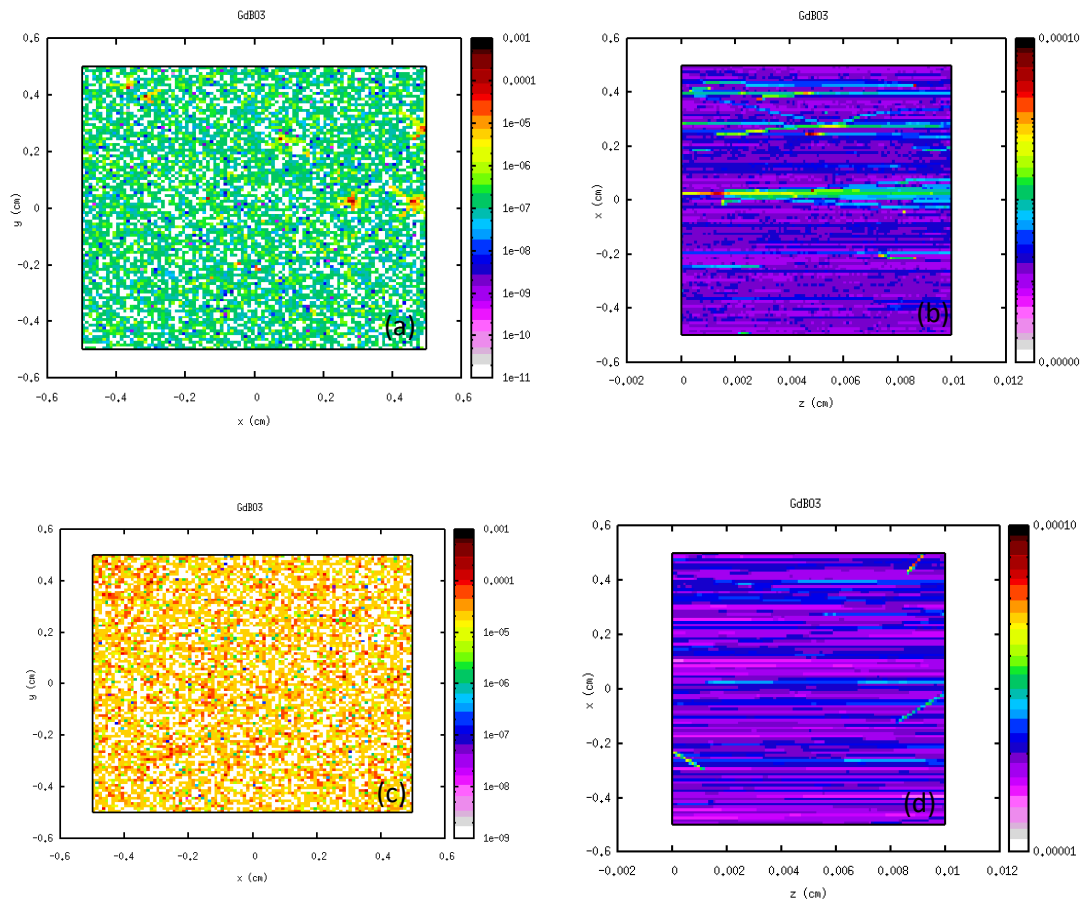*Figure 4.7. GdBO$_3$:Eu^{3+} (a) Energy deposition density at the surface (GeV/cm^3 per primary) (b) Energy deposition with depth (c) Photon fluence (1/cm^2 per primary) (d) Photon fluence variation with depth of the film*

Fig. 4.7 shows the energy deposition density when neutron flux (a) hit on the scintillator surface and (b) penetrates through the depth of the film. Fig. 4.7 (c) and (d) show the photon flux produced from the neutron absorption in these two cases respectively. As presented in Fig.4.7 (c), photon flux produced at the surface is high and flux is reducing along the depth of the thin film. To visualize the light passing through the boundary (the one-way fluence across the boundary) over an integrated solid angle, the USRBDX card was used.
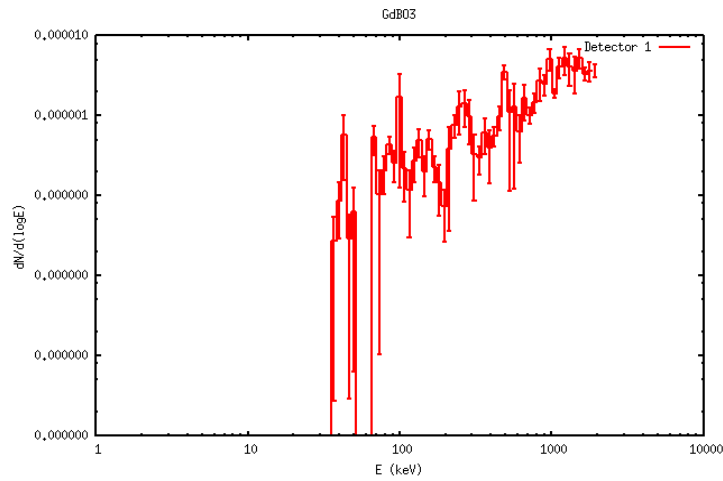
Figure 4.8. boundary crossing output -photon

Fig. 4.8 shows the number of photons transferred to the SiPM by travelling across the scintillator surface against the kinetic energy of all particles crossing the surface (in GeV per primary).
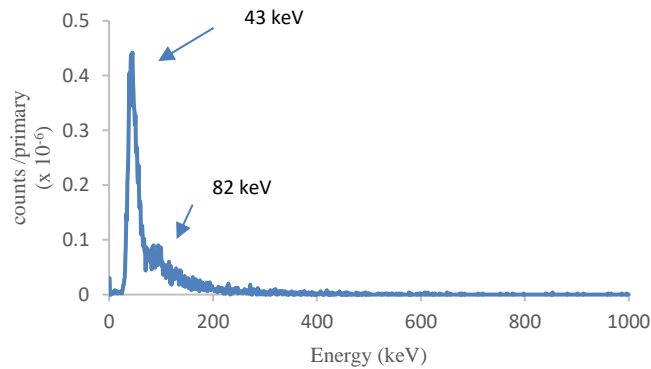
Energy spectrum

Figure 4.9. Simulated energy spectrum of GdBO$_3$:Eu^{3+}

As explained in previous section, a competitive mechanism to gamma emission is the IC process. Atoms in excited states, de-excite by emitting X-rays mainly between 40 keV to 50 keV for the K-shell and 6 keV to 7 keV for the L-shell and low energy Auger electrons. The combined 1st excited state to ground state transitions for ^{156}Gd and ^{158}Gd are each at ~82 keV.

42

4.4.3 $Li_6Gd(BO_3)_3:Eu^{3+}$

For $Li_6Gd(BO_3)_3:Eu^{3+}$ film detectors, the neutron absorbing film acts to absorb neutrons and following nuclear reactions are possible:

$n + {}^{155}Gd \rightarrow {}^{156}Gd^* \rightarrow {}^{156}Gd + \gamma +$ conversion electron + X-rays (39-199 keV)

$n + {}^{157}Gd \rightarrow {}^{158}Gd^* \rightarrow {}^{158}Gd + \gamma$ (7.9 MeV) + conversion electrons + X-rays (29-182 keV)

$^{10}B + {}^{1}n_0 \rightarrow$
- ^{7}Li (1.015 MeV) + α (1.777 MeV), 2.79 MeV (to ground state) (6.3%)
- $^{7}Li^*$ (0.84 MeV) + α (1.47 MeV), 2.31 MeV (93.7%) $\rightarrow$ $^{7}Li + \alpha$ + 0.478 MeV

$^{6}Li + {}^{1}n_0 \longrightarrow {}^{3}H$ (at 2.73 MeV) + α (at 2.05 MeV), 4.78 MeV
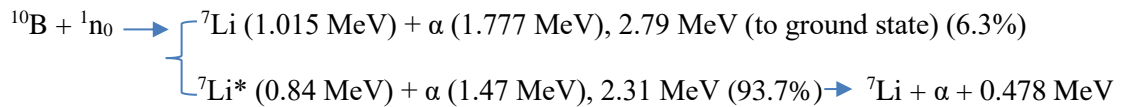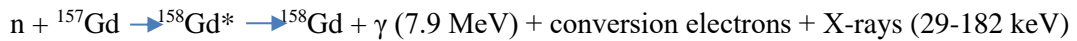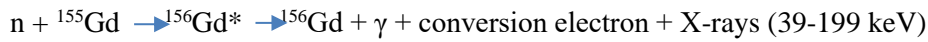
Simulation Geometry:

Simulations were performed with a layer thickness of 100 µm. The experimental samples were irradiated with a Deuterium-Deuterium (D-D) source emitting 2.5 MeV neutrons. To produce more thermal neutrons a 15 cm thick HDPE moderator cube was used. The neutrons passed through about 10 cm (between HDPE and detector) of air before hitting the samples. This same setup was used for the simulations.

Energy deposition density is expressed as GeV/cm^3 per primary. Neutron fluence, is expressed as number of particles (neutrons) $particles/cm^2$ per primary.
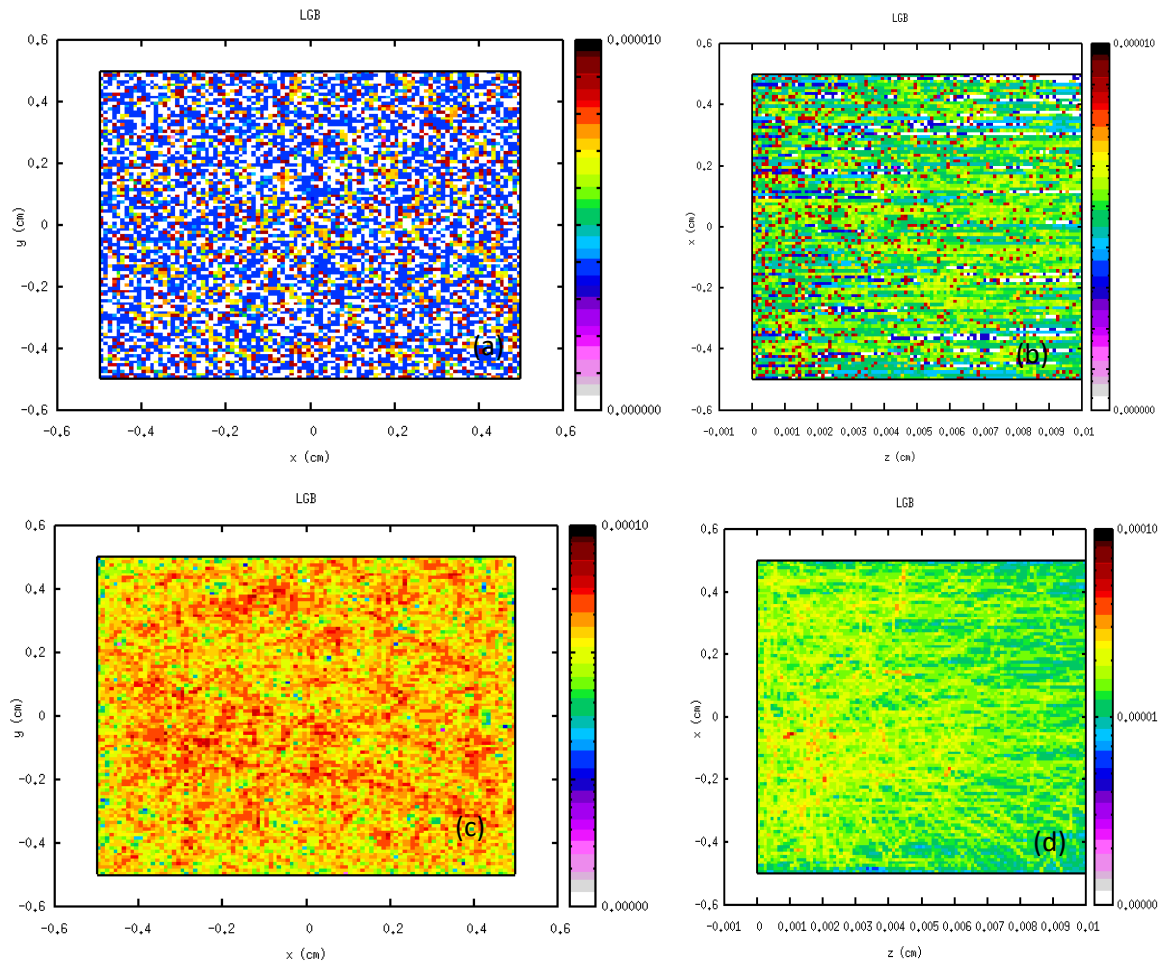
Neutron and Photon flux:

Figure 4.10. Li₆Gd(BO₃)₃:Eu³⁺ (a) Energy deposition density at the surface (GeV/cm³ per primary) (b) Energy deposition with depth (c) Photon fluence (1/cm² per primary) (d) Photon fluence variation with depth of the film

Fig. 4.10 shows the energy deposition density when neutron flux (a) hit on the scintillator surface and (b) penetrates through the depth of the film. Fig. 4.10 (c) and (d) show the photon flux produced from the neutron absorption in these two cases respectively. As presented in Fig.4.10 (c), photon flux produced at the surface is high and flux is reducing along the depth of the thin film. To visualize the light passing through the boundary (the one-way fluence across the boundary) over an integrated solid angle, the USRBDX card was used.

44
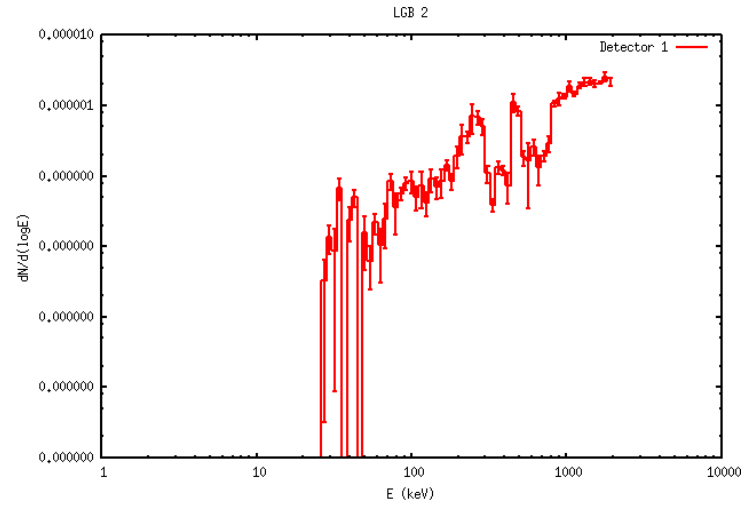
Figure 4.11 boundary crossing output -photons

Fig. 4.11 shows the number of photons transferred to the SiPM by travelling across the scintillator surface against the kinetic energy of all particles crossing the surface (in GeV per primary).

Energy spectrum

Figure 4.12. Simulated energy spectrum of Li₆Gd(BO₃)₃ :Eu³⁺

As explained in the previous two sections, atoms in excited states, de-excite by emitting X-rays mainly between 40 keV to 50 keV for the K-shell.

4.4.4 Hexagonal Boron (h-BN)

The boron containing layer (h-BN) in a neutron detector must be thick enough (tens of µm) to capture the incoming neutron flux, yet sufficiently thin (a few µm) to allow the daughter particles (α and Li) to penetrate th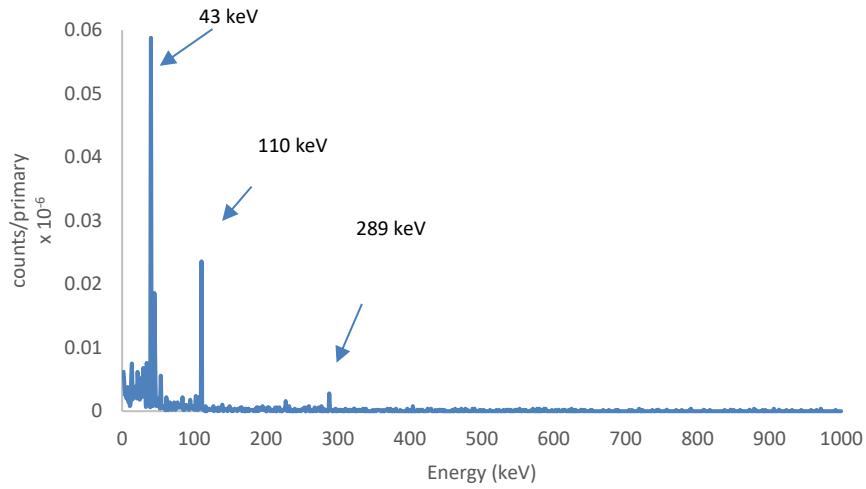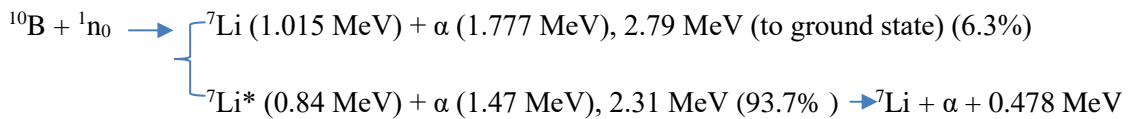e semiconductor later to generate electron hole pairs. For film detectors, the neutron absorbing film acts to absorb neutrons and following nuclear reactions occur:

$^{10}B + {}^1n_0 \longrightarrow$ ^7Li (1.015 MeV) + α (1.777 MeV), 2.79 MeV (to ground state) (6.3%)

$^7Li^*$ (0.84 MeV) + α (1.47 MeV), 2.31 MeV (93.7%) ➔ ^7Li + α + 0.478 MeV

Simulation Geometry:

Simulations were performed with a layer thickness of 1 µm. The experimental samples were irradiated with an Americium Beryllium (^{241}Am/Be) source. To convert fast neutrons to thermal neutrons a HDPE moderator was used. Distance between neutron source and detector is 50 cm. This same setup was used for the simulations. Energy deposition density is expressed as GeV/cm^3 per primary. Neutron fluence, is expressed as number of particles (neutrons) particles/cm^2 per primary.

Neutron and Photon flux:

Fig. 4.13 shows the energy deposition density when neutron flux (a) hit on the scintillator surface and (b) penetrates through the depth of the film. Fig. 4.13 (c) and (d) show the photon flux produced from the neutron absorption in these two cases respectively. As presented in Fig.4.13 (c), photon flux produced at the surface is high and flux is reducing along the depth of the thin film. But the photon flux generated in the h-BN layer is very low compared to other films mentioned above.
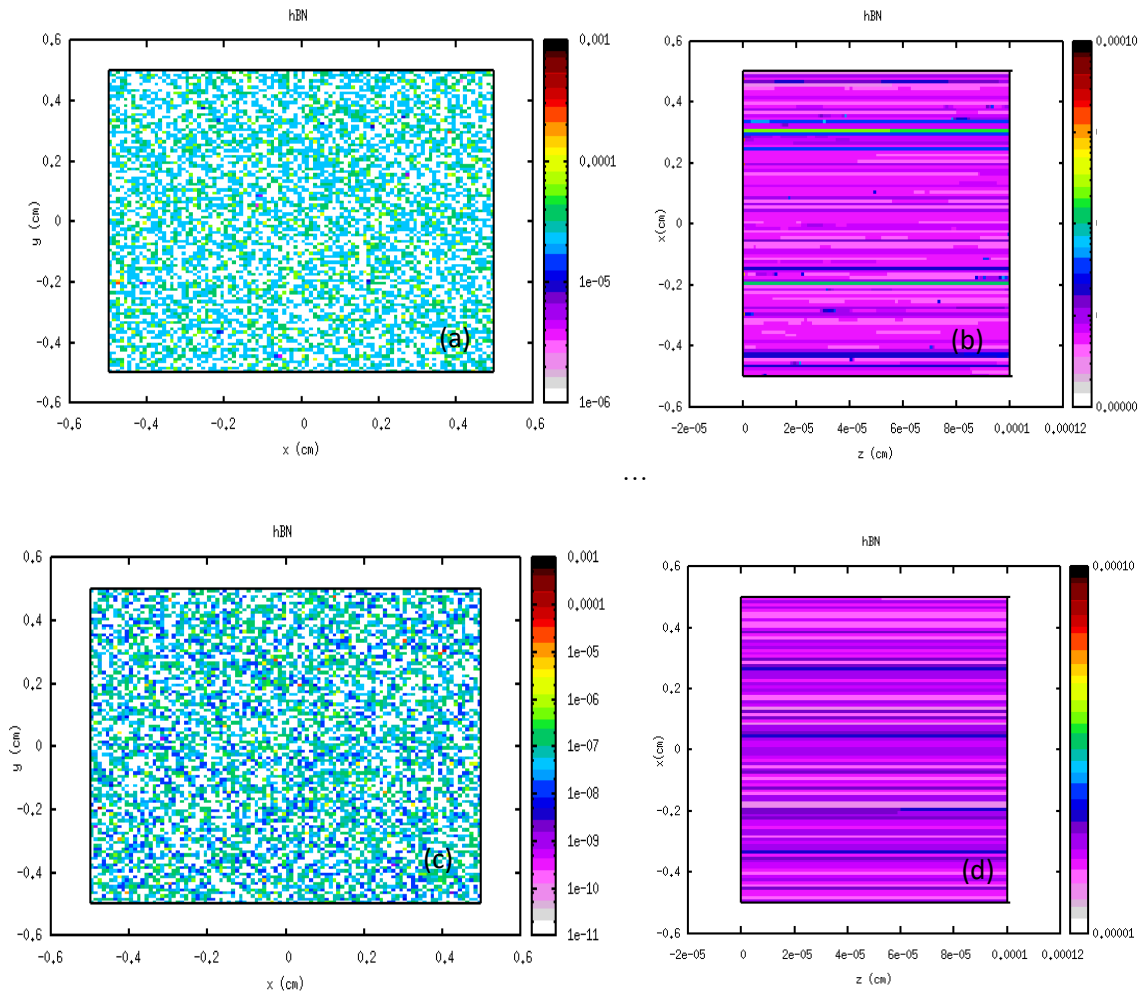
Figure 4.13 h-BN (a) Energy deposition density at the surface (b) Energy deposition with depth (c) Photon fluence (d) Photon fluence variation with depth of the film
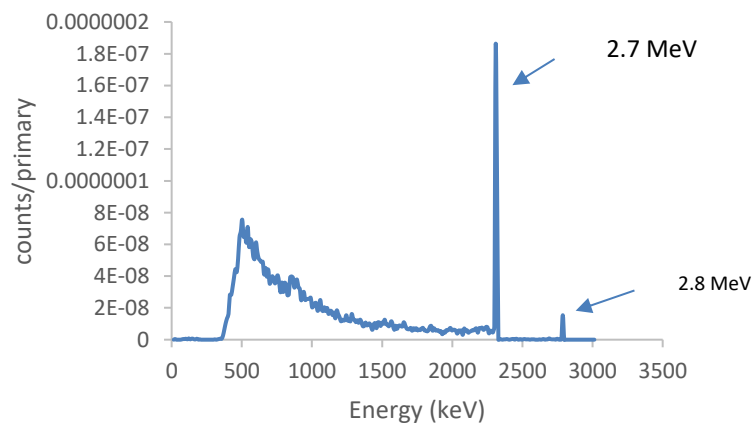
Energy spectrum

Figure 4.14 Energy Spectrum of h-BN

47

Fig. 4.14 shows the simulated energy spectrum for the scintillator, and peaks from Boron (0.48, 2.3, and 2.8 MeV) are visible.

4.5 Simulations for Gamma radiation

In this section, simulation results are present for single crystal scintillators. The objective of this study was to generate the response function of single crystal scintillators for gamma-rays accurately as possible.

In the simulations, each gamma source was defined as isotopic point source and was placed 5 cm away from the detector. A simulation was performed for each radiation source separately. The pulse height distributions of the detector were obtained for each gamma source in the energy range 59 keV to 662 keV. The photon pulse height distribution, the energy resolution, and other effects related to the SiPM detector were not considered in the FLUKA simulations. The broadening of the photopeak expected was not included in the spectra obtained by the DETECT card in FLUKA due to one of the main factors impacting the broadening coming from the electronic circuit used for the detector [54]. Therefore, obtained values by the FLUKA simulation were converted to a real detector response using the sigma values calculated theoretically.

Details of the conversion process to pulse height distribution

The DETECT card records the amount of deposited energy per scintillation event. The number of counts produced in the crystal or thin film scintillator versus energy is obtained in the FLUKA calculations; the energy deposition spectrum in these detectors behaves according to Poisson statistics. If the mean number of scintillation events generated is N, the statistical fluctuation in that number is given as:

$$\sigma = \sqrt{N} \qquad\qquad (4.1)$$

The standard deviation given in Eq. (4.1), can be expressed in terms of deposited energy as follows:

$$\sigma(E) = \sqrt{E_m} . \sqrt{E} \tag{4.2}$$

Where E is the average deposited energy in the crystal after the scintillation events. E_m is the smallest energy value measured and it was determined to be 1 keV in the FLUKA calculations. If we are only concerned with fluctuations in the signal, the response function approximates a Gaussian shape because N is large. The FWHM for a Gaussian distribution is given by:

$$FWHM = 2\sqrt{2ln2} . \sigma \tag{4.3}$$

$$R = \frac{FWHM}{E_0} \tag{4.4}$$

Where E_0 is the peak energy of the photopeak.

The single peaks obtained by FLUKA calculations were converted to real detector response through the conversion process. The Gaussian distribution fits for the photopeak in presented spectra were made using σ values calculated from Eq. (4.2).

4.5.1 YSO:Ce scintillator crystal

The single peaks obtained by FLUKA calculations were converted to real detector response through the conversion process mentioned above and fits the Gaussian distribution to the photopeak in spectra for resolution calculation.
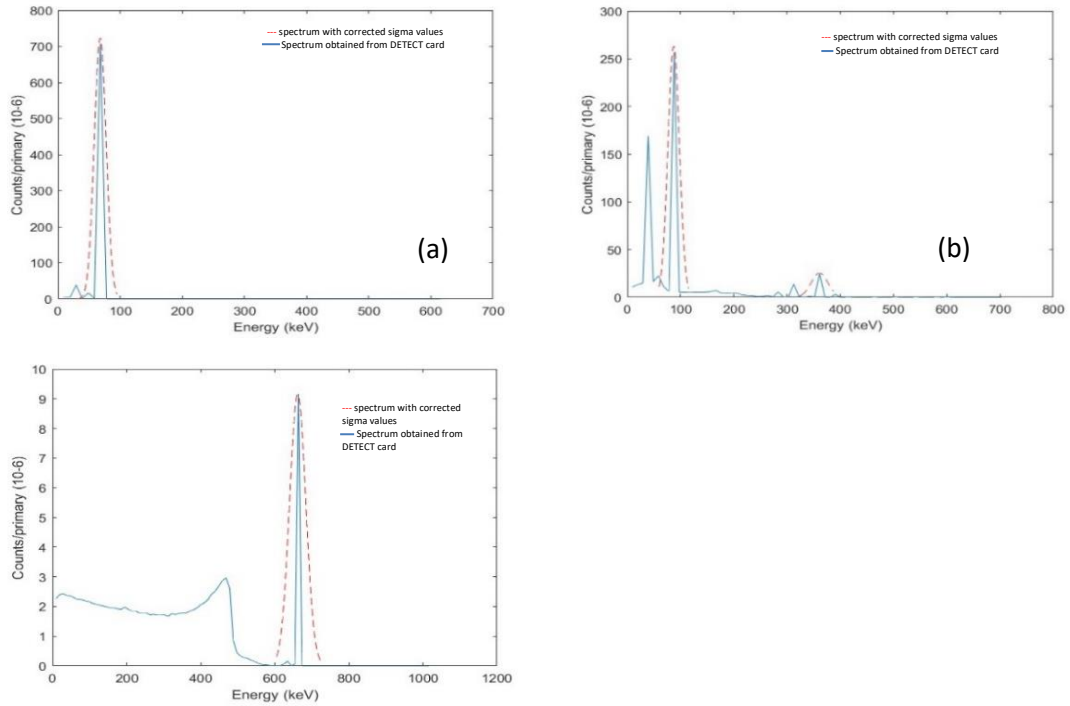
Figure 4.15 Simulated spectrum for YSO:Ce (a) Am-241 (b) Ba-133 (c) Cs-137 spectrum

The spectrum presented in blue lines shows the obtained spectra by the DETECT card. The red dotted lines in the spectrum were drawn by using these corrected sigma values.

Calculated energy resolutions in terms of FWHM (equation 4.3) and R% are presented in Table 4.2.

Table 4.2 Energy resolution of YSO:Ce detector

Energy (keV)	FLUKA	
	FWHM (Calculated)	Energy resolution (R%)
59.5	19.04	32.0
356.0	31.02	8.7
661.7	44.60	6.7

Similarly, calculations were carried out for the other two detectors, LYSO:Ce and GAGG:Ce.

4.5.2 LYSO:Ce Scintillator crystal

Within the inorganic scintillator class, cerium doped lutetium yttrium orthosilicate LYSO:Ce crystal is prominent. The distance between the scintillator and gamma source was 5 cm. Am-241, Ba-133 and Cs-137 isotopic point sources were used for the simulations.

Figure 4.16 Simulated spectrum for LYSO:Ce (a) Am-241 (b) Ba-133 (c) Cs-137 spectrum

Calculated energy resolutions in terms of FWHM and R% are presented in Table 4.3.

Table 4.3 Energy resolution of LYSO:Ce detector

Energy (keV)	FLUKA	
	FWHM (Calculated)	Energy resolution (R%)
59.5	16.2	27.2
356.0	38.2	10.7
661.7	58.0	8.7

4.5.3 GAGG:Ce Scintillator crystal

For GAGG:Ce, simulations were performed for a 5×5×5 mm^3 scintillator crystal. The distance between the scintillator and the gamma source was 5 cm. Cs-137, Am-241 and Ba-133 isotopic sources were used for the simulations.
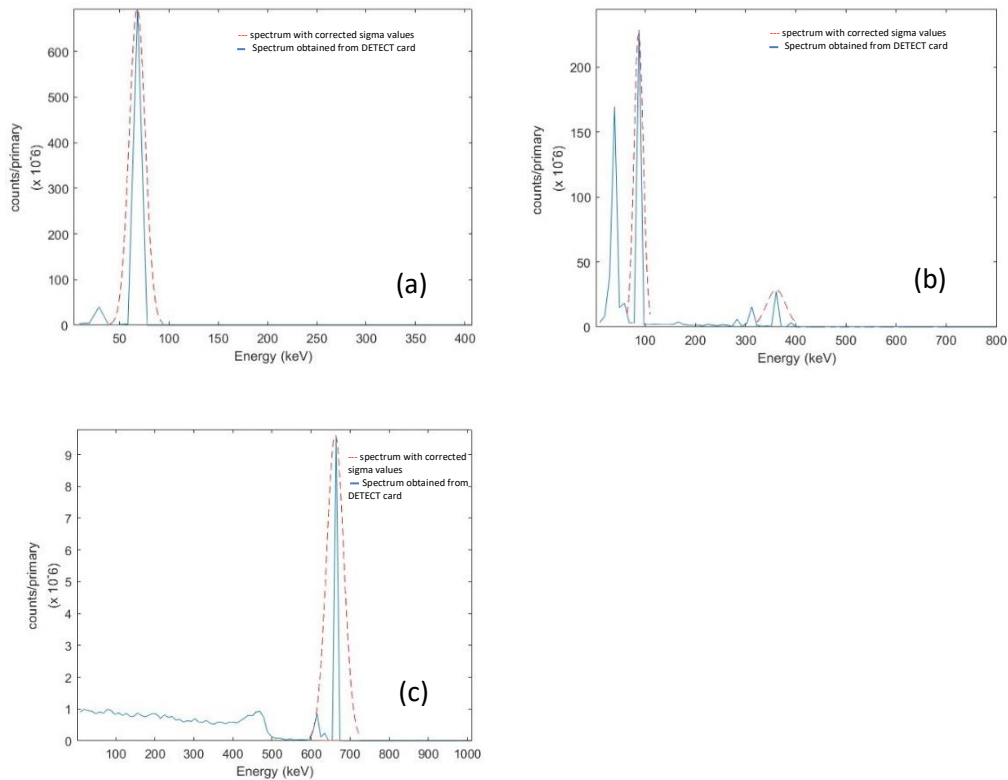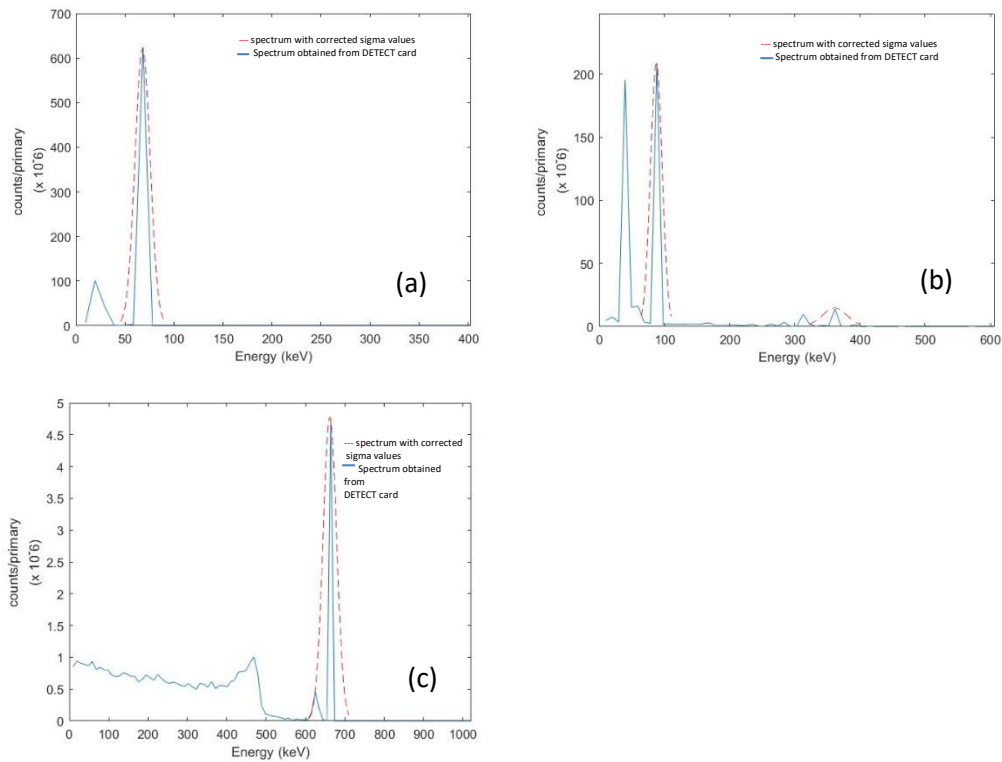

Figure 4.17 Simulated spectrum for GAGG:Ce (a) Am-241 (b) Ba-133 (c) Cs-137 spectrum

Calculated energy resolutions in terms of FWHM and R% are presented in Table 4.4.

Table 4.4 Energy resolution of GAGG:Ce detector

Energy (keV)	FLUKA	
	FWHM (Calculated)	**Energy resolution (R%)**
59.5	15.4	25.9
356.0	38.0	10.6
661.7	48.0	7.25

A comparison with experimental results is presented in Chapter 5.

4.6 Results and Discussion

Thin film scintillators:

After the Gd neutron capture event, excited states of the resultant ^{156}Gd* and ^{158}Gd* nuclei are relatively low lying-in energy. In excited states, due to relatively high atomic number of gadolinium ($Z = 64$), this leads to internal conversion electron emission leaving vacancies in the atomic shells, orbital electron shuffling occurs leading to the emission of characteristic X-rays, which is a competing process to gamma-ray emission, mainly at low energies, with the maximum energy line at 246 keV. Therefore, neutron capture process of natural gadolinium produces characteristic X-rays as well as prompt gamma rays. In simulated spectra, X-rays mainly between 40 keV to 50 keV for the K-shell and 6 keV to 7 keV for the L-shell are visible. A peak at $\sim$82 keV is also visible.

A comparison with experimental results is presented in Chapter 6.

Single crystal scintillators:

In this work, the energy resolution and FWHM values were calculated for the 59-661.7 keV energy range using the simulated spectra. The expected broadening of the photopeak is not included in the spectra obtained by FLUKA simulation due to one of the main factors impacting the broadening coming from the electronic circuit used for the detector. Therefore, obtained values by the FLUKA simulation were converted to a real detector response using the sigma values calculated theoretically.

Chapter 5

Study 2

Gamma ray detection with SiPM

This chapter presents a brief overview of scintillation detectors, the interactions of gamma rays with materials, and the YSO, LYSO and GAGG scintillator crystals, which were used in this work. Simulation and experimental studies are then presented along with a comparative investigation of the performance of YSO, LYSO and GAGG scintillation crystal readout with a SiPM for the detection of low activity gamma rays. Emission spectra, energy calibration, and energy resolution are discussed and measured.

5.1. Scintillation detectors

Scintillation detectors are based on scintillator materials, which produce secondary low-energy photons, typically in the visible spectrum, as a response to high-energy incident radiation. The scintillator is attached to a photodetector, a PMT tube or Silicon Photomultiplier (SiPM), which converts the scintillator light into an electrical signal. Different scintillator materials provide different features in terms of time response, resolution, detection efficiency, sensitivity to different radiation types, and detection area. When ionizing radiation interacts with a scintillator material, a fluorescent flash, called scintillation, is produced.

5.1.1. Interaction with gamma rays

In gamma ray detection, scintillation is the result of the excitation of bound electrons, produced by three types of mutual interactions: photoelectric effect, Compton effect, and pair production. The probability of occurrence of these interactions is dependent on the scintillator type, and energy of the gamma ray.

In the photoelectric effect, an incident gamma ray is absorbed, and a photoelectron is emitted from one of the electron shells of the absorber atom [51], as shown in Fig. 5.1 (a). The photoelectron with an energy E_{e-} given by:

$$E_{e-} = hv - E_b \qquad (5.1)$$

Where hv is the energy of the incoming gamma ray, and E_b the binding energy of the shell from which electron is emitted.

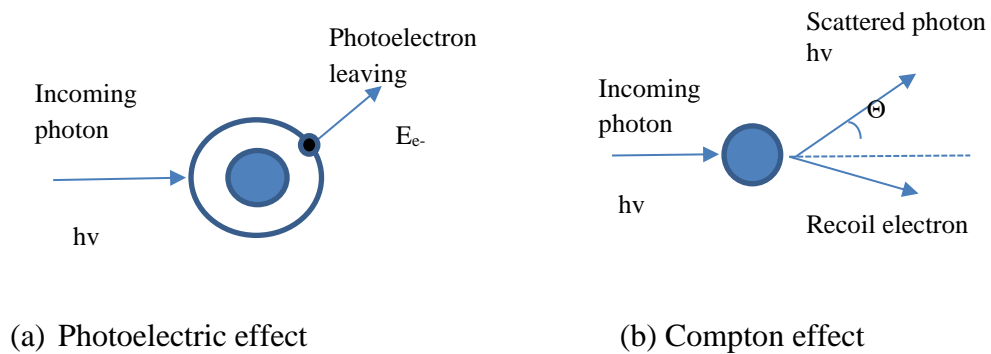(a) Photoelectric effect (b) Compton effect

Figure 5.1 Schematic of (a) Photoelectric effect and (b) Compton effect

The vacancy created by the electron emission can be filled by other electrons while releasing the binding energy either in the form of a characteristic X-ray or an Auger electron. Thus, the result of the photoelectric absorption is the ejection of a photoelectron, carrying most of the gamma ray energy, followed by one or more low energy electrons, generated by the absorption of the original binding energy of the photoelectron. Therefore, the energy spectrum of the photoelectric effect is typically a single peak (photopeak) with a total electron energy corresponding to the energy of the incident gamma ray. The amount of scintillation photons produced by the photoelectric effect is proportional to the gamma ray energy [55].

In the Compton effect, the incident gamma ray photon scatters along with an electron in the absorbing material. As presented in Fig. 5.1 (b), in this scattering phenomenon, the incoming gamma ray photon is deflected by an angle θ with respect to its original direction of travel. Hence, the photon transfers only a portion of its energy to the emitted

electron, called a recoil electron. The remaining energy of the scattered photon $h\nu_0$, assuming that the recoil electron is initially at rest, is given by:

$$hv' = hv \cdot \frac{1}{1+\alpha(1-\cos{(\theta)})} \tag{5.2}$$

Where hv is the energy of the incoming photon, θ is the deflection angle, and α is given by:

$$\alpha = \frac{hv}{m_0 c^2} \tag{5.3}$$

Where $m_0 c^2$ is the rest mass of the electron, 0.511 MeV.

The kinetic energy of the recoil electron is given by:

$$E_{e-} = hv - hv' \tag{5.4}$$

A continuum of energy can be transferred to the electron, from zero up to the maximum energy, because all scattering angles can occur in a Compton scatter. When $\theta = \pi$, the maximum energy is transferred to the electron. Even then, the pulses are smaller than those that contribute to the photopeak. Therefore, in the energy spectrum this corresponds to the so-called Compton edge.

In pair production, a photon passing near the nucleus of an atom, is subjected to strong field effects from the nucleus and may be absorbed. The photon energy is fully converted in an electron-positron pair, e− and e+, which are created in the energy/mass conversion of the incoming photon. The pair production process may occur when the incoming photon has an energy hv >1.022 MeV, because the energy needed to create one e⁻/e⁺ pair at rest is 2×0.511 MeV. The kinetic energy of the produced particles is:

$$E_{e-} + E_{e+} = hv - 1.022 \tag{5.5}$$

Usually, this kinetic energy is lost inside the material after a travel of few millimetres.

The annihilation photons are emitted by the annihilation of e$^+$, which are generated by the primary photon, and can interact with the detector or escape. The double escape peak occurs when both annihilation photons escape without interaction in the detector. The single escape peak occurs when one photon escapes but the other is totally absorbed.

In high Z materials, the photoelectric effect dominates at low energy, and pair production dominates at high energy. On the other hand, in low Z materials Compton scattering dominates at medium energy.
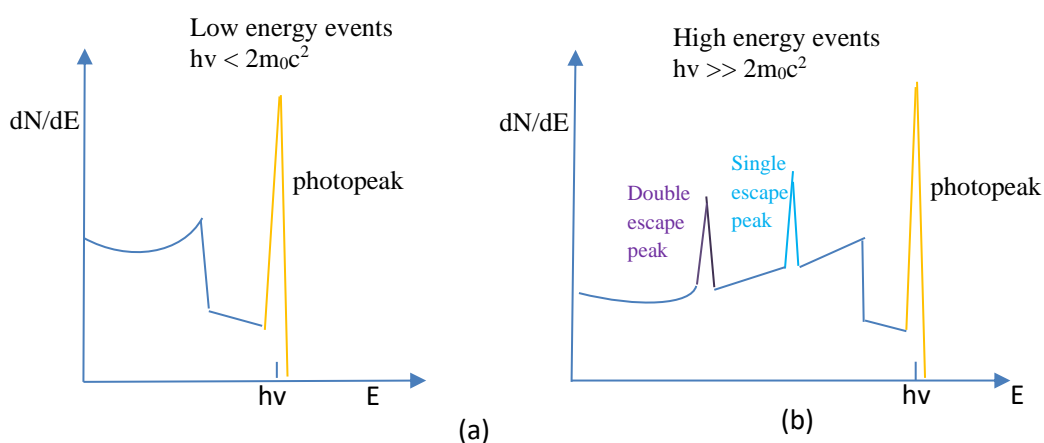

Figure 5.2 Example of the response of a scintillator detector (a) Low energy events (b) High energy events

The spectrum shown in Fig. 5.2 (a) relates to low energy events, illustrating the photoelectric effect and Compton edge. The spectrum shown in Fig. 5.2 (b) illustrates the situation for high energy events, showing pair production and Compton edge.

5.2. Single crystal scintillators

The last decade has seen the introduction of several new high luminosity scintillators with a range of different scintillation properties such as high light yield, high energy resolution, high effective atomic number, fast scintillation response, chemical stability, and large crystal growth [56-60]. Additionally, scintillator crystals are non-

hygroscopic, rugged, and inexpensive to manufacture demonstrating their potential for use as efficient and cost-effective inorganic scintillators for radiation detection.

The choice of the scintillator material is fundamental in a detector because it has an impact on the detection efficiency, the energy resolution, and the time resolution.

Within the inorganic scintillator class, the best combination of these factors is achieved by cerium-doped materials, such as silicates, cerium-doped lutetium-yttrium orthosilicate (LYSO:Ce) and cerium doped yttrium orthosilicate, Y_2SiO_5:Ce (YSO:Ce) [56, 59, 60]. Also, cerium-activated oxide materials based on garnet structure are promising. This family of scintillators includes the recent discovery of single crystal multicomponent garnet scintillator, cerium-doped gadolinium aluminium gallium garnet (GAGG:Ce) [57, 58]. The peak emission for YSO:Ce, LYSO:Ce and GAGG:Ce is at around 420 nm, 420 nm and 530 nm respectively, which is suitable for use with semiconductor-based photodetectors such as SiPMs. The properties of these scintillation crystals are summarized in Table 5.1 [61].

Table 5.1 Properties of scintillator crystals

Scintillator	LYSO:Ce	GAGG:Ce	YSO:Ce
Composition	$Lu_{1.9}Y_{0.1}SiO_5$:Ce	$Gd_3Al_2Ga_3O_{12}$:Ce	Y_2SiO_5:Ce
Effective Z	66	54	35
Density (g/cm³)	7.25	6.63	4.4
Wavelength of peak emission (nm)	420	540	420
Light output (photons/MeV)	29,000	50,000	26,300
Decay time (ns)	45	88	42
Self-radiation	Yes	No	No
Hygroscopic	No	No	No

YSO:Ce, LYSO:Ce and GAGG:Ce scintillator crystals from EPIC Crystals, China, were used for this study. According to the manufacturer, the nominal cerium doping level of YSO:Ce, LYSO:Ce and GAGG:Ce are 0.5 mol%, 0.5 mol% and 0.3 mol% respectively.

Table 5.2 Features of scintillators

Scintillator	Size	Ce %
YSO:Ce	5×5×5 mm³	0.5 mol
LYSO:Ce	5×5×1 mm³	0.5 mol
GAGG:Ce	5×5×1 mm³	0.3 mol

5.3 Experimental Measures

In this study, to measure the emission spectra, scintillator crystals were coupled with a custom designed SiPM MCA from Bridgeport Instruments (model no: SIPM 1K_BC36_H50) with peak spectral sensitivity at around 420 nm which matches closely with the peak emission of the two scintillator crystals used. To maximize light collection, the scintillator crystal was optically coupled by a light guide to the SiPM. The pulse height distribution of each detector was obtained for each gamma source in the energy range 59 keV to 661.7 keV, and the energy resolution was calculated.

The radiation sources used for these experimental activities are listed in Table 5.3.

Table 5.3. Radioactive sources used in experimental activities

Radiation Source	Expected γ-ray or x-ray energy (keV)	Current activity (μCi)
Cs-137	32.2, 661.7	0.445
Am-241	59.5	0.998
Ba-133	31.0, 81.0, 276.4, 302.9, 356.0	0.129

The energy resolution (FWHM) for electron energy (E) can be obtained with the following equation by assuming the square root of the energy dependency:

$$FWHM = \frac{FWHM_0}{\sqrt{E/E_0}} \qquad (5.6)$$

Where, E_0 is the peak centroid respectively for the peak width of the source [62].

The detector resolution as a percentage can be defined as:

$$R\% = 100 \times \frac{FWHM}{Eo} \qquad (5.7)$$

5.3.1 Cerium doped yttrium orthosilicate, YSO:Ce

A typical Cs-137, Ba-133 and Am-241 spectrum recorded for 1 hour with a YSO:Ce cubic crystal is presented in Fig.5.3.
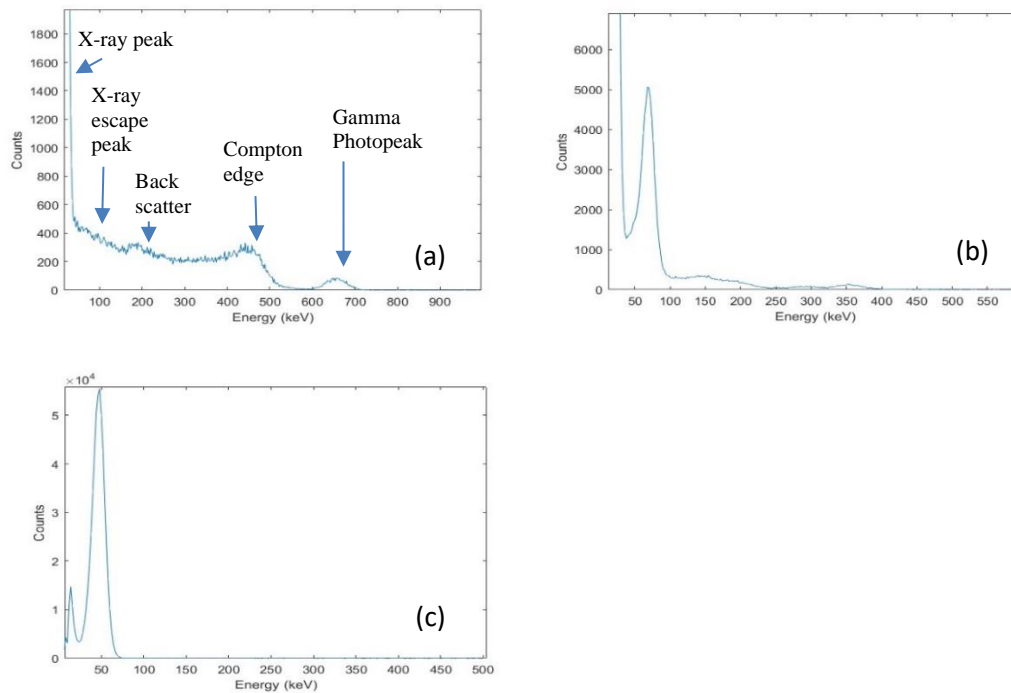

Figure 5.3 Energy spectrum of YSO:Ce (a) Cs-137, (b) Ba-133 and (c) Am-241

It can be observed that all the key features of the Cs-137 spectrum, the X-ray photopeak from decaying to Ba-137, the X-ray peak from decaying to Pb$_{k\alpha,\beta}$, the backscatter peak at around 200 keV, the Compton edge and photopeak, are present. For low activity Ba-133, the X-ray peak, the escape peak and photopeak are visible. In the energy spectrum obtained for low activity Am-241, the photopeak is visible alongside a low energy peak at around 17 keV.

The detector energy resolutions calculated by using Eq. (5.6) and Eq. (5.7) are presented in Table 5.4.

Table 5.4 Energy resolution of YSO:Ce

Peak Energy (keV)	FWHM	Energy resolution (R%)
48.0	15.3	31.8
70.0	18.6	26.5
354.0	33.9	9.5
660.0	48.8	7.4

5.3.2 Cerium-doped lutetium-yttrium orthosilicate, LYSO:Ce

The background radiation spectrum (BKG) of the LYSO:Ce scintillator is significant. Fig. 5.4 shows the BKG spectrum obtained without the presence of any external radioactive materials and was collected over a period of 1 hour.
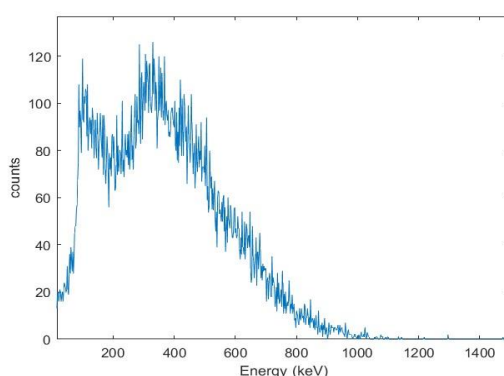

Figure 5.4 LYSO background spectrum

With a low dose rate of 0.009 µSv/hr, the result is related to the intrinsic activity of ^{176}Lu, which undergoes β-decay to excited states of ^{176}Hf (β-particle energy of 593 keV) leading to simultaneous detection of the β-particle plus 88 keV γ-ray, β-particle plus 202 keV γ-ray, and β-particle plus 307 keV γ-ray, respectively. Thus, broad peaks, due to beta continuum, would be expected at 88, 290 (88 + 202), 395 (88 + 307) and 597 (88 + 202 + 307) keV due to β-particles and internal conversion electrons depositing their whole energy within the crystal [63].

Therefore, the BKG spectrum is subtracted from each emission spectrum of LYSO:Ce crystals and presented in Fig. 5.5 (for Cs-137, Ba-133 and Am-241 respectively). It can be observed that all the key features of the Cs-137 spectrum, the X-ray photopeak from decaying to Ba-137, the X-ray peak from decaying to Pb$_{k\alpha,\beta}$, the backscatter peak at around 200 keV, the Compton edge and photopeak, are present. For low activity Ba-

133, the X-ray peak, escape peak and photopeak are visible. In the energy spectrum obtained for low activity Am-241, the photopeak is visible alongside the peak at around 20 keV.
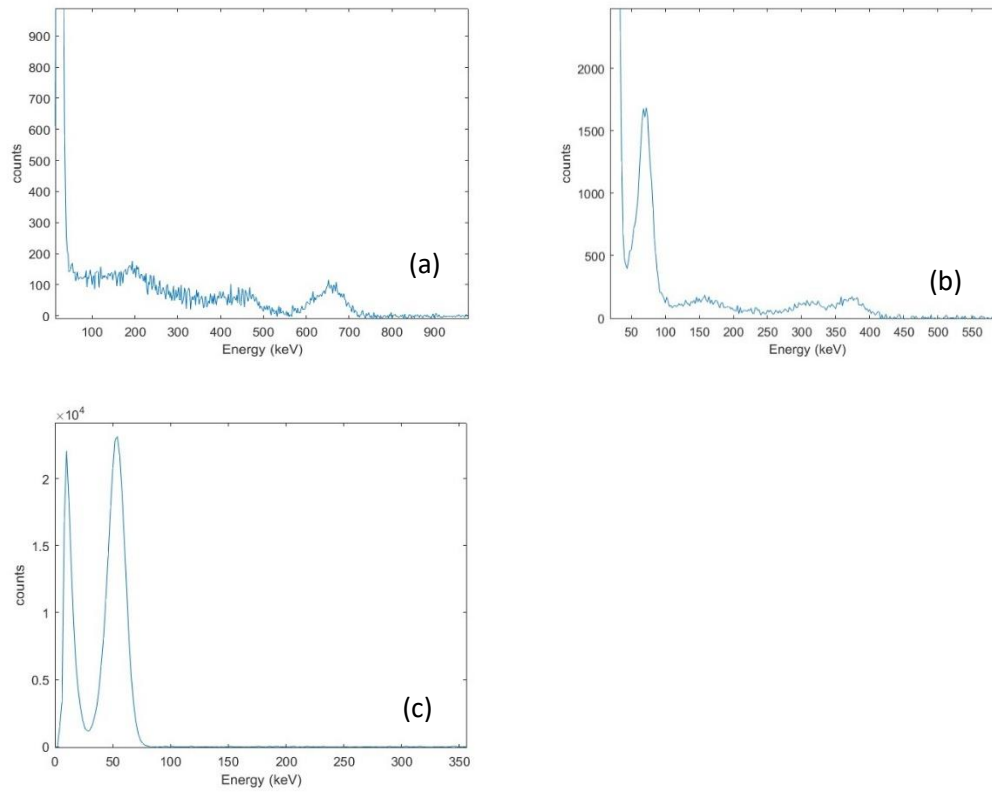

Figure 5.5 Energy spectrum of LYSO:Ce (a) Cs-137, (b) Ba-133 and (c) Am-241

Energy resolutions calculated using Eq. (5.6) and E1. (5.7) are presented in Table 5.5.

Table 5.5 Energy resolution of LYSO:Ce

Peak Energy (keV)	FWHM	Energy resolution (R%)
54.2	16	28.1
70.1	18	23.9
368.0	46	12.6
670.0	70	9.9

5.3.3 Cerium-doped gadolinium aluminium gallium garnet, GAGG:Ce

A typical Cs-137, Ba-133 and Am-241 spectrum recorded for 1 hour with a GAGG:Ce cubic crystal is presented in Fig. 5.6.
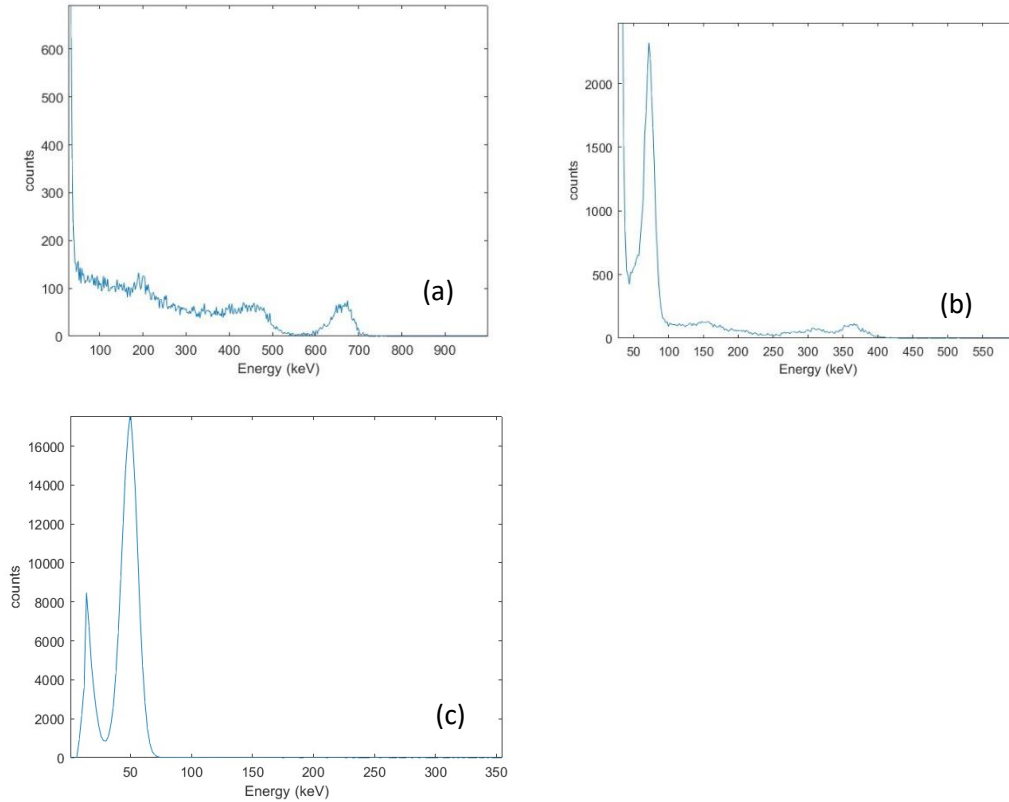
Figure 5.6 Energy spectrum of GAGG:Ce (a) Cs-137 (b) Ba-133 and (c) Am-241

It can be observed that all the key features of Cs-137 spectrum, the X-ray photopeak from decaying to Ba-137, the X-ray peak from decaying to $Pb_{k\alpha,\beta}$, the backscatter peak at around 200 keV, the Compton edge and photopeak, are present. For low activity Ba-133, the X-ray peak, escape peak and photopeak are visible. In the energy spectrum obtained for low activity Am-241, the photopeak is visible alongside the peak at around 19 keV.

Energy resolutions calculated using Eq. (5.6) and Eq. (5.7) are presented in Table 5.6.

Table 5.6 Energy resolution of GAGG:Ce

Peak Energy (keV)	FWHM	Energy resolution (R%)
50.1	14.4	26.3
72.0	16.0	20.9
362.0	34.0	9.4
664.0	52.0	6.9

5.4. Neutron testing

The thermal neutrons used in this section were produced from an AmBe source located within a moderating HDPE. Neutron interactions occur within GAGG:Ce quite often, due to its high content of Gd.
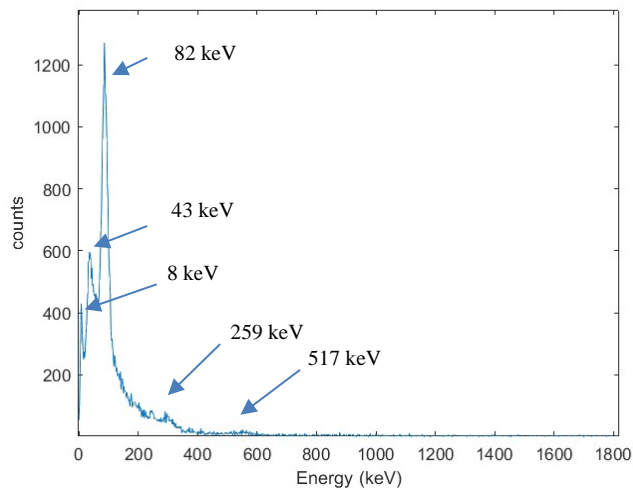

Figure 5.7 Response of GAGG:Ce scintillator for AmBe source following irradiation for 10 minutes

The [241]Am/Be spectra for the 1 mm thick GAGG:Ce scintillator crystal is shown in Fig. 5.7 with several of the key features marked. The combined 1st excited state to ground state transitions for [156]Gd and [158]Gd at ~82 keV is the most prominent peak and is well separated from a lower energy peak at ~43 keV. In addition, two higher energy peaks are also observed at ~259 keV and ~517 keV. Similar spectra were observed by Reeder et al. and Taggart et al. [64, 65] and an explanation of their origins was initially presented there. The 82 keV peak is the combination of the 88.9 keV and 79.5 keV gamma rays from the 1st excited states of [156]Gd and [158]Gd, which cannot be separately determined. The energy peak at ~43 keV is due to internal conversion decays occurring within the GAGG scintillator from the 1st excited states. In Fig. 5.7 a gamma peak is also observed at ~259 keV, and results from the rotational band structure of both [156]Gd and [158]Gd in which the 4^+ state de-excites in sum-coincidence through the 2^+ state to the ground state. The resulting gamma peak is due to the combination of these transitions from both [156]Gd and [158]Gd isotopes. The thinner scintillator no longer has the stopping power to fully resolve the ~517 keV peak but the other features remain.

Further, GAGG:Ce detector was exposed to Deuterium-Deuterium (D-D) neutron source (2.5 MeV) and following spectrum is observed.
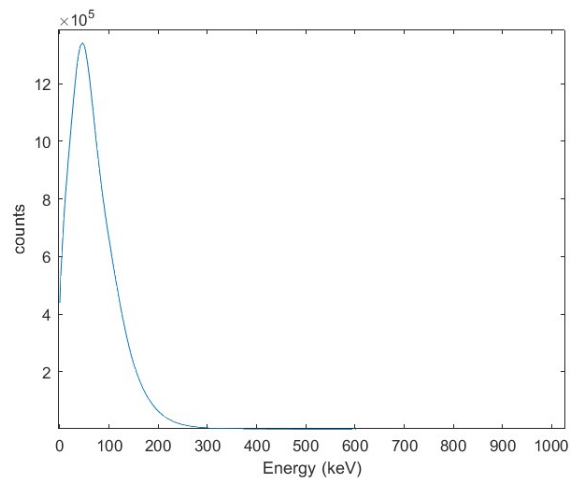

Figure 5.8. Response of GAGG:Ce scintillator for D-D source for 10 min

In the spectrum, peak around 43 keV is visible.

5.5 Results and discussions

The direct spectrum from Cs-137 shows a 32 keV X-ray photopeak from decaying to Ba-137, an 85 keV X-ray peak from decaying to $Pb_{k\alpha,\beta}$, a backscatter peak at around 200 keV, a Compton edge and a 662 keV photopeak. For low activity Ba-133, an X-ray peak, an escape peak and photopeak are visible at 31 keV, 81 keV, 303 keV, 356 keV. The direct spectrum from Am-241 shows the expected gamma peak (59.5 keV) and characteristic L X-ray peak (17.8 keV) from decaying to Np. If both or one of the annihilation photons of the pair production escapes from the detector volume, double or single escape peaks appear in the gamma spectrum.

In the experimental spectrum, a small peak shift is observed due to the adjustment of the operating voltage of the SiPM for each scintillator type, i.e. 34.5 V for GAGG:Ce and 35.1 V for LYSO:Ce, to adjust the gain controls of the detector. The main disadvantage of LYSO detector is intrinsic radioactivity caused by the β-decay of ^{176}Lu radionuclide (with a natural abundance of 2.6%) followed by a prompt gamma ray

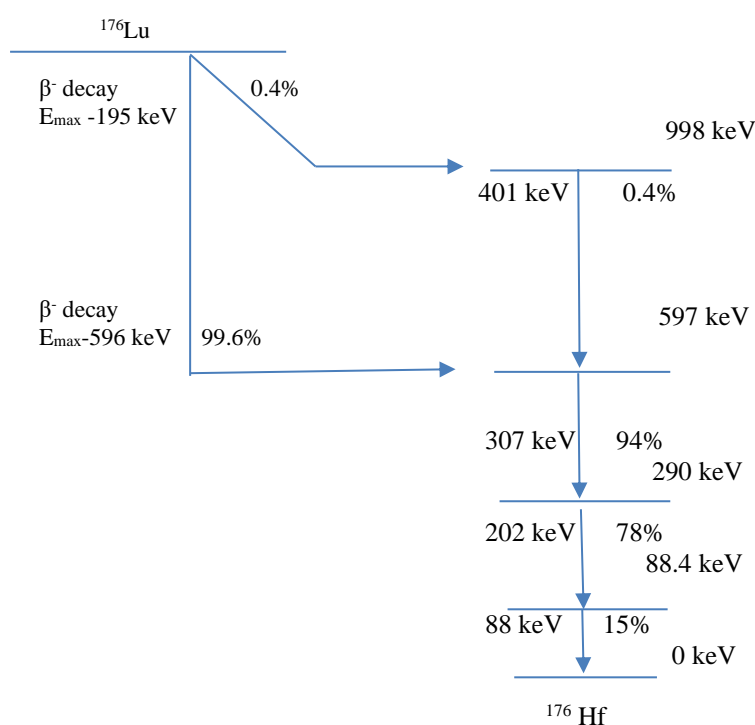cascade at energies of 307 keV and 202 keV. The simplified decay scheme of ^{176}Lu is shown in Fig. 5.7.

A comparison of detector resolutions calculated by simulation and from experimental studies is presented in Table 5.7. The energy resolution is measured for photon energies of 59 keV to 661.7 keV.

Table 5.7 Energy resolution comparison

Energy (keV)		Experimental				FLUKA simulated		
		^{241}Am	^{133}Ba			^{137}Cs	^{241}Am	^{133}Ba	^{137}Cs
		59.5	**81.0**	**356.0**	**661.7**			
LYSO:Ce	FWHM$_0$	16.0	18.0	46.0	68.0	16.2	38.2	58.0
	E$_0$	54.2	70.1	368.0	664.0	59.5	356.0	661.7
	R%	28.1	23.9	12.6	10.2	27.2	10.7	8.7
GAGG:Ce	FWHM$_0$	14.0	16.0	34.0	52.0	15.4	38.0	48.0
	E$_0$	50.1	72.0	362.0	664.0	59.5	356.0	661.7
	R%	25.6	20.9	9.4	7.8	25.9	10.6	7.25
YSO:Ce	FWHM$_0$	15.3	18.6	33.9	48.8	19.0	31.0	44.6
	E0	48.0	70.0	354.0	660.0	59.5	356.0	661.7
	R%	31.8	26.5	9.5	7.4	32.0	8.7	6.7

The pulse height distributions of the detectors were obtained for each gamma source in the energy range 59 keV to 662 keV, and the energy resolution was calculated.
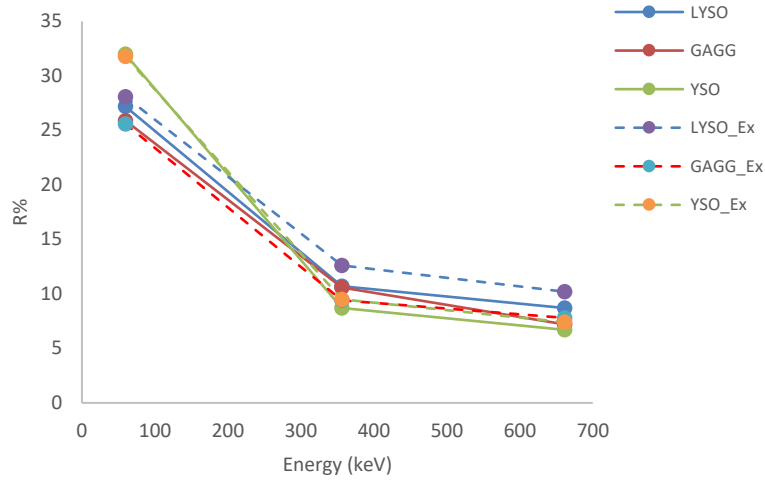

Figure 5.10 Comparison of experimental and simulation results. Solid lines correspond with simulated energy resolution while dashed lines correspond to experimental ('Ex') energy resolution.

As shown in Table 5.8, the difference between simulated energy resolution values and experimentally obtained values is less than a factor of 2. It was also observed that the relative percentage difference between the experimental and simulation resolution values was within 15% for all three types of scintillator crystal at all three source energies.

The relative difference (RD%) between the resolution calculated from FLUKA (*A*) and the resolution obtained by experimental results (*B*), were determined using the following equation:

$$RD\% = \frac{A-B}{B} \cdot 100\% \qquad\qquad (5.7)$$

Table 5.8 Relative difference

Scintillator	Energy (keV)	R% simulated	R% experimental	Difference	RD%
LYSO:Ce	59.5	27.2	28.1	0.9	3.2
	356.0	10.7	12.6	1.9	15.0
	661.7	8.7	10.2	1.5	14.7
GAGG:Ce	59.5	25.9	25.6	0.3	1.1
	356.0	10.6	9.4	1.3	12.7
	661.7	7.2	7.8	0.6	7.6
YSO:Ce	59.5	32.0	31.8	0.2	0.6
	356.0	8.7	9.5	0.8	8.4
	661.7	6.7	7.4	0.7	9.4

This study showed that the FLUKA code also can be used to determine the energy resolution and can therefore be of benefit in terms of reducing financial cost and time in the development of new scintillators and radiation sensors.

Chapter 6

Study 3

Material Preparation

6.1. Introduction

Neutrons have mass but no electrical charge and they therefore cannot directly produce ionization in a detector, and therefore cannot be directly detected. This means that neutron detectors must rely upon a conversion process where an incident neutron interacts with a nucleus to produce a secondary charged particle. These charged particles are then directly detected and from them the presence of neutrons is deduced.

In typical radiation detectors, scintillators are the luminescent material, which act as energy converters by absorbing the incident radiation and converting it to a photon signal. Based on photon counting applications, an ideal scintillator material should have high stopping power for a given thickness (high material density and high atomic number), fast scintillation response after excitation (fast emission intensity decay), a good spectral match with the readout device (appropriate emission wavelength), high conversion efficiency of the incident radiation (high light yield), linear light response with incident radiation dose (proportionally), robustness and stability to physical and chemical changes (radiation resistance and non-hygroscopicity), and high spatial resolution across the scintillator area (thin micrometre layers). All these properties are yet to be found in a single material with a simple and cost-effective growth technique. Since the appropriate procedures to obtain such materials are still being developed, scintillator properties are usually compromised for a specific radiation detector application [66].

This section of the thesis focuses on examining a possible method to engineer an effective scintillator for neutron detection. $Gd_2O_3{:}Eu^{3+}$, $GdBO_3{:}Eu^{3+}$, $Li_6Gd(BO_3)_3{:}Eu^{3+}$ and h-BN scintillators were prepared and tested with neutrons.

6.2. Material preparation

In this work, $Gd_2O_3:Eu^{3+}$, $GdBO_3:Eu^{3+}$ and $Li_6Gd(BO_3)_3:Eu^{3+}$ phosphor materials were successfully synthesized through simple precipitation processes and subsequent annealing. The h-BN + ZnO scintillator was prepared using RF sputtering [67, 68].

The chemicals described throughout this section are gadolinium oxide (99.5%, A.M.P.E.R.E. Industrie, France), europium oxide (99.5%, AMR, China), urea, boric acid (99.5%, Fisons Scientific Equipment), HNO_3 (Fisher Scientific), lithium carbonate, isopropanol, and phosphor medium (7153E, DUPONT).

6.2.1. Europium doped gadolinium oxide, $Gd_2O_3:Eu^{3+}$

The $Gd(NO_3)_3$ stock solution (0.25 M) was prepared by dissolving Gd_2O_3 in dilute HNO_3

To suitable amounts of $Gd(NO_3)_3$ stock solution, europium nitrate as well as urea were added in a beaker, dissolved and diluted to 500 ml by deionized water. The concentrations of Gd^{3+}, Eu^{3+} and urea in the final solution were 0.025 and 0.5 M respectively; Eu^{3+}/Gd^{3+} was 5 mol%, which is referred to as the 'standard solution' in subsequent methods described below. The solution was kept boiling on a hot plate until turbidity was observed, the solution was then aged for 1 hr.

The precipitates were then washed using deionized water several times and filtered. The water and precipitates were separated by using a centrifuge. The precipitates were then dried at 110˚C in an oven, and soft white powders resulted. To convert these powders to phosphors, they were pre-fired at 980˚C overnight.

To investigate the relationship between luminescence and firing temperature the samples were fired at three different temperatures (800˚C, 980˚C and 1050˚C).
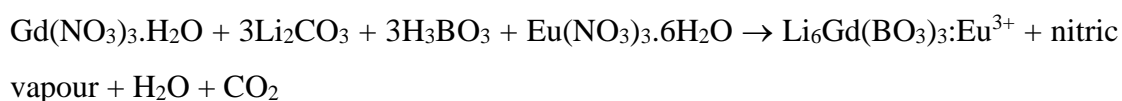
6.2.2. Europium doped gadolinium borate, GdBO$_3$:Eu^{3+}

To suitable amounts of Gd(NO$_3$)$_3$ stock solution, europium oxide (Eu$_2$O$_3$) as well as H$_3$BO$_3$ were added in a beaker. The mixture was stirred at 60˚C until it formed a clear solution. 30 g of urea was then added to the solution. Precipitation then started immediately. The precipitates were washed using deionized water several times and filtered. The precipitates were then dried at 110˚C in an oven, and soft white powders resulted. To convert these powders to phosphors, they were pre-fired at 800˚C overnight.

To investigate the relationship between luminescence and firing temperature the samples were fired at three different temperatures (800˚C, 980˚C and 1050˚C).

6.2.3. Europium doped lithium gadolinium borate, Li$_6$Gd(BO$_3$)$_3$:Eu^{3+}

The europium doped lithium gadolinium borate samples were synthesized by means of chemical reaction.

To synthesize the Li$_6$Gd(BO$_3$)$_3$:Eu^{3+} phosphor stoichiometric amounts of Gd(NO$_3$)$_3$ and Eu(NO$_3$)$_3$ stock solutions were added to a beaker and heated to 60˚C while stirring. To the solution were then added the required amounts of Li$_2$CO$_3$ and H$_3$BO$_3$. When the solution became clear the following reaction was complete:

Gd(NO$_3$)$_3$.H$_2$O + 3Li$_2$CO$_3$ + 3H$_3$BO$_3$ + Eu(NO$_3$)$_3$.6H$_2$O $\rightarrow$ Li$_6$Gd(BO$_3$)$_3$:Eu^{3+} + nitric vapour + H$_2$O + CO$_2$

The precipitate was then washed with deionized water several times and filtered at the pump. The precipitates were then dried at 60˚C in an oven and the resulting soft white phosphor precursor powders annealed at 550˚C for 16 hours producing the luminescent phosphor powder. To investigate the relationship between luminescence and firing temperature the samples were fired at two different temperatures (550˚C and 800˚C). K-bar printing was used to prepare thin films from the powders. The luminescence spectrum of the Li$_6$Gd(BO$_3$)$_3$:Eu^{3+} was obtained using photoluminescence analysis, the laser used has a wavelength of 532 nm and a 1% neutral-density filter in place.

Thin film preparation

0.5 g of $Gd_2O_3:Eu^{3+}$ powder was mixed with binder (phosphor medium) using a speed mixer for 20 s at 3300 rpm. A fine paste of $Gd_2O_3:Eu^{3+}$ was formed. Scintillator layers were then deposited on glass substrate by K-bar technique. Substrates were then dried at 60˚C in an oven. Before deposition, the glass substrate was cleaned by ethanol. Similarly, thin scintillator layers of $GdBO_3:Eu^{3+}$, $Li_6Gd(BO_3)_3:Eu^{3+}$ were prepared.

6.2.4. h-BN

h-BN films were prepared by using a Mantis magnetron sputtering and e-beam deposition system. All substrates were cleaned ultrasonically in acetone and then in isopropyl alcohol (IPA) followed by deionized water before being loaded into the deposition chamber. The deposition of the h-BN films was performed using RF magnetron sputtering, with a sputtering power of 60 W. During the sputtering deposition processes, the background pressure was typically 5×10^{-4} Pa and the working gas pressure was 1 Pa. The sputtering target was a 2" h-BN target with a purity of 99.99% (Sigma Aldridge).

The target was first pre-sputtered for 30 minutes for cleaning purposes with a shutter placed between the target and the substrate. During the pre-sputtering stage, the substrates were heated to 25, 60, and 100°C. The deposition duration was 4 hr for all samples to deposit ∼400 nm QCM layer thickness in each case.

The quartz crystal microbalance (QCM) parameters used for the h-BN deposition were as follows:

Density $(\rho) = 2.25$ g/cm^3

Acoustic impedance $(Z) = $ Density $(\rho) \times$ Velocity (v)

Velocity $(v) = 23.1 \times 10^3$ m/s [65]

Acoustic impedance $= 23.1 \times 2.25 \times 10^3 \times 10^2$ g cm^{-2} s^{-1}

$$= 51.975 \times 10^5 \text{ g cm}^{-2} \text{ s}^{-1}$$

Similarly, a 100 nm thick ZnO layer was also deposited on h-BN.

6.3. Characterization of Physical Properties

The surface morphology of the $Gd_2O_3:Eu^{3+}$, $GdBO_3:Eu^{3+}$ and $Li_6Gd(BO_3)_3:Eu^{3+}$ samples was examined by scanning electron microscopy (SEM) and the fluorescence spectra were obtained by photoluminescence analysis.

The laser was focused on the sample surface through a convex lens. After the laser interact with the sample, emit electromagnetic waves collected by a light collector and received by a spectrometer.
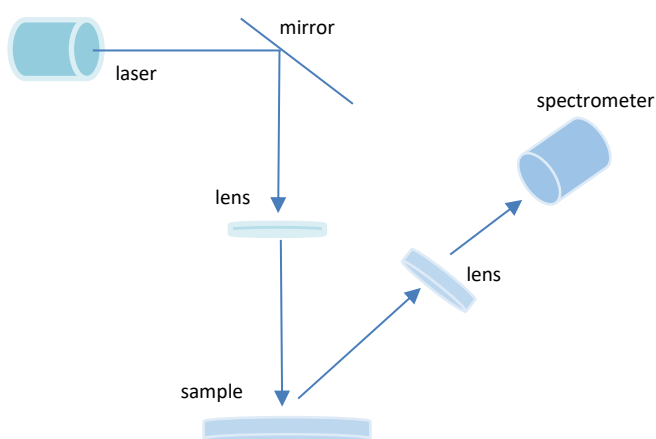

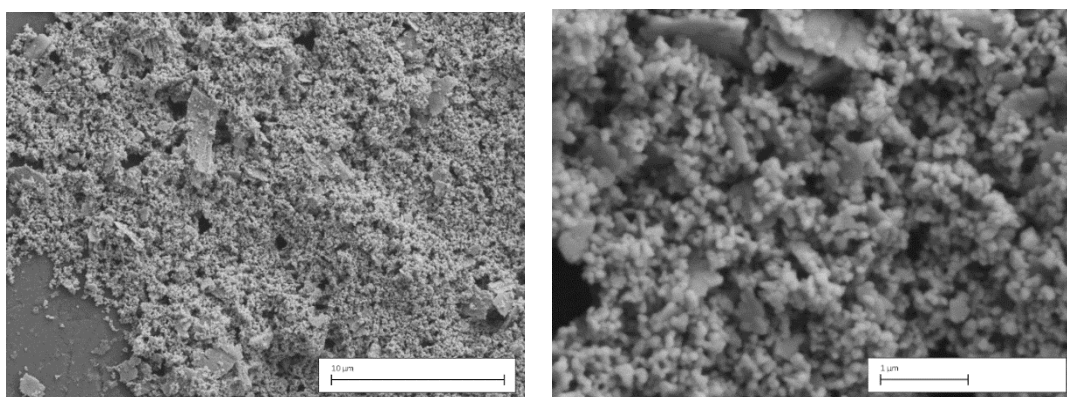*Figure 6.1 Schematic of photoluminescence analysis*

6.3.1. $Gd_2O_3:Eu^{3+}$

Figure 6.2 SEM images of $Gd_2O_3:Eu^{3+}$

Fig. 6.2 presents SEM micrographs of a $Gd_2O_3:Eu^{3+}$ sample fired at 980℃. The $Gd_2O_3:Eu^{3+}$ precursors prepared by the standard method have an approximately spherical shape with a diameter of about 0.1 μm.
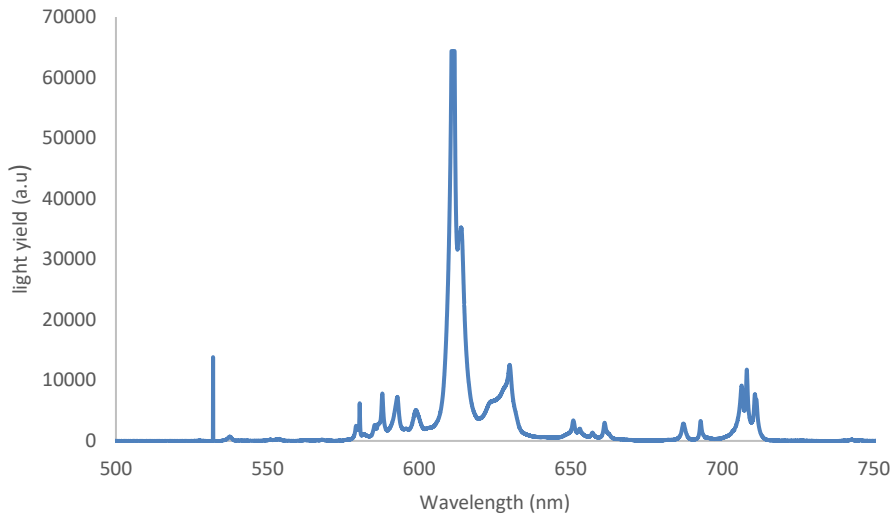
Figure 6.3 Fluorescence spectra of Gd$_2$O$_3$:Eu^{3+} at 980 ˚C (laser is at 532 nm with 1% filter)

The charged particles emitting from the (n, γ) reactions on ^{155}Gd and ^{157}Gd consequently excite Eu^{3+} ions and result in the characteristic Eu^{3+} emission peaking at around 612 nm that corresponds to the transition of electrons from 5d $\rightarrow$ 7f energy levels. The spectrum consists of 5 sets of lines at 580 nm, 587-600 nm, 611-630 nm, 651-661 nm, and 687-710 nm, which are connected to the intra-configurational ^{5}d$_0$ $\rightarrow$ ^{7}f$_0$, ^{5}d$_0$ $\rightarrow$ ^{7}f$_1$, ^{5}d$_0$ $\rightarrow$ ^{7}f$_2$, ^{5}d$_0$ $\rightarrow$ ^{7}f$_3$ and ^{5}d$_0$ $\rightarrow$ ^{7}f$_4$ transitions of Eu^{3+}, respectively. The strongest emission was observed for the ^{5}d$_0$ $\rightarrow$ ^{7}f$_2$ transition, followed by the ^{5}d$_0$ $\rightarrow$ ^{7}f$_4$ transition.
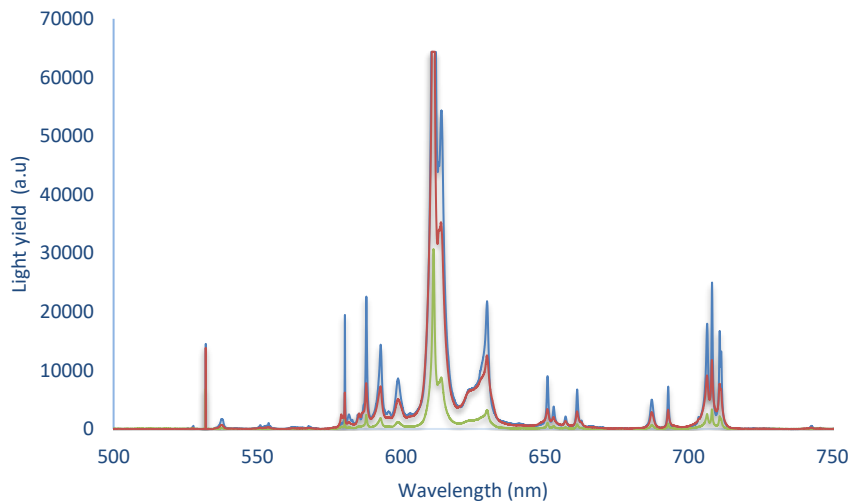

Figure 6.4 Fluorescence spectra of Gd$_2$O$_3$:Eu^{3+} samples fired at 700 (green), 980 (red) and 1050 ˚C (blue) (laser is at 532 nm with 1% filter and saturated at 65000).

74

For samples fired at 700-1050˚C, the luminescence increased dramatically.

E.g. For 687-710 nm set of lines: light yield of the samples fired at 980 ℃ and 1050 ℃ increased approximately by 67% and 84% compared to the sample fired at 700 ℃. This is because higher temperature firing yields better crystallization.
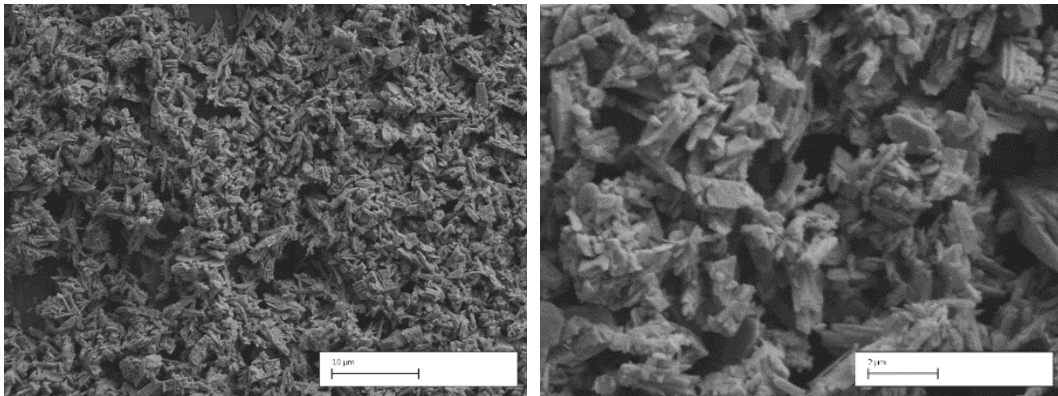
6.3.2. GdBO$_3$:Eu^{3+}

Figure 6.5 SEM images of   GdBO3:Eu3+

Fig. 6.5 presents SEM micrographs of GdBO$_3$:Eu^{3+} sample fired at 800℃. GdBO$_3$:Eu^{3+} precursors have a rod shape of 0.5 µm to 2 µm in length.

Fig. 6.6 shows the fluorescence spectrum of GdBO$_3$:Eu^{3+} samples recorded from 532-750 nm. Under the excitation of the laser beam, GdBO$_3$:Eu^{3+} displays a red colour. The synthesized phosphor samples show a red emission due to Eu^{3+}.
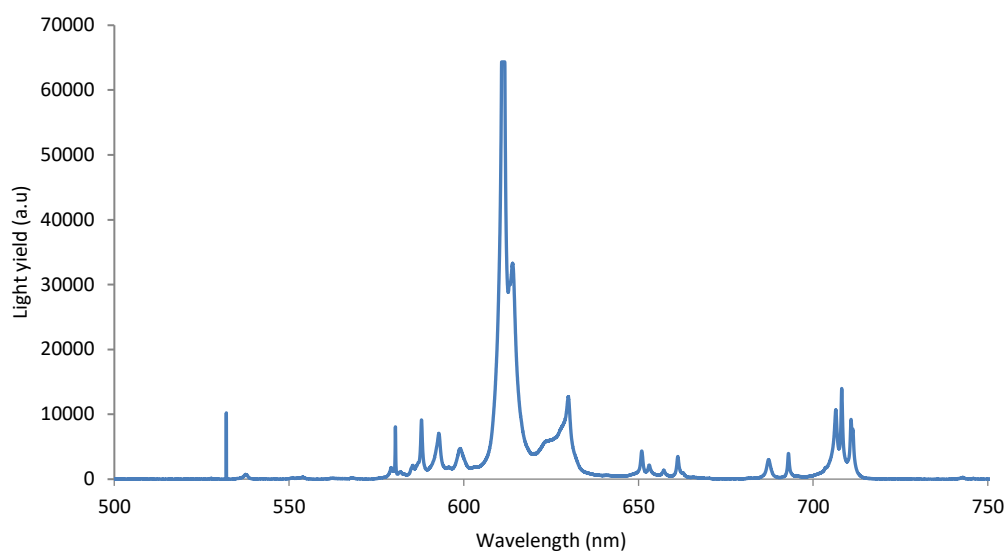
Figure 6.6 Fluorescence spectra of GdBO3:Eu³⁺ at 800 ̊C

The charged particles emitting from the reactions mentioned above consequently excite Eu^{3+} ions and result in the characteristic Eu^{3+} emission peaking at 612 nm that corresponds to the transition of electrons from 5d to 7f energy levels.
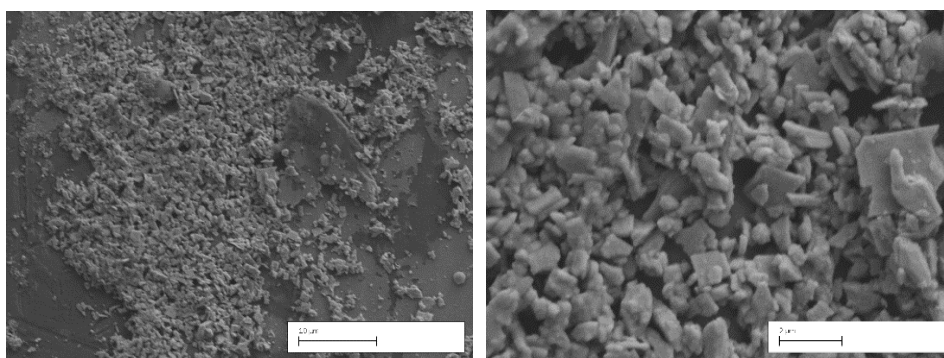
6.3.3. Li₆Gd(BO₃)₃

Figure 6.7 SEM image of Li₆Gd(BO₃)₃:Eu³⁺

Fig. 6.7 shows SEM micrographs of $Li_6Gd(BO_3)_3$:Eu^{3+} fired at 800 ̊C.
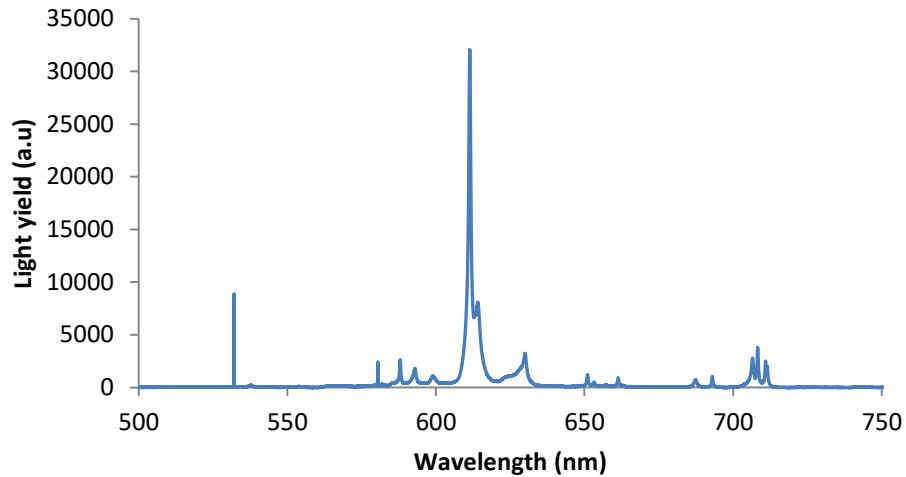
Figure 6.8 Fluorescence spectra of Li₆Gd(BO₃)₃:Eu³⁺ at 550 ̊C

Fig. 6.8 shows a fluorescence spectrum of $Li_6Gd(BO_3)_3$:Eu^{3+} samples recorded from 532-750 nm. Under the excitation of laser beam, $Li_6Gd(BO_3)_3$:Eu displays a red colour. The synthesized phosphor samples show a red emission due to Eu^{3+}.

The charged particles emitting from the reactions mentioned above consequently excite Eu^{3+} ions and result into the characteristic Eu^{3+} emission peaking at 612 nm that corresponds to the transition of electrons from 5d to 7f energy levels.

6.3.4 h-BN

SEM micrographs of h-BN with and without substrate heating during the deposition process are presented in the following three figures.
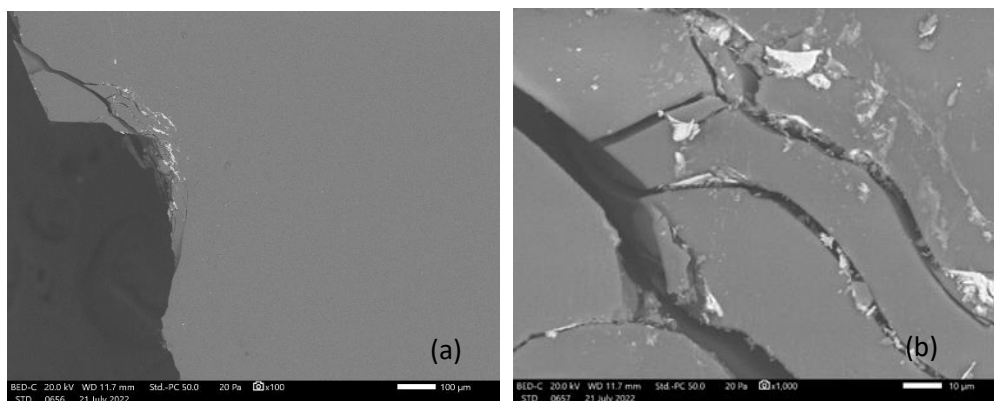

Figure 6.9 h-BN (a) film deposited at 25 ̊C (without substrate heating) (b) edge of the film

Fig. 6.9 shows that, the surface of deposited h-BN thin film is very smooth. Cracks are visible only in the edges.
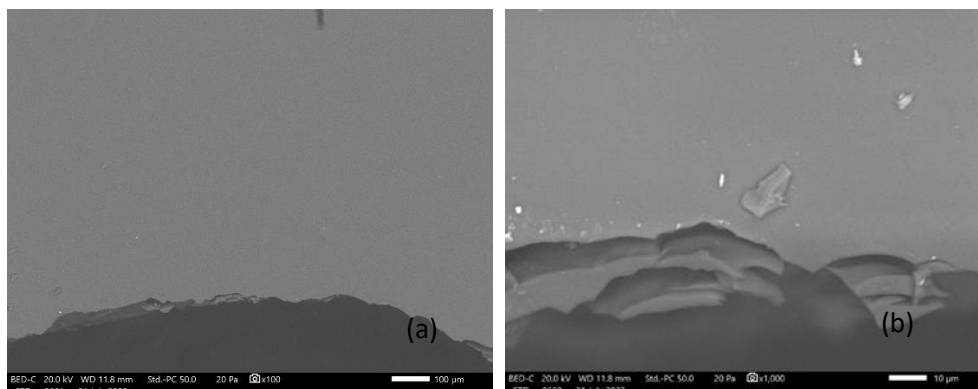

Figure 6.10 h-BN (a) film deposited with 60 ℃ substrate heating (b) edge of the film

Fig. 6.10 shows that the smoothness of the film surface is improved further with substrate heating (60 ℃) and the cracks at the edges are notably reduced, compared to the h-BN film prepared without substrate heating.
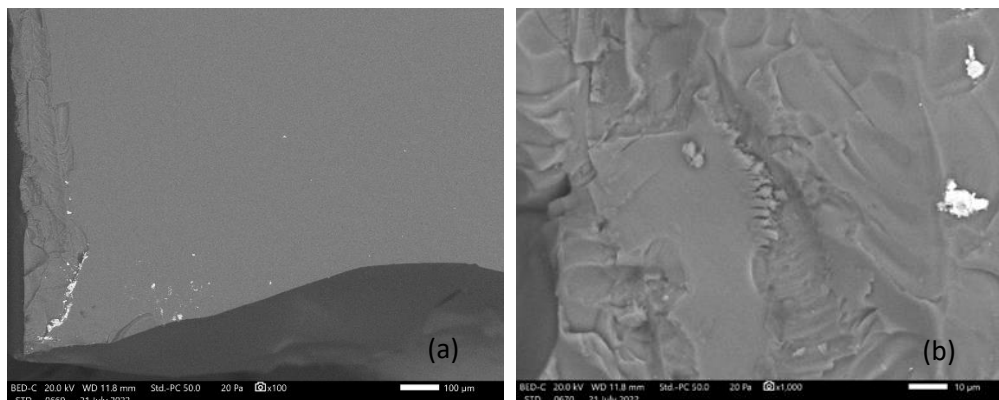
Figure 6.11 h-BN (a) film deposited with 100 ℃ substrate heating (b) edge of the film

Fig. 6.11 shows images obtained of the h-BN layer following deposition with 100°C substrate heating. The observed surface is very smooth compared to other two films, the improvement arising due to the reduction of oxygen impurities at higher temperature.

The h-BN films were also analyzed by Atomic Force Microscopy (AFM), an AFM analysis providing images with near-atomic resolution for measuring surface

topography or roughness of samples which helps in evaluating parameters like amplitude or height.

The average roughness (R_{ave}) and the root mean square roughness (R_{rms}) are the height parameters used to provide a general description of height variations, the deviation in height that represent the standard deviation of surface heights. Many peaks and valleys appeared in the AFM images which significantly affect the R_{ave} and R_{rms} values.
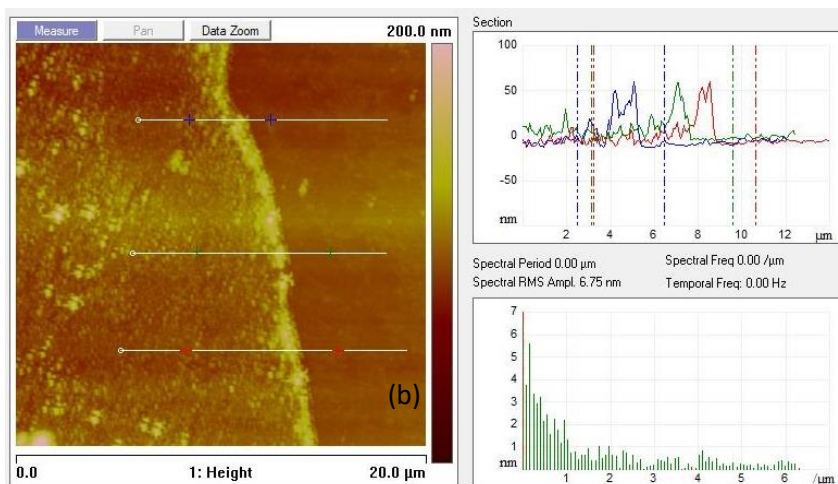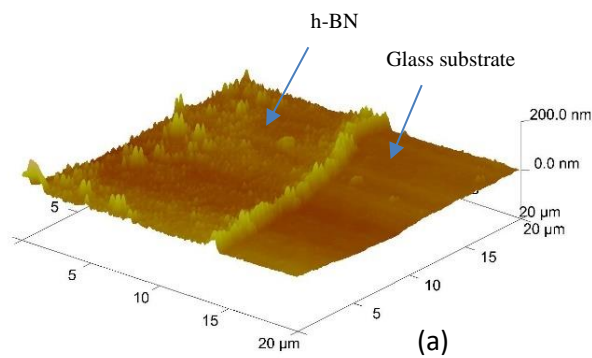
Edge measurements:

Figure 6.12 AFM analysis (a) 3-D structure (b) 2-D structure (line scans)
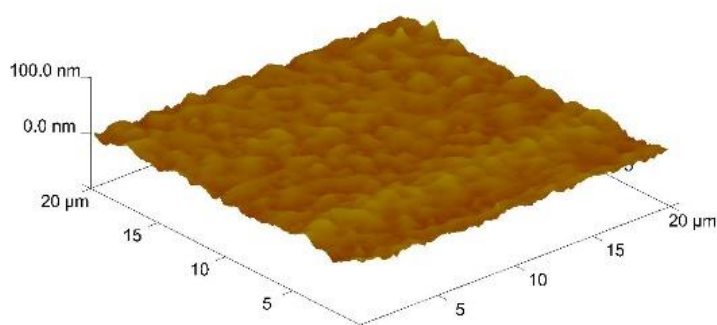
Surface measurements:

Figure 6.13 AFM Surface analysis (centre of the film)

Fig. 6.12 and Fig. 6.13 present 3-D images of the h-BN thin film deposited without substrate heating (at 25°C). The rms roughness is less than 6.748 nm for the surface areas with fewer wrinkles. The AFM line scans show that the average thickness of the deposited h-BN film was around 50 nm. It was observed that there was a large difference between the measured QCM thickness (1 µm) and the actual deposited layer thickness (50 nm).

6.4. Testing with Thermal neutrons

Gadolinium based samples were irradiated with a Deuterium-Deuterium (D-D) source emitting 2.5 MeV neutrons. To produce thermal neutrons a 15 cm thick high density polyethylene (HDPE) moderator cube was used. The neutrons passed through about 10 cm (between the HDPE and the detector) of air before hitting the samples. The experimental set up is indicated in the photograph and schematic diagram shown in Fig. 6.14. The pulse height distribution from irradiating the Gd_2O_3:Eu^{3+}, $GdBO_3$:Eu^{3+}, and $Li_6Gd(BO_3)_3$:Eu^{3+} samples with thermal neutrons was obtained using a custom designed Bridgeport SiPM MCA (model no: SIPM 1K_BC36_H50).

HDPE is a good neutron moderator containing hydrogen and carbon and is used as a moderating material for neutrons to thermalize fast neutrons.
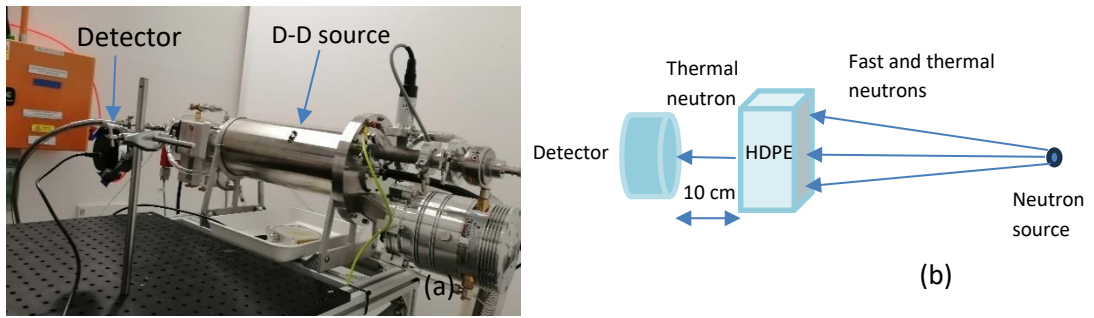
Figure 6.14.(a) Experimental setup (b) schematic of setup

6.4.1 Gd based thin scintillators

The fabricated Gd-based thin layer scintillator (100 µm) produced a pulse height spectrum with features that are attributable to Gd K X-ray emission following neutron capture as shown in the following three figures.
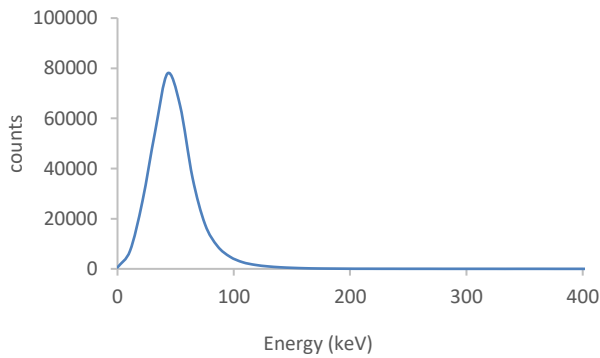
Figure 6.15 Pulse height spectrum of Gd2O3:Eu3+ (fired at 980 ℃)
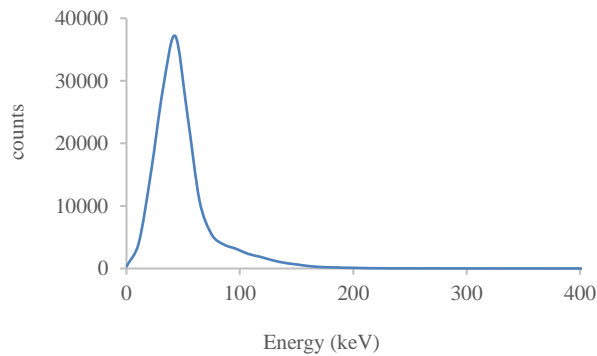
Figure 6.16 Pulse height spectrum of GdBO$_3$:Eu^{3+} (fired at 800 ℃)
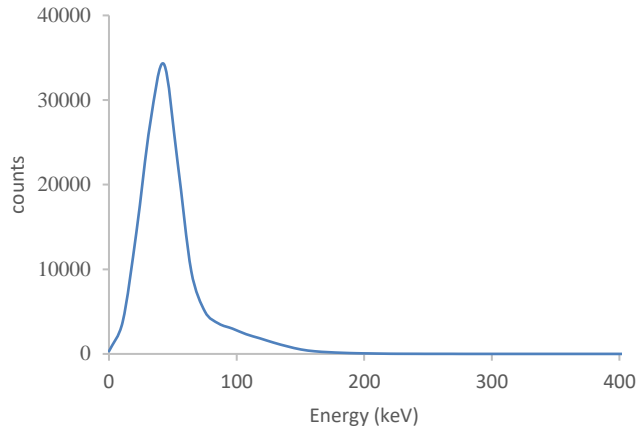
Figure 6.17 Pulse height spectrum of LGB (fired at 800 ̊C)

The emission probability of K_α X-rays per neutron capture in ^{157}Gd is 18.2±1% while the emission probability of K_α X-rays in ^{155}Gd is 29.1±3.8%. Therefore, detection of the K_α X-ray peak in the 43 keV region is more efficient.

There are two sources of gamma rays that are concerned when Gd is used as a neutron capture element. One source is that of external gamma rays accompanying the neutron field and the other is neutron activated internal prompt gamma rays. In the presented work thin film scintillators (thickness ~100 μm) were used and were virtually transparent to the high-energy gamma rays mentioned above.
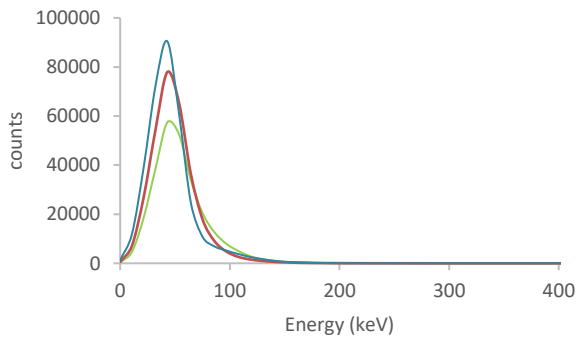
Figure 6.18 Pulse height spectra of Gd₂O₃:Eu³⁺ samples fired at 700 (green), 980 (red), and 1050 ̊C (blue)

Fig. 6.18 shows that the number of photons emitted by the $Gd_2O_3:Eu^{3+}$ scintillator layer increases when the firing temperature is increased.

This clarifies that, for samples fired at 700-1050˚C, the luminescence increased significantly because higher temperature firing yields better crystallization, thus increasing the detection efficiency of the samples.

6.4.2 h-BN based scintillator layer

The thermal neutrons used in this work were produced from an ^{241}AmBe source located within a moderating polyethylene cube. The moderator is 50 mm of polyethylene, that covers a hole in the poly shielding of 100x100 mm containing the source. The role of the moderating polyethylene is to provide moderation to the fast neutrons emitted from the Be (α, n) reaction to thermalize.

The detector sits on top of cover of source, approximately 50 cm from the source. The pulse height distribution from irradiating h-BN samples with thermal neutrons was obtained using a custom designed Bridgeport SiPM MCA (model no: SIPM 1K_BC36_H50).
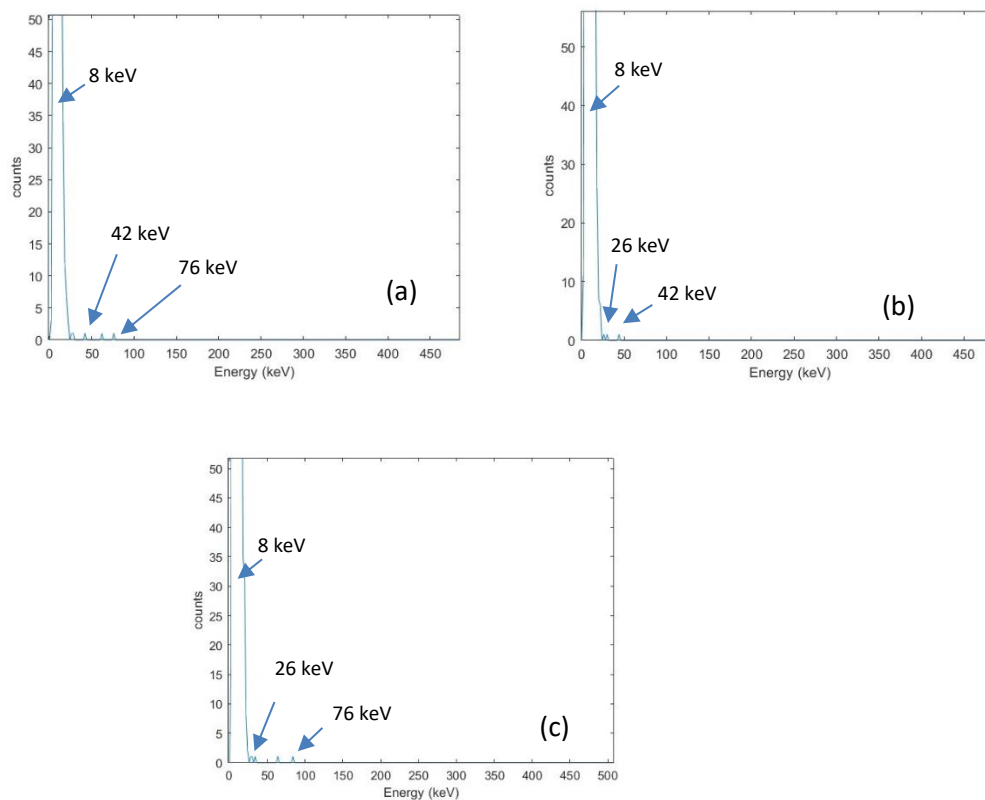
Figure 6.19 ^{241}AmBe spectrum of h-BN (a) 25˚C (b) 60˚C (c) 100˚

The fabricated h-BN scintillator thin film produced a pulse height spectrum with features at 8 keV, 26 keV, 42 keV and 76 keV.

6.5 Results and Discussion

The focus of the Gd based scintillator development was to take advantage of the high neutron capture cross section of the gadolinium isotopes present in Gd based scintillators, combined with the high attenuation coefficient for efficient detection of neutron-induced gamma rays. These combined properties mean that Gd based scintillators have the potential to offer a very clean signal for thermal neutron detection.

The gadolinium isotopes from mass 154 to 158 are stable, although only two isotopes, ^{155}Gd and ^{157}Gd, have significant thermal neutron cross sections.

The reaction products of (n, γ) reactions on ^{155}Gd and ^{157}Gd are ^{156}Gd and ^{158}Gd respectively. The reaction Q-value energies are 8.536 and 7.937 MeV. (n, γ) reactions produce a large number of high energy gamma decays, typically above 1 MeV, which are not of primary interest in this work. The resulting de-excitations also produce transitions through numerous low-lying states, which are much more likely to be stopped within a relatively small scintillator crystal. The level scheme for the first three excited states in each of the nuclides of interest is shown in Fig. 2.1. The first excited states in ^{156}Gd and ^{158}Gd are at 88.97 keV and 79.51 keV respectively, which are populated by E2 transitions of 199.22 keV and 181.95 keV from the 4^+ 2nd excited states. In turn the 2nd excited states are themselves populated by E2 transitions of 296.4 keV and 277.6 keV from the 6^+ 3rd excited states. These transitions are the source of key neutron signatures for gadolinium containing scintillators [64-65]. However, it should be noted that the 2^+ first excited states in both isotopes can also decay via internal conversion processes, and this mechanism produces an additional low energy.

The lower energy peak at ~43 keV is caused by internal conversion decays occurring within the Gd based scintillator from the first excited states. The internal conversion coefficients are both greater than 1 (3.89 and 5.94 respectively [69]) indicating de-excitation is predominantly via this mechanism. The thermal neutron captures cross sections of ^{155}Gd and ^{157}Gd are sufficiently large that the thermal neutron reaction occurs within tens of micrometres of the surface of the detector. Hence there is a high

likelihood of escape by the 43 keV gadolinium K-shell X-ray [19] for approximately half of the internal conversion events.

The size of the prepared scintillator is small (1 cm^2 and 100 μm thickness). Such thin film devices are likely to be gamma blind, because of the long attenuation length of gamma radiation, at energies of 200 keV and above where for 0.1 mm thickness layers, the photoelectron interaction probability is calculated to be < 2%) compared to the interaction probability for thermal and epithermal neutrons. However, there is the distinct possibility that X-rays, caused by inelastic scatting processes in materials placed between the source and the detector, may cause K-shell Auger electron emission. Consequently, there is a range of thicknesses where the Gd-doped film is opaque to neutrons and somewhat transparent to typical gamma rays. For the devices we have measured, the high energy gammas have a mean free path much greater than the active region and can be ignored, not only based on cross-section but because the experimental pulse height spectra are the characteristic of the expected electron energy spectrum.

We compared the response of the ^{nat}Gd based thin film scintillators developed under this research with the GAGG:Ce scintillator response under same experimental condition. Fig. 5.8 shows the obtained spectra for GAGG:Ce. Features of spectra obtained from the GAGG:Ce and ^{nat}Gd based thin films scintillators are similar to each other. This shows that ^{nat}Gd based thin film scintillators are promising for thermal neutron detection.

The focus on the development of h-BN + ZnO scintillator was to check the feasibility of its use as a thermal neutron detector. The boron (or boron containing) layer must be thick enough (tens of μm) to capture the incoming neutron flux, yet sufficiently thin (a few μm) to allow the daughter particles (α and Li) to reach into the ZnO layer to generate optical photons.

Samples were irradiated with an Americium-Beryllium (^{241}Am/Be) neutron source. Based on the dominant nuclear reaction described earlier, each absorbed neutron is expected to generate daughter particles (Li and α) with kinetic energies of 2.310 MeV (94%) and 2.792 MeV (6%), giving an average energy of 2.34 MeV.

Although the neutron absorption layer in the devices studied was only 50 nm, signal generation was evident.

Chapter 7

Study 4

Development of Front-End Electronics

7.1. Introduction

Silicon photomultipliers (SiPM) are considered as a promising device for the development of photon counting applications. This chapter is about the design, development, and performance measurements of front-end electronics for a prototype radiation detector with a SiPM. For the detection of ionizing radiation, a SiPM is coupled to a scintillating material. In this arrangement the SiPM detects the scintillation photon produced by the radiation.

The SiPM used is a solid-state single photon sensitive detector formed of an array of microcells, each consisting of single photon avalanche diode (SPAD) with its own quench resistor and a capacitively coupled fast output able to detect signals at the single photon level. SPADs are designed to operate in high inverse polarization, with a wide depletion zone that produces a pulse as an output when an incident photon triggers an avalanche. SiPMs are insensitive to magnetic fields, very small in size, and only need a bias voltage of between 20 V to 100 V, much lower than the voltage required for photomultiplier tube (PMT) operation, which makes them attractive for novel radiation detector systems.

Often, the front-end electronics plays a fundamental role in meeting the relevant specifications of a detection system and, in some cases, it even limits the system performance. In some applications classic readout designs for radiation detectors are not able to provide optimal performance due to the particular characteristics of SiPM sensors used. Thus, several impromptu readout approaches are developed to maximise the favourable features of this type of signal readout for radiation detectors. In this study, the main requirements and design considerations for a prototype scintillation

detector are discussed and an overview of the implementation of a front-end readout system is provided.

7.2. Software

The complete tool chain described here works under Windows 10/11.

7.2.1. Cadence OrCAD

The most important tool used for designing the front-end electronics was the Cadence Allegro PCB 17.4-2019 design software from OrCAD, which was used for circuit design and the PCB layout. Most of the circuits used for the front-end boards were simulated and tested with OrCAD PSpice before commissioning. Resources and documentation are available on the OrCAD website [70].

7.3. Low cost front-end electronics

This section is about the development and performance measurements of front-end electronics for the prototype detector. The section begins with the reverse-engineering, analysis, and the development and commissioning of front-end readout electronics.

7.3.1. Design Consideration

The prototype scintillation neutron detector is designed to operate in pulse mode. Once the radiation detector is operating in pulse mode, each individual pulse amplitude carries important information regarding the number of photons detected following a particular radiation interaction in the detector. Pulse height spectra are a fundamental property of a detector output routinely used to deduce information about the incident radiation or the operation of the detector itself.

When operated in pulse mode, a common situation often arises, in which the pulses from the detector are fed to a counting device with a discrimination level. Signal pulses must exceed a given level in order to be registered by the counting circuit. In setting up a nuclear counting measurement, it is often desirable to establish an operating point

which will provide maximum stability over long periods of time. One such stable operating point can be achieved at a discrimination level and small changes in the discrimination level will have minimum impact on total number of pulses recorded.

Biasing the SiPM

A MICROFC-60035-SMT-TR1, C-series low noise, 6×6 mm^2 SiPM from On-semiconductor was employed in the readout circuit design. The SiPM has three output connectors for connecting the bias voltage, the standard output from the anode and the fast output signal.

The SiPM is designed to operate in Geiger mode where the cathode must be positively biased with respect to the anode above the breakdown voltage, as shown in Fig. 7.1. The breakdown voltage of the SiPM is the minimum reverse bias voltage at which the SPAD operates in Geiger or avalanche mode. The overvoltage is the excess voltage applied above the breakdown voltage.
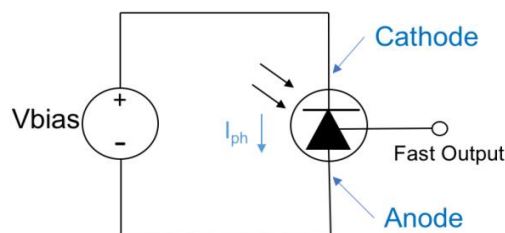
Figure 7.1 Biasing the SiPM [46]

Breakdown voltage and overvoltage range are both a function of SiPM technology and the overvoltage influences SiPM parameters such as photon detection efficiency (PDE), gain and noise. SiPM breakdown voltage is temperature dependent. The temperature coefficient of the breakdown voltage is process dependent. For accurate quantitative detection in an uncontrolled thermal environment, temperature measurement and compensation of the bias voltage may be required to maintain a consistent overvoltage and performance.

The manufacturer recommended parameter values for the chosen SiPM are as follows:

Breakdown voltage = V_b = range is 24.2 V to 24.7 V

Overvoltage = V_{ov} = range is 1 V to 5 V

Therefore, applied bias voltage should be in the range of 25.2 V to 29.7 V
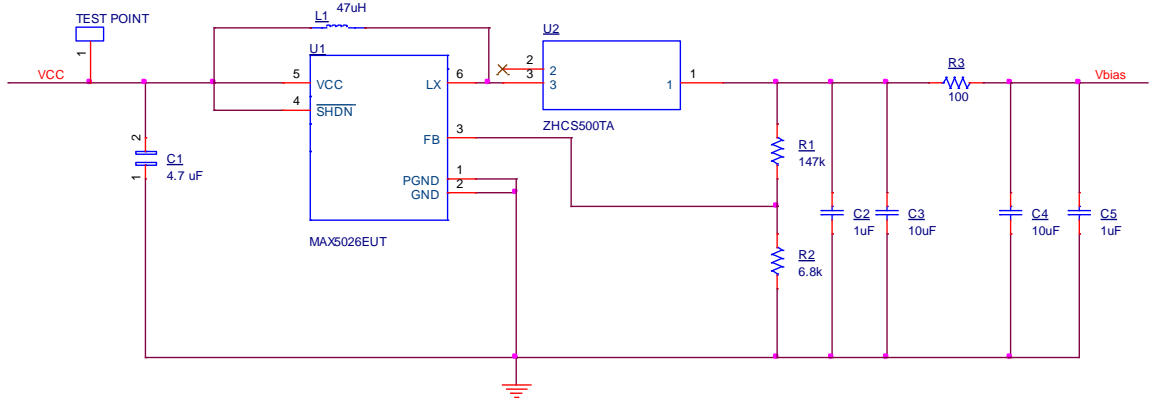
Figure 7.2 Bias voltage supply circuit

To supply bias voltage to the SiPM a constant-frequency, pulse width modulating, low-noise, high output voltage DC-DC converter MAX5026 was employed in the circuit, as shown in Fig. 7.2. The output voltage of the MAX5026 can be fixed by setting two external resistors, R1 and R2. First the value of R2 is selected in the 5 kΩ to 50 kΩ range according to the datasheet recommendation, with R1 then given by the following equation stated on the datasheet of the MAX5026:

$$R1 = R2 \left(\frac{Vout}{Vref} - 1\right) \tag{7.1}$$

Where, V_{ref} = 1.25 V.

In the circuit design, 6.8 kΩ and 147 kΩ values were used for R2 and R1 respectively, based on an expected output of +28.2 V for biasing the SiPM.

The output filter capacitor should be 1 µF or greater to achieve low output ripple. For very low output ripple applications, the output of the boost converter can be followed by an RC filter to further reduce the ripple. Fig. 7.2 shows that a 100 Ω, 1 µF RC filter was used in the presented circuit design to reduce noise at the output.

Basic SiPM readout and output polarity

When biased in Geiger mode, the SiPM produces a photocurrent proportional to the number of microcells that have fired, which provides a measure of the amount of light detected by the sensor. The photocurrent (I_{ph}) flows through the sensor from cathode to anode, as shown in Fig. 7.1, and either of these terminals can be used as standard output.

The standard output polarity depends on whether the anode or the cathode is being used for readout and does not depend on the sensor type. Reading out from the cathode will give a negative polarity and reading out from the anode will produce positive polarity (see Fig. 7.3).
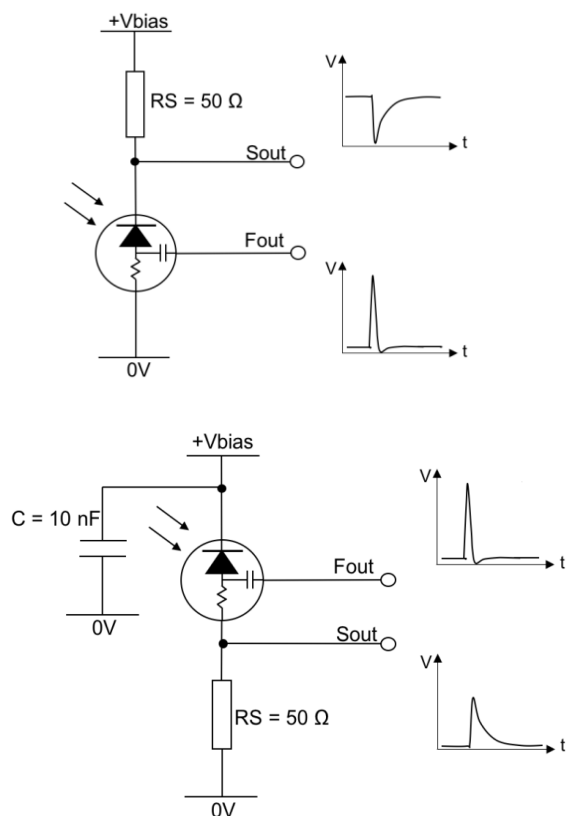

Figure 7.3 Biasing the readout for best fast output [46]

To obtain the positive output polarity, the biasing a readout circuit was designed as shown in Fig. 7.4.
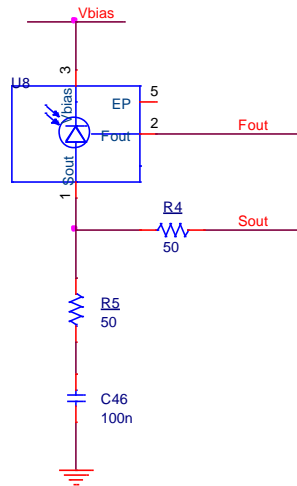
Figure 7.4 Biasing and readout circuit

The fast output is a capacitively coupled output derived from the fast-switching pulse that occurs within the microcell. Unlike the standard output there is no net charge transfer across the fast output. The fast output amplitude is proportional to the number of microcells that have fired and can therefore provide information on the number of photons detected. If the fast output is not used it should be left floating without any cables or wires attached.

7.3.2 Standard output readout

To readout the SiPM from the standard output, the photocurrent generated on detection of photons needs to be converted to a voltage or several amplification stages are needed before further signal processing or analysis is possible.

However, the capability to operate the SiPM contemporarily in photon counting is dependent on the design of the front-end electronics. So, it is important to find the right balance and a feasible solution for managing the SiPM for it to work efficiently in photon counting mode and during charge integration mode.

7.3.3. Power supply

The front-end readout is designed to operate in either battery mode (9 V) or USB mode (5 V) as shown in Fig. 6.5.
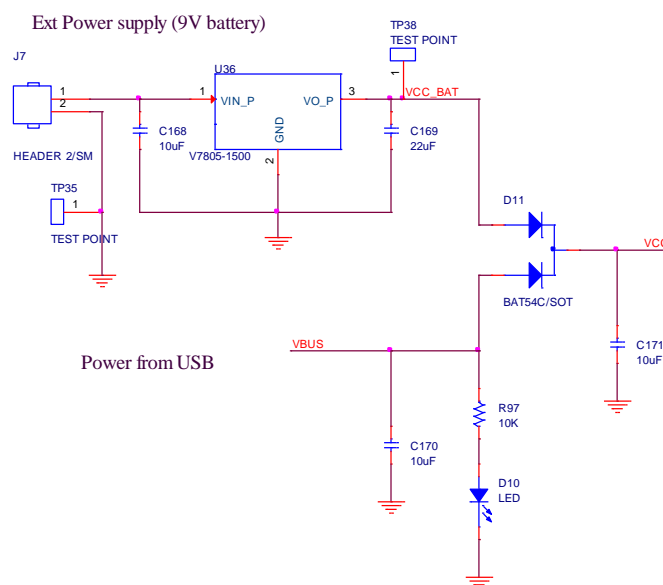
Figure 7.5 Power supply selection

To supply the power required for the functioning of the front-end readout circuit several TPS76801QPWP low-dropout (LDO) low-power linear voltage regulators were used. The TPS768xx features high power supply rejection ratio (PSRR), ultralow noise, fast start-up, and excellent line and load transient responses in a small space outline and is stable with 10 µF capacitors.

Since the dropout voltage is very low and directly proportional to the output current, and the quiescent current is very low and independent of output loading, LDOs yield a significant improvement in operating life when the prototype circuit is battery-powered. The chosen LDO also features a shutdown mode, applying a TTL high signal to EN (enable) shutting down the regulator, reducing the quiescent current to less than 1 µA at $T_J = 25°C$. Power good (PG) is an active high output, which can be used to implement a power-ON reset or a low-battery indicator.
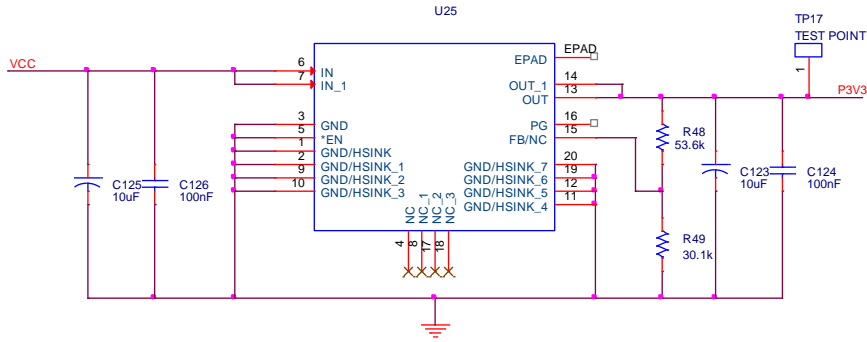
Figure 7.6 LDO schematic

The output voltage of the TPS786xx adjustable regulator is programmed using an external resistor divider as shown in Fig. 7.6. The output voltage is calculated as follows:.

$$V_o = V_{ref} \left(1 + \frac{R1}{R2}\right) \qquad (7.2)$$

Where, V_{ref} = 1.2246 V (the internal reference voltage).

7.3.4 USB connection

Designing universal serial bus (USB) communications into the circuit enables the system to communicate with a variety of USB host devices and provides a convenient power option through the USB connection. Having both power and data communication capability in one cable adds convenience and flexibility to the design. A FTDI IC was used to implement the USB functionality.

The USB connection can be operated in two different modes: host or device, with a hub being a special version of a USB device. A supplement to the USB standard introduces 'On-The-Go' mode, which enables a USB product to operate as either a host or a device depending on which kind of controller is at the other end of the cable.

USB Host

The USB host controls data flow on the bus by sequentially polling all devices for data, meaning that no device can transmit on the bus without a host request. A USB host must be able to supply power to a connected USB device through the +5 V VBUS line.

USB Device

USB devices are bus slaves that provide functionality to the USB host. Devices must provide configuration information to the host so that the host can configure the connection. Devices are separated in different classes depending on their functionality. Two different types of device classes exist: hubs and functions. Hubs provide a host with more attachment points, while functions provide additional functionality. USB devices will transmit data or control information over the bus when requested by the host.

As a USB host provides +5 V over the V_{BUS} line, a USB device can either be powered over the USB cable, or it can be self-powered. The following sections present schematics for how to connect USB as data transfer and a power (+5 V) supply option when battery power is disconnected.

In the schematic design shown in Fig.7.7 a FT2232H, a 5th generation FTDI USB device was used. The FT2232H is a USB 2.0 high speed (480 Mb/s) to UART/FIFO IC and has the capability of being configured in a variety of industry standard serial or parallel interfaces.
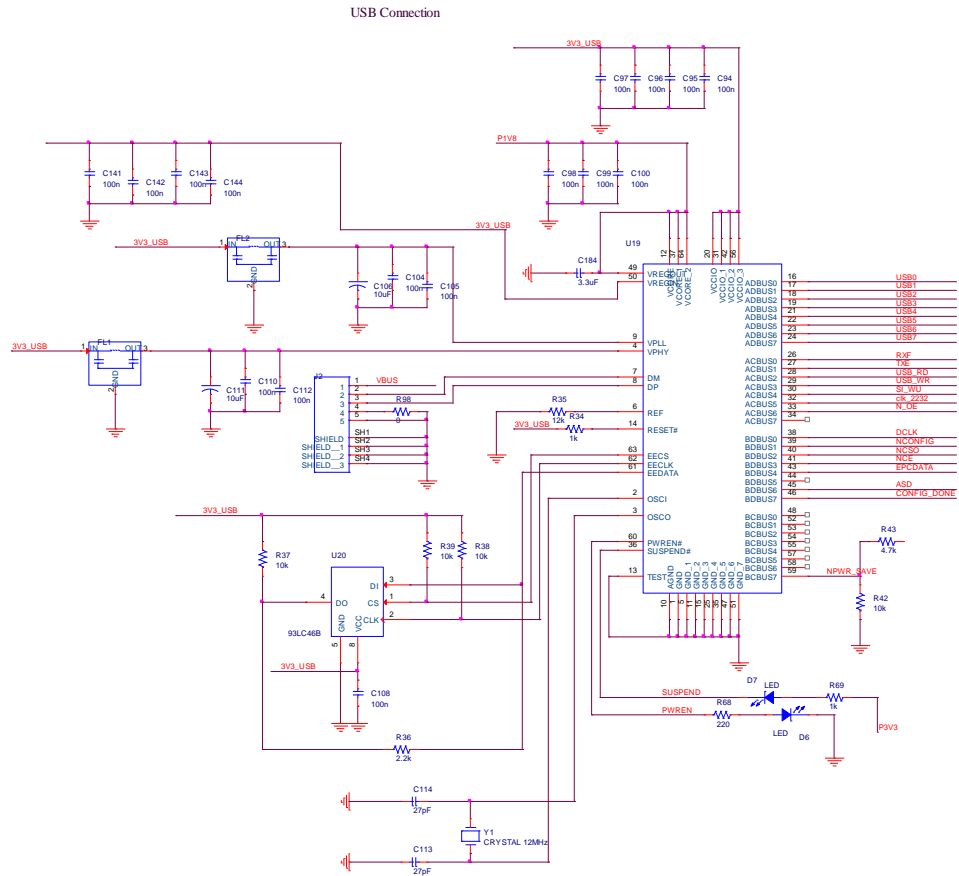
Figure 7.7 USB connection schematic

7.4. PCB Fabrication

The power supply design and SiPM circuit with bias voltage supply was fabricated as a 6-layer PCB and a 2-layer PCB, as shown in the photographs of Fig. 7.8.

The SiPM bias circuit (Fig. 7.8 (a)) utilizes a MAX5026 voltage converter. The MAX5026 is a constant frequency, pulse width modulating, current mode step-up voltage converter with an internal power switch that operates at 500 kHz. By employing a MAX5026, the voltage output can be increased up to +30 V from the +3 V to +11 V input source. In the presented design a 5 V input voltage was used to get the required bias voltage of ∼28 V. This circuit is specially designed for low noise performance by employing 1 μF and 10 μF capacitors for C2, C5 and C3, C4 respectively, as indicated in Fig. 7.2.

Figure 7.8 Fabricated front-end circuit (a) SiPM with bias voltage supply (b) power supply with programming facility

7.5. Performance Measurements

An ideal photon-detector generates signals with identical shapes linearly scaled with the number photons which have initiated Geiger discharges, and the charge spectrum will comprise of 0, 1, 2, 3. . . p.e. However, SiPMs do show a number of differences from an ideal detector, frequently called 'nuisance parameters', including:
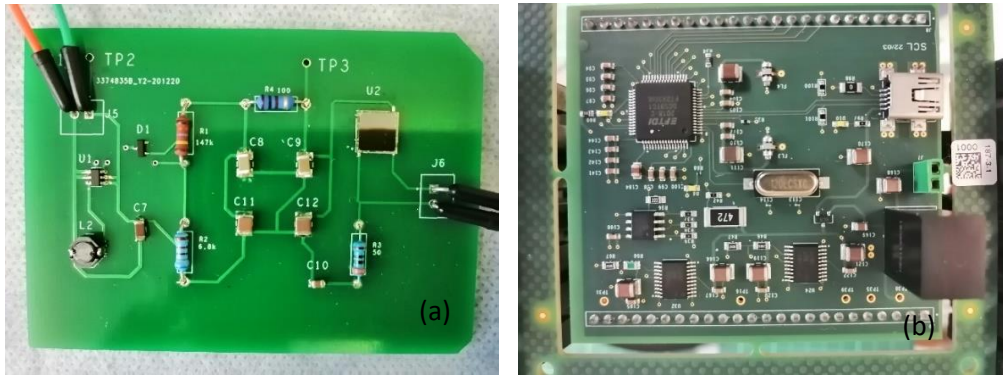
1. Dark counts produce background signals at the primary dark count rate.
2. Secondary photons generated during Geiger discharges can create an electron-hole pair in an adjacent pixel and cause a Geiger discharge there, resulting a double-size signal known as crosstalk.
3. Secondary photons produced from Geiger discharges can create an electron-hole pair in the non-depleted silicon of the detector and charge carriers can diffuse into the amplification region of a neighbouring pixel, where they cause a Geiger discharge known as delayed crosstalk.
4. During the Geiger discharge, charge carriers can be trapped in defect states and released after some time producing a Geiger discharge in the same pixel as the primary discharge known as after-pulsing. The signal strength of after-pulses depends on the recovery rate of the pixel. Additionally, secondary photons generating electron-hole pairs in the non-depleted Si with charge carriers diffusing into the same pixel as the primary Geiger discharge, contribute to after-pulses called optically induced after-pulsing [71].

Furthermore, pixel-to-pixel gain variations and read-out noise will result in signal fluctuations. The effects discussed above can also be observed in the oscilloscope images shown in Fig. 7.9.

Output pulses were measured using a Tektronix TDS2014 four channel digital storage oscilloscope, the SiPM being shielded from external light for all the measurements.
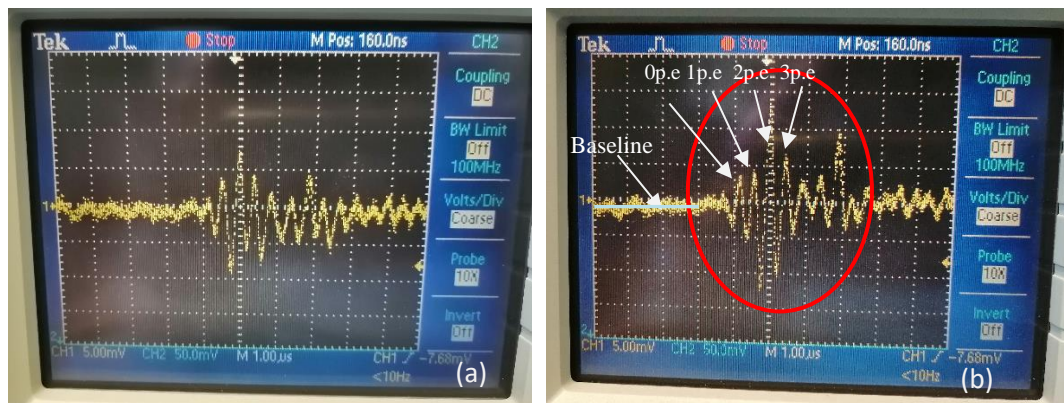
Figure 7.9 SiPM output pulses (Oscilloscope measurements)

The vertical scale was set to 5 mV and the horizontal scale to 1 µs per division using channel 1 of the oscilloscope. When the front-end circuit was exposed to a radiation source, pulses with heights varying from one pulse to another were observed, their distribution being shown in the images of Fig 7.9. The amplitudes of the output pulses were measured with the oscilloscope, the first peak corresponding to no detection, the second peak corresponding to one detection, the third to two simultaneous detections, and so on. The images in Fig. 7.9 show that it is possible to distinguish the different pulse heights corresponding to the different numbers of simultaneous detections.
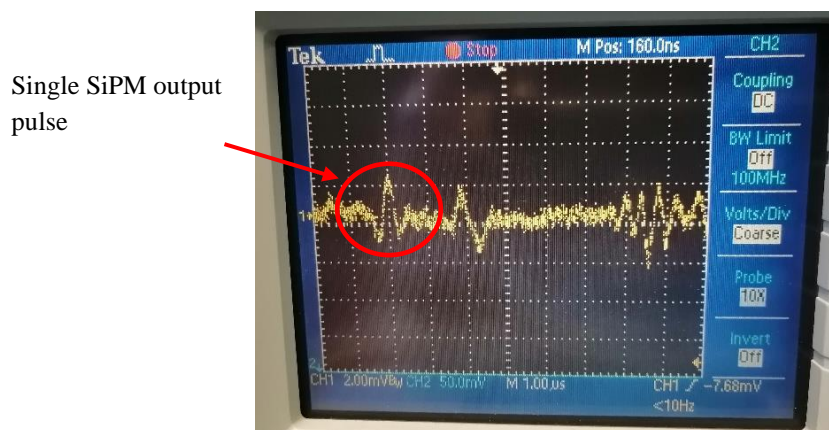
Figure 7.10. Response signal of the SiPM as seen on the oscilloscope.

97

Changing the vertical scale to 2 mV per division and the horizontal scale to 1 µs per division the image in Fig. 7.10 was obtained that indicates the pulse height of the measured signal pulse is 4 ± 0.2 mV.

7.6. Discussion

This chapter has presented the design and evaluation of front-end electronics for a SiPM based radiation detector. The presented measurement results demonstrate that the voltage output of the implemented circuit has features that are attributable to the successful detection of photons.

Key features of the prototype system presented include ensuring that the power consumption is low and that the size of the front-end electronics PCBs are as small as possible to keep the weight of the system as low as possible for its intended application in a portable handheld neutron detector.

Chapter 8

Results and Discussion

An ideal scintillator would have high luminosity, high density and effective atomic number, fast rise and decay time constants, a peak emission wavelength that matches well with the spectral sensitivity of the photodetector and low non-proportionality. In addition, the scintillation material should be inexpensive to manufacture, non-hygroscopic, rugged, and preferably produce no intrinsic radiation. All these properties are yet to be found in a single material with a simple and cost-effective growth technique. Since the appropriate procedures to obtain such materials are still being developed, scintillator properties are usually compromised for a specific radiation detector application.

Thus, an intense research and development continues to explore new phosphor materials as scintillators or the optimization of the current ones taking advantage of new technological methods for their preparation. Therefore, development of phosphors with a rare earth element such as gadolinium show high potential for deployment as efficient and cost-effective inorganic scintillators for neutron detection. The presented work has discussed the development and characterization of Gd_2O_3:Eu^{3+}, $GdBO_3$:Eu^{3+}, $Li_6Gd(BO_3)_3$:Eu^{3+} and h-BN scintillators for thermal neutron detection.

The focus on the Gd based scintillator development is to take advantage of the high neutron-capture cross section of the gadolinium isotopes present in Gd based scintillators.

Natural gadolinium (^{nat}Gd) comprises the 7 natural isotopes, out of all, ^{155}Gd and ^{157}Gd shows the highest thermal cross section for ^{nat}Gd. The products of reaction are two stable isotopes, $^{156}Gd^*$ and $^{158}Gd^*$ in excited state, 8.536 MeV and 7.937 MeV respectively. These reactions produce a large number of high energy gamma decays, typically above 1 MeV, which are not of primary interest in this work. The resulting de-excitations also produce transitions through numerous low-lying states, which are much more likely to be stopped within a relatively small scintillator crystal. The first excited states in ^{156}Gd and ^{158}Gd are at 88.97 keV and 79.51 keV respectively, which are populated by E2 transitions of 199.22 keV and 181.95 keV from the 4^+ 2nd excited

states. In turn the 2nd excited states are themselves populated by E2 transitions of 296.4 keV and 277.6 keV from the 6^+ 3rd excited states. These gamma transitions are the source of key neutron signatures for gadolinium containing scintillators. However, it should be noted that the 2^+ first excited states in both isotopes can also decay via internal conversion processes, and this mechanism produces an additional low energy neutron-related peak due to the escape of characteristic gadolinium K-shell X-rays.

The lower energy peak at ~43 keV is caused by internal conversion decays occurring within the Gd based scintillator from the first excited states. The internal conversion coefficients are 3.89 and 5.94 respectively, indicating de-excitation is predominantly via this mechanism. The thermal neutron captures cross sections of ^{155}Gd and ^{157}Gd are sufficiently large that the thermal neutron reaction occurs within tens of micrometres of the surface of the detector. Hence there is a high likelihood of escape by the 43 keV gadolinium K-shell X-ray for approximately half of the internal conversion events that only travel a few micrometres in the scintillator.

Scintillator samples were irradiated with a D-D source and peak around 43 keV was visible in the resulting spectra. Although gamma rays are emitted with high probability, most of the capture gamma rays escape without depositing any energy in the scintillator due to the small sample sizes used (1 cm^2 and 100 µm thickness).

The focus on the development of h-BN + ZnO scintillator was to check the feasibility of its use as a thermal neutron detector. The boron (or boron containing) layer must be thick enough (tens of µm) to capture the incoming neutron flux, yet sufficiently thin (a few µm) to allow the daughter particles (α and Li) to reach into the ZnO layer to generate light photons.

h-BN samples were irradiated with an Americium-Beryllium (^{241}Am/Be) neutron source. Based on the dominant nuclear reaction, each absorbed neutron is expected to generate daughter particles (Li and α) with kinetic energies of 2.310 MeV (94%) and 2.792 MeV (6%), giving an average energy of 2.34 MeV. While a 480 keV gamma ray is emitted with 94 % probability, most of the captured gamma rays escape without depositing any energy in the scintillator due to the small sample size (1 cm^2 and 50 nm thickness). Experimental results showed that, although, the neutron absorption layer in the devices developed for this study was only 50 nm, signal generation was evident.

The problem with depositing a 1 µm layer of h-BN was the time taken to do so. To obtain a 20 nm later, sputter deposition for 4 hrs was required. If substrate heating is used, a warm up time of 30 min or more is required and to cool down nearly 3 hrs is needed to bring the deposition system back to room temperature, the system used having no active substrate cooling. These limitations mean that to deposit around 20 nm to 25 nm layer thickness a full day is needed. If wanting to develop layers thicker than 1 µm, it will be better to use an alternative deposition method in the future.

Simulations have been carried out using FLUKA to predict the response of the detector. This study showed that the FLUKA code also can be used to determine the response function of scintillators and can therefore be of benefit in terms of reducing the financial cost and time taken in the development of new scintillators and radiation sensors.

For the front-end electronics development, a readout circuit which can powered through the USB connection (PC) or a rechargeable battery (9 V) was designed and tested. The presented measurement results demonstrate that the implemented circuit has features that are attributable to successful photon detection. Here the design focus was on reduction of the power consumption and PCB size, the intended application of the system being for use as a portable handheld neutron detector.

Conclusions and future work possible

The development of phosphors containing a rare earth element such as gadolinium show a high potential for deployment as efficient and cost-effective inorganic scintillators for neutron detection.

Preliminary measurements have been performed using such scintillators with SiPMs of 6×6 mm^2 area and a cell size of 35 µm and the work could be taken further through implementation with other SiPM arrays.

The front-end electronics can also be developed further by the addition of a suitable FPGA and ASIC to fulfil the goal of developing a complete prototype of a light-weight, low-cost, handheld neutron detector.

References

[1] E.V. Ryabeva, V.V. Kadilin, V.A. Idalov, Use of neutron scintillation detectors as a substitute for helium-3 counters in radiation monitors, At. Energy 127 (2019) 51-55.

[2] R.T. Kouzes, K.E. Conlin, J.H. Ely, L.E. Erikson, W.J. Kernan, A.T. Lintereur, E.R. Siciliano, D.L. Stephens, D.C. Stromswold, R.M. Van Ginhoven, M.L. Woodring, Alternatives to 3He for neutron detection for homeland security, Nucl. Instrum. Methods Phys. Res. A 623 (2010) 1035-1045.

[3] D.A. Shea, D. Morgan, The Helium-3 Shortage: Supply, Demand, and Options for Congress, CRS Report for Congress, 2010, www.crs.gov. (last accessed on 01.05.2022).

[4] P. Peerani, A. Tomanin, S. Pozzi, J.Dolan, E. Miller, M. Flaska, M. Battaglieri, R. De Silva, L. Ficini, G. Ottonello, G. Ricco, G. Dermody, C. Glies, Testing on novel neutron detectors as alternative to 3He for security applications, Nucl. Instrum. Methods Phys. Res. A 690 (2012) 110-120.

[5] A. Stoykov, J.B. Mosset, U. Greuter, M. Hildebrandt, N. Schlumpf, A SiPM-based ZnS:6LiF scintillation neutron detector, Nucl. Instrum. Methods Phys. Res. A 787 (2015) 361-366.

[6] K. Nakamura and P. D. Group, Review of particle physics, Journal of Physics G: Nuclear and Particle Physics, 37 (2010) 075021.

[7] C.W.E. van Eijk, Inorganic scintillators for thermal neutron detection, Radiation Measurements, 38 (2004) 337-342.

[8] D. S. McGregor, H. K. Gersch, J. D. Sanders, Thin film coated detectors for neutron detection, (2001).

[9] R. D. Breukers, C. M. Bartle, A. Edgar, Transparent lithium loaded plastic scintillators for thermal neutron detection, Nucl. Instrum. Methods Phys. Res. A 701 (2013) 58-61.

[10] B. J. Connors, C. J. Summers, B. Klein, E. A. Burgett, ad N. E. Hertel, ZnO Thermal Neutron Scintillators Designed for High Sensitivity and Gamma-Ray Discrimination, IEEE Nuclear Science Symposium, (2011).

[11] R.T. Kouzes, K.E. Conlin, J.H. Ely, L.E. Erikson, W.J. Kernan, A.T. Lintereur, E.R. Siciliano, D.L. Stephens, D.C. Stromswold, R.M. Van Ginhoven, M.L. Woodring,

Alternatives to 3He for neutron detection for homeland security, Nucl. Instrum. Methods Phys. Res. A 623 (2010) 1035-1045.

[12] Z. Wang and C. Morris, Multi-layer boron thin-film detectors for neutrons, Nucl. Instrum. Methods Phys. Res. A 652 (2011) 323-325.

[13] ANSI, N42.35-2006 (2006) https://webstore.ansi.org/ (last accessed on 01.11.2022)

[14] IEC 62244, Radiation protection instrumentation-installed radiation monitors for the detection of radioactive and special nuclear materials at national borders (2006) https://www.iec.ch/homepage/ (last accessed on 01.11.2022)

[15] R. L. Schulte, F. Swanson, and M. Kesselman, The use of large area silicon sensors for thermal neutron detection, Nucl. Instrum. Methods Phys. Res. A 353 (1994) 123-127.

[16] J. Haruna, J. H. Kaneko, M. Higuchi, S. Kawamura, S. Saeki, Y. Yagi, H. H. Ishibashi, F. Fujita, A. Homma, M. Furusaka and Y. Kiyanagi, Response function measurement of $Gd_2Si_2O_7$ scintillator for neutrons, IEEE Nuclear Science Symposium Conference Record 2 (2007) 1421-1425.

[17] R. Engels, G. Kemmerling and J. Schelten, Boron Nitride, A neutron scintillator with Deficiencies, IEEE Nuclear Science Symposium Conference Record 3 (2005) 1318-1322.

[18] D. S. McGregor, R. T. Klann, H. K. Gersch, and Y-H. Yang, Thin-film-coated bulk GaAs detectors for thermal and fast neutron measurements, Nucl. Instrum. Methods Phys. Res. A 466 (2001) 126-141.

[19] D. D. Schultz, B. Blasy, J.C. Santana, C. Young, J.C. Petrosky, J.W. McClory, D. LaGraffe, J.I. Brand, J. Tang, W. Wang, N. Schemm, S. Balkir, M. Bauer, I. Ketsman, R.W. Fairchild, Y.B. Losovyj, P.A. Dowben, The K-shell auger electron spectrum of gadolinium obtained using neutron capture in a solid-state device, J. Phys. D: Appl. Phys. 43 (2010) 075502.

[20] A. Gorin, K. Kuroda, I. Manuilov, K. Morimoto, T. Oku, A. Ryazantsev, H. M. Shimizu, J. Suzuki, F. Tokanai, Development of scintillation imagine device for neutrons, Nucl. Instrum. Methods Phys. Res. A 479 (2002) 456-460.

[21] R.D. Breukers, C.M. Bartle, A. Edgar, Transparent lithium loaded plastic scintillators for thermal neutron detection, Nucl. Instrum. Methods Phys. Res. A 701 (2013) 58-61.

[22] C. Piemonte, et al., Performance of NUV-HD Silicon Photomultiplier Technology, IEEE Transactions on Electron Devices, 63 (2016) 1111-1116.

[23] A. Stoykov, J. B. Mosset, U.Greuter, M. Hildebrandt, N. Schlumpf, A SiPM-based ZnS:6LiF scintillation neutron detector, Nucl. Instr. And meth., A 787 (2015) 361-366.

[24] F. Acerbi, et al., IEEE J. Quantum Electron 54 (2018).

[25] K. Nakamura and P. D. Group, Review of particle physics, Journal of Physics G: Nuclear and Particle Physics, 37 (2010) 075021.

[26] A. T. Yue, M. S. Dewey, D. M. Gilliam, G. L. Greene, A. B. Laptev, J. S. Nico, W. M., Improved determination of the neutron lifetime, Phys. Rev.Lett., 111 (2013) 222501.

[27] Heilbronn L., Neutron properties and definitions (supplement) (2015) https://three.jsc.nasa.gov/articles/ (last accessed on 20.05.2022)

[28] G. F. Knoll, Radiation Detection and Measurement. John Wiley and Sons, Inc., third edition ed, (2000).

[29] E. A. Lorch, "Neutron Spectra of 214Am/B, 241Am/Be, 241Am/F, 242Cm/Be, 238Pu/13C and 252Cf isotopic neutron sources," The International Journal of Applied Radiation and Isotopes, 4 (1973) 585-591.

[30] W. Leo, Techniques for Nuclear and Particle Physics Experiments: A How-to Approach. Springer, (1994).

[31] F. Piscitelli, Boron-10 layers, Neutron Reflectometry and Thermal Neutron Gaseous Detectors. PhD thesis, Institut Laue-Langevin and University of Perugia, (2014) 1406.

[32] C. Leroy and Rancoita, Principles of Radiation Interaction in Matter and Detection - 2nd Edition. World Scientific, Singapore, (2009). ISBN-13 978-981-281-827-0.

[33] W. Blum, W. Riegler, and L. Rolandi, Particle Detection with Drift Chambers. Springer Verlag Berlin Heidelberg, (2008) 10.1007/978-3-540-76684-1. http://www.springer.com/us/book/9783540766841/ (last accessed on 20.05.2022)

[34] J. L. Grafe, F. E. McNeill, D. R. Chettle, S. H. Byun, Characteristic X-ray emission in gadolinium following neutron capture as an improved method of in vivo measurements: A comparison between feasibility experiment and Monte Carlo simulation, Nucl. Instrum. Methods Phys. Res. B 281 (2012) 21-25.

[35] F. Sauli, "Principles of operation of multiwire proportional and drift chambers," CERN 77-09 (1977).

[36] https://www.nuclear-power.com/nuclear-engineering/radiation-detection/gaseous-ionization-detector/ (last accessed on 25.05.2022)

[37] C. Leroy and Rancoita, Principles of Radiation Interaction in Matter and Detection - 2nd Edition. World Scientific, Singapore, (2009). ISBN-13 978-981-281-827-0.

[38] Delaney, C. F. G. and Finch, E. C, Radiation detectors: physical principles and applications. Oxford: Clarendon Press ; New York : Oxford University Press , 1992.

[39] H Spieler, Semiconductor Detector Systems. Oxford University Press, 2005.

[40] S. Sze and K. K. Ng, Physics of Semiconductor Devices. JohnWiley and Sons, Inc. Wiley, third ed., 2007.

[41] G. Lutz, Semiconductor Radiation Detectors. Springer Berlin Heidelberg, 2007.

[42] D. Renker, Geiger-mode avalanche photodiodes, history, properties and problems, Nucl. Instrum. Meth. A 567 (2006) 48-56.

[43] F. Zappa et al., Principles and features of single-photon avalanche diode arrays, Sens. Actuators A 140 (2007) 103-112.

[44] V. Golovin, Patent no. RU 2142175, 1998.

[45] Z. Sadygov, Patent no. RU 2102820, 1998.

[46] http://www.onsemi.com/ (last accessed on 01.05.022)

[47] W. Kindt, Geiger Mode Avalanche Photodiode Arrays. PhD thesis, Technische Universiteit Delft, 1999.

[48] A. Lacaita et al., On the bremsstrahlung origin of hot-carrier-induced photons in silicon devices, IEEE Trans. Electron Devices, 40 (1993) 577-582.

[49] W. Shockley and W. T. Read, Statistics of the Recombinations of Holes and Electrons, Phys. Rev. 87 (1952) 835-842.

[50] F. Acerbi et al., Characterization of Single-Photon Time Resolution: From Single SPAD to Silicon Photomultiplier, IEEE Trans. on Nuclear Science, 61 (2014) 2678-2686.

[51] https://fluka.cern/ (last accessed on 01.08.022)

[52] C. Ahdida, D. Bozzato, D. Calzolari, F. Cerutti, N. Charitonidis, A. Cimmino, A. Coronetti, G. L. D'Alessandro, A. Donadon Servelle, L. S. Esposito, R. Froeschl, R.

García Alía, A. Gerbershagen, S. Gilardoni, D. Horváth, G. Hugo, A. Infantino, V. Kouskoura, A. Lechner, B. Lefebvre, G. Lerner, M. Magistris, A. Manousos, G. Moryc, F. Ogallar Ruiz, F. Pozzi, D. Prelipcean, S. Roesler, R. Rossi, M. Sabaté Gilarte, F. Salvat Pujol, P. Schoofs,V. Stránský, C. Theis, A. Tsinganis, R. Versaci, V. Vlachoudis, A. Waets, M. Widorski, New Capabilities of the FLUKA Multi-Purpose Code, Frontiers in Physics 9 (2022) 788253.

[53] G. Battistoni, T. Boehlen, F. Cerutti, P.W. Chin, L.S. Esposito, A. Fassò, A. Ferrari, A. Lechner, A. Empl, A. Mairani, A. Mereghetti,P. Garcia Ortega, J. Ranft, S. Roesler, P.R. Sala, V. Vlachoudis, G. Smirnov, Overview of the FLUKA code, Annals of Nuclear Energy 82 (2015) 10-18.

[54] N. Demir, Z. Nur Kuluozturk, Determination of energy resolution for a NaI(Tl) detector modelled with FLUKA code, Nuclear Engineering and Technology 53 (2021) 3759-3768.

[55] G. F. Knoll, Radiation detection and measurement. John Wiley and Sons, 1979.

[56] M. Moszynski, M. Balcerzyk, M. Kapusta, D. Wolski, C.L. Melcher, Large size LSO:Ce and YSO:Ce scintillators for 50 MeV range ɣ-ray detector, IEEE Transaction on nuclear science, 47 (2000).

[57] Y. Zhu, Z. Wang et al., Study of Characteristics of Ce-doped $Gd_3Al_2Ga_3O_{12}$ Scintillator, IEEE, (2019).

[58] Jung Yeol Yeom et al., First Performance Results of Ce:GAGG Scintillation Crystals With Silicon Photomultipliers, IEEE Transaction on nuclear science, 60 (2013).

[59] I. Mouhti, A. Elanique, M. Y. Messous, A. Benahmed, J. E. McFee, Y. Elgoub, P. Griffith, Characterization of CsI (Tl) and LYSO scintillator detectors by measurements and Monte Carlo simulations, Applied Radiation, and Isotopes (2019) 108878.

[60] C. Wanarak, A. Phunpueok, W. Chewpraditkul, Scintillation response of $Lu_{1.95}Y_{0.05}SiO_5$:Ce and Y_2SiO_5:Ce single crystal scintillators, Nucl. Instrum. Methods Phys. Res. B 286 (2012) 72-75.

[61] https://www.epic-crystal.com/products/ (last accessed on 20.12.2021)

[62] Suffian M. Tajudin, Y. Namito, T. Sanami, H. Hirayama, Response of plastic scintillator to gamma sources, Applied Radiation and Isotopes, 159 (2020) 109086. ISSN 0969-8043.

[63] Yamamoto S., Horii H., Hurutani M., Matsumoto K., Senda M., Investigation of single, random, and true counts from natural radioactivity in LSO-based clinical PET. Ann. Nucl. Instrum. Med. 19 (2005) 109-114.

[64] P.L. Reeder, Neutron detection using GSO scintillator, Nucl. Instrum. Methods A 340 (1994) 371-378.

[65] M.P. Taggart, M. Nakhostin, P.J. Sellin, Investigation into the potential of GAGG:Ce as a neutron detector, Nucl. Instrum. Methods Phys. Res. A 931 (2019) 121-126.

[66] M. C. M. Angub, et al., Hydrothermal growth of vertically aligned ZnO nanorods as potential scintillator materials for radiation detectors. Journal of Luminescence, (2018) 427-435.

[67] J. Li, R. Dahal, S. Majety, J.Y. Lin, H.X. Jiang, Hexagonal boron nitride epitaxial layers as neutron detector materials, Nucl. Instrum. Methods Phys. Res. A 654 (2011) 417-420.

[68] T.C. Doan, S. Majety, S. Grenadier, J. Li, J.Y. Lin, H.X. Jiang, Hexagonal boron nitride thin film thermal neutron detectors with high energy resolution of the reaction products, Nuclear Instruments and Methods in Physics Research A 783 (2015) 121-127.

[69] T. Kibédi, et al., Evaluation of theoretical conversion coefficients using BrIcc, Nucl. Instrum. Methods A 589 (2008) 202-229.

[70] https://www.orcad.com/ (last accessed on 02.06.2022)

[71] R. Klanner, Characterisation of SiPMs, Nucl. Instrum. Methods Phys. Res. A 926 (2019) 36-56.